Search for an mSUGRA Signature in the electron + jets + $\not\!\!E_T$ Final State in $p\overline{p}$ Collisions at $\sqrt{s} = 1.8$ TeV

by

Zhang Zhou

A dissertation submitted to the graduate faculty

in partial fulfillment of the requirements for the degree of

DOCTOR OF PHILOSOPHY

Major: High Energy Physics

Program of Study Committee:
John Hauptman, Major Professor
James Cochran
John Hill
Suraj Kothari
Jianwei Qiu

Iowa State University

Ames, Iowa

2001

Copyright © Zhang Zhou, 2001. All rights reserved.

Graduate College
Iowa State University

This is to certify that the Doctoral dissertation of

Zhang Zhou

has met the dissertation requirements of Iowa State University

Major Professor

For the Major Program

To my grandma and my parents, and in memory of my grandpa.

TABLE OF CONTENTS

1 THE STANDARD MODEL AND BEYOND 1

1.1 Brief History of Particle Physics 1

1.2 The Standard Model 4

1.3 Beyond the Standard Model and Supersymmetry 6

2 INTRODUCTION TO THIS ANALYSIS 10

3 THE DØ EXPERIMENT 13

3.1 Overview 13

3.2 Luminosity and Cross Section 14

3.3 The Central Tracking System 15

3.3.1 The Vertex Drift Chamber (VTX) 15

3.3.2 The Transition Radiation Detector (TRD) 16

3.3.3 The Central Drift Chamber (CDC) 16

3.3.4 The Forward Drift Chamber (FDC) 17

3.4 The Calorimeter 18

3.5 The Muon System 22

3.6 Triggering and Data Acquisition (DAQ) 24

3.6.1 The Level 0 Triggers 24

3.6.2 The Level 1 Triggers 24

3.6.3 The Level 1.5 Triggers 25

3.6.4 The Level 2 Triggers 25

3.7 Event Reconstruction and Object Identification 27

3.7.1 Tracking Finding 27

3.7.2 Event Vertex 27
3.7.3 Electron and Photon Reconstruction 28
3.7.4 Jet Reconstruction 34
3.7.5 Muon Reconstruction 37
3.7.6 $\not\!\!E_T$ reconstruction 38

4 INITIAL DATA SELECTION 39

4.1 Trigger 39
4.2 Initial Offline Data Selection 39
4.2.1 Data Cleaning Cuts 39
4.2.2 Object Kinematic and Fiducial Cuts 40
4.2.3 Object ID Cuts 41
4.2.4 Vertex Cut 42
4.2.5 Conclusion 42

5 ELECTRON AND JET IDENTIFICATION EFFICIENCY 45

5.1 Electron Identification Efficiency 45
5.2 Jet Identification Efficiency 47
5.2.1 CC Jet *emf* Efficiency 49
5.2.2 CC Jet *chf* Efficiency 51
5.2.3 CC Jet *hcf* Efficiency 53
5.2.4 Total CC Jet ID Efficiency 53
5.2.5 ICR Jet Efficiency 54
5.2.6 EC Jet Efficiency 55

6 FAST MONTE-CARLO 64

6.1 Detector Simulation 64
6.2 Trigger Simulation 65
6.2.1 Level 1 EM and Level 2 ELE Efficiency 65
6.2.2 Level 1 JT and Level 2 JET Efficiency 67
6.2.3 Level 2 $\not\!\!E_T$ Efficiency 69

6.2.4 Overall Trigger Efficiency . . . 70
6.3 The Integrated FMCØ . . . 72
6.4 Summary . . . 77
7 BACKGROUNDS . . . 78
7.1 QCD Multijet Background . . . 78
7.2 $t\bar{t}$ Background . . . 80
7.3 WW Background . . . 81
7.4 $W+$ jets Background . . . 82
7.4.1 Measuring the Scaling Factor α . . . 83
7.4.2 Estimating the Number of $W+ \geq 3$ jet Events, N_3^W . . . 86
7.4.3 Calculating the Number of $W+ \geq 4$ jet Events, N_4^W . . . 86
7.5 Summary . . . 88
8 SIGNAL ANALYSIS . . . 92
8.1 Neural Network Analysis . . . 92
8.2 Signal Significance . . . 98
9 RESULTS . . . 104
10 PRODUCTION CROSS SECTION OF $t\bar{t}$ . . . 105
10.1 $W+$ jets Background . . . 105
10.1.1 Measuring the Scaling Factor: α . . . 105
10.1.2 Estimating the Number of $W+ \geq 4$ jet Events . . . 106
10.2 Measuring the $\sigma_{t\bar{t}}$ . . . 108
APPENDIX A ICR AND EC JET ID EFFICIENCIES . . . 113
APPENDIX B VECBOS AND QCD DYNAMIC SCALE Q^2 . . . 117
APPENDIX C $t\bar{t}$ 3C FIT . . . 119
APPENDIX D NEURAL NETWORKS . . . 125
D.1 Perceptron . . . 125
D.2 Mathematical Interpretation . . . 127

D.3 Using Neural Networks 128

BIBLIOGRAPHY 130

LIST OF FIGURES

Figure 2.1 Feynman diagram for gluino pair production and decay to one electron, 4 jets, and $\not\!\!E_T$. 10

Figure 2.2 The current exclusion contour from the DØ dilepton analysis for $\tan(\beta) = 3$ [41]. Also plotted is the LEP 1 exclusion contour [31]. Parameter space below the contour is excluded. 12

Figure 3.1 The DØ detector. 14

Figure 3.2 The central tracking system. 15

Figure 3.3 The Central Drift Chamber. 17

Figure 3.4 Exploded view of one of the two Forward Drift Chambers. 18

Figure 3.5 The DØ calorimeter. 19

Figure 3.6 Schematic view of two units of calorimeter cells. 20

Figure 3.7 Side view of one quadrant of the DØ calorimeter. Also shown are lines of constant pseudorapidity (η_d) lines. 22

Figure 3.8 Side view of the DØ muon system. 23

Figure 3.9 A diagram of the DØ trigger and data acquisition system. 26

Figure 3.10 EM fraction (f_{em}) of electron candidates from $Z \to ee$ events (solid) and from multijet triggered data (dashed), for (a) central electrons and (b) forward electrons. The arrows in the plots indicate the "standard" cut used in other DØ analyses. 30

Figure 3.11 Shower shape H-matrix chi-squared (χ^2_{hm}) of electron candidates from $Z \to ee$ events (solid) and from multijet triggered data (dashed), for (a) central electrons and (b) forward electrons. The arrows in the plots indicate the "standard" cut used in other DØ analyses. 31

Figure 3.12 Track match significance (σ_{trk}) of electron candidates from $Z \to ee$ events (solid) and from multijet triggered data (dashed), for (a) central electrons and (b) forward electrons. The arrows in the plots indicate the "standard" cut used in other DØ analyses. 33

Figure 3.13 Electron isolation fraction ($fiso$) of electron candidates from $Z \to ee$ events (solid) and from multijet triggered data (dashed), for (a) central electrons and (b) forward electrons. The arrows in the plots indicate the "standard" cut used in other DØ analyses. 35

Figure 5.1 Method of measuring electron identification efficiency. The two regions between the lines on either side of the signal region, (81,101) GeV, are the side-bands for background calculation (see text). 46

Figure 5.2 CC (left) and EC (right) electron efficiency as a function of *eid* cuts and the number of jets present in the event. 48

Figure 5.3 Raw CC jet *emf* distribution. 50

Figure 5.4 R_{MET} distribution for the CC jets. The lines indicate the R_{MET} cut ($R_{\mathrm{MET}} > 1.43$) which would be applied to clean up the sample (see text). 51

Figure 5.5 CC jet *emf* distribution after the R_{MET} cut. 52

Figure 5.6 Ratio of the CC jet *emf* after and before the R_{MET} cut as a function of *emf*. The lines indicate the *emf* ID cuts applied to the data. Jets with *emf* between the lines are accepted. 53

Figure 5.7 Calculating CC *emf* cut efficiency. The jets in this plot are required to pass 15GeV $< \mathrm{E}_{\mathrm{T}}^{\mathrm{j}} <$ 17GeV. The histogram is the *emf* distribution after the R_{MET} cut. The curves are functions fitted (see text) to the *emf* within the region they are drawn. The straight line is the tangential line of the histogram at which the *emf* cut($emf > 0.2$) was applied. 54

Figure 5.8 Ratio of the CC jet *chf* after and before the R_{MET} cut as a function of the jet *chf*. The lines indicate the *chf* ID cut ($chf < 0.4$) applied to the data. Both samples have had *emf* ID cuts applied. 55

Figure 5.9 CC jet *chf* distribution after the R_{MET} and the *emf* cuts. The lines indicate the *chf* ID cut ($chf < 0.4$) applied to the data. 56

Figure 5.10 CC jet *emf*, *chf*, and *hcf* difference between the unfixed and the fixed data. The jets are from the same events from Run 1b ELE_JET_HIGH triggered data (our signal sample) and are matched to 0.1 in $\eta - \phi$ space (to ensure that they are the same jet). The jets were required to pass 15 GeV $< \mathrm{E}_{\mathrm{T}}^{\mathrm{jet}} <$ 25 GeV. The plots indicate that while there is little difference in jet *emf* and *chf* there is a large difference in jet *hcf* between the unfixed and the fixed data. 57

Figure 5.11 CC jet *hcf* distribution for the fixed and the unfixed data. Cut on *hcf* is not necessary for the fixed data. 58

Figure 5.12 CC Jet ID efficiency as a function of E_T^j. Two second-order polynomials were used to fit the points in regions 1 and 2 respectively. 58

Figure 5.13 ICR Jet ID efficiency as a function of E_T^j. Two second-order polynomials were used to fit the points in region 1 and 2 respectively. 60

Figure 5.14 EC Jet ID efficiency. A second-order polynomial was used to fit the points. 63

Figure 6.1 EM Level 1 turn-on curve as a function of offline electron E_T. The Level 1 threshold is 12 GeV. Two scales, $q = 2.0$ and $q = 2.5$ (see text), were used for both CC and EC electrons. 66

Figure 6.2 ELE Level 2 turn-on curve of ELE_JET_HIGH as a function of offline electron E_T. The Level 2 threshold is 15 GeV. Two scales, $q = 1.3$ and $q = 1.4$ (see text), were used for both CC and EC electrons. 68

Figure 6.3 ELE Level 2 turn-on curve of ELE_JET_HIGHA as a function of offline electron E_T. The Level 2 threshold is 17 GeV. Two scales, $q = 1.3$ and $q = 1.4$ (see text), were used for both CC and EC electrons. 69

Figure 6.4 Combined Level 1 JT and Level 2 JET turn-on curve of ELE_JET_HIGH for a single jet. It is a function of offline jet E_T and jet fiducial region. The Level 1 jet tower E_T threshold is 5 GeV and the Level 2 jet E_T threshold is 10 GeV. The fits were performed in the region where the curves were drawn. 72

Figure 6.5 Flow-chart of FMCØ. Prefix "s" refers to smeared objects. 74

Figure 7.1 Calculating the QCD multijet background in the electron sample by normalizing $\not\!\!E_T$ spectrum of fake sample to that of the electron sample in the low $\not\!\!E_T$ region. The fake sample is plotted in circles and the electron sample is plotted in histogram. The errors are statistical only. The plots are for CC electrons. 79

Figure 7.2 Calculating the QCD multijet background in the electron sample by normalizing $\not\!\!E_T$ spectrum of fake sample to that of the electron sample in the low $\not\!\!E_T$ region. The fake sample is plotted in circles and the electron sample is plotted in histogram. The errors are statistical only. The plots are for EC electrons. 80

Figure 7.3 Expected NN output for the $W+ \geq 1$ jet (top left), $W+ \geq 2$ jet (top right), $W+ \geq 3$ jet (bottom left), $W+ \geq 4$ jet (bottom right) events, and the corresponding background events. 89

Figure 7.4 NN output for the expected (points) and the real (histogram) data. In the top left plot at least 1 jet was required; in the top right plot at least 2 jets were required; in the bottom left plot at least 3 jes were required and in the bottom right plot at least 4 jets were required. The data events were required to pass the EM1_EISTRKCC_MS trigger. 90

Figure 7.5 Fitting $W+ \geq n$ jet events to a power law as shown in Equation 7.3. The fit shows that the power law is well observed in the data. 91

Figure 7.6 Expected NN output for $W+ \geq 3$ jet and its corresponding background events (left plot) and NN output for the expected (points) and the real (histogram) data (right plot). The MC (data) events were simulated (required) to pass the ELE_JET_HIGH(A) trigger. 91

Figure 8.1 Distribution of Neural Network variables for data (histogram), background (circles) and signal (hatched histogram). The number of signal events is normalized to the number of background events. The signal was generated with $M_0 = 170$ GeV, $M_{1/2} = 58$ GeV and $\tan(\beta) = 3.0$. . 94

Figure 8.2 Distribution of $cos(\theta_j^*)$ (left) and $cos(\theta_e^*)$ (right) for the signal (hatched histogram) and $t\bar{t}$ (histogram) events. The number of events was normalized to the number of $t\bar{t}$ events expected in our final sample. 95

Figure 8.3 Result of Neural Network training. The small bump on the right end of the distribution is the expected signal. The signal was generated with $M_0 = 170$ GeV, $M_{1/2} = 58$ GeV and $\tan(\beta) = 3.0$. The backgrounds are stacked up in the order of $W(e\nu)+$ jet, $W(\tau\nu)+$ jet, QCD multijet, $t\bar{t}$, and WW. All events are normalized to their expected number of events in data. 96

Figure 8.4 Neural Network output for the data (histogram), signal (hatched histogram) and background (points). The signal was generated with $M_0 =$ 170 GeV, $M_{1/2} = 58$ GeV and $\tan(\beta) = 3.0$. The background expectation describes the data very well. The line indicates the cut on NN output which corresponds to the maximum signal significance. The significance (described in section 8.2) as a function of NN output is also plotted. 97

Figure 9.1 95% C.L. exclusion contour for mSUGRA with $\tan(\beta) = 3.0$. Also plotted is the result of DØ dilepton [41] and LEP I [31] analyses. 104

Figure 10.1 Fitting N_i to Equation 10.1 (see text). We assume that the number of $W+$ jet events follows scaling law as a function of inclusive jet multiplicity. 107

Figure 10.2 Distribution of Neural Network variables for $t\bar{t}$ signal (hatched histogram) and background (histogram). The number of $t\bar{t}$ events is normalized to the same number of background events. 109

Figure 10.3 Result of Neural Network training. The background distribution peaks on the left and the $t\bar{t}$ signal peaks on the right. The right end of the distribution is the expected signal ($\sigma_{t\bar{t}} = 5.9$ pb was used). The backgrounds are stacked up in the order of $W(e\nu)+$ jet, $W(\tau\nu)+$ jet, QCD multijet, and WW. All events are normalized to their expected number of events in data respectively. 111

Figure 10.4 Neural Network output for the data (histogram), $t\bar{t}$ signal (hatched histogram), and background (points). The number of signal events is normalized to our measured $t\bar{t}$ cross section: $\sigma_{t\bar{t}} = 6.13$ pb. The line indicates the cut on NN output which corresponds to the highest signal significance. 112

Figure A.1 Ratio of *emf* after and before the R_{MET} cut for the ICR jets. Depletion in the high end of the distribution indicates that the contribution of noise and fakes is not negligible. 113

Figure A.2 ICR jet *emf* distribution after the R_{MET} cut. The lines indicate the *emf* cut. Jets with $emf < 0.95$ are accepted. 114

Figure A.3 ICR jet *chf* distribution after the R_{MET} and *emf* cuts. The lines indicate the *chf* cut. Jets with $chf < 0.6$ are accepted. 114

Figure A.4 Ratio of *emf* after and before the R_{MET} cut for the EC jets. Depletion in the low and high ends of the distribution indicate that the contribution of noise and fakes are not negligible. 115

Figure A.5 EC jet *emf* distribution after the R_{MET} cut. The lines indicates the *emf* cut. Jets with $0.05 < emf < 0.95$ are accepted. 115

Figure A.6 EC jet *chf* distribution after the R_{MET} and *emf* cuts. The lines indicates the *chf* cut. Jets with $chf < 0.4$ are accepted. 116

Figure B.1 Expected H_T distribution (points) vs data H_T distribution (histogram). VECBOS was generated with $Q^2 = (\frac{1}{n}\sum_i E_T^{parton})^2$ (left plot) and $Q^2 = M_W^2$ (right plot). At least 3 jets were required. 118

Figure C.1 χ^2 distribution of 3C fit to $t\bar{t}$ events. The top plot shows the χ^2 distribution for fits which result in the correct permutation. A χ^2 function with 3 degrees of freedom is also drawn. The middle plot shows the χ^2 distribution for events which a matching between the fitted jets to partons is identifiable (although may not be correct). The ratio of the number of events in the top plot to the middle plot gives how often our fitter results in a correct permutation. The rate is 52%. The bottom plot shows the χ^2 distribution we would expect for our data $t\bar{t}$ events. For representation purpose, the middle and the bottom plots show the χ^2 distributions only up to $\chi^2 = 100$. 122

Figure C.2 χ^2 distributions of 3C fits performed on W+jet, QCD multijet, WW, and mSUGRA events. All events are required to have passed our initial selection cuts (see Chapter 4). In each plot we have a χ^2 cutoff at 100. . 123

Figure C.3 Distribution of pull quantities of all variables which have finite resolution. A Gaussian fit between (-3,3) is also plotted on top of each distribution. The fits indicate that the resolution assignment was correct. 124

Figure D.1 A perceptron. 126

Figure D.2 The sigmoid function: $g(x) = \frac{1}{1+e^{-x}}$. 126

Figure D.3 A multilayer perceptron feed-forward neural network. There are 2 input nodes, 3 hidden nodes, and 1 output node. 127

LIST OF TABLES

Table 1.1 Quark and leptons in the Standard Model. The quarks are denoted as: u—up, d—down, c—charm, s—strange, t—top, b—bottom. The leptons are denoted as: e—electron, μ—muon, τ—tau and their corresponding neutrinos. The numbers in the parentheses are electric charge (in units of proton charge) and mass or mass limit (in GeV). Each particle has its anti-particle, which has equal mass and equal physical properties but opposite charge. 4

Table 1.2 Particles that carry forces in the Standard Model. The numbers in the parentheses are electric charge (in units of proton charge) and mass (in GeV). The photon (γ), Z and gluon (g) are their own anti-particles, while W^+ and W^- are anti-particles of each other. The gluon is responsible for mediating strong interaction between the quarks. 4

Table 1.3 Chiral and gauge supermultiplets in the MSSM. 8

Table 1.4 Mass and gauge eigenstates in the MSSM. 9

Table 4.1 Triggers used for the electron channel analysis. The Level 2 "electron" requires the EM object passes the electron transverse and longitudinal shower shape cut. The EM1_EISTRKCC_MS triggered data are used for background study (see Chapter 7). 44

Table 5.1 Electron ID efficiency used in this analysis. The electron likelihood cuts are $L_5^e < 0.5$ for CC electrons and $L_4^e < 0.3$ for EC electrons. 47

Table 5.2 CC jet ID efficiency as a function of E_T^j. 59

Table 5.3 Fitted results of CC jet ID efficiency. The two curves intersect at E_T^j = 27.36 GeV (see text and Figure 5.12). 60

Table 5.4 ICR jet ID efficiency as a function of E_T^j. 61

Table 5.5 Fitted results of ICR jet ID efficiency. The two curves intersect at E_T^j = 30.46 GeV (see text and Figure 5.14). 62

Table 5.6 EC jet ID efficiency as a function of E_T^j. 62

Table 5.7 Fitted results of EC jet ID efficiency. 63

Table 6.1 Fit results of EM (Level 1) turn-on curves of ELE_JET_HIGH. Two scales, $q = 2.0$ and $q = 2.5$, were used for both CC and EC electrons. The fit parameters from the two scales were averaged and listed in the last column. The errors in the third and fourth columns come from the fit while the errors in the last column include statistical and systematic errors (see text). 67

Table 6.2 Fit results of ELE (Level 2) turn-on curves of ELE_JET_HIGH. The Level 2 threshold is 15 GeV. Two scales, $q = 1.3$ and $q = 1.4$, were used for both CC and EC electrons. The fit parameters from the two scales were averaged and listed in the last column. The error in the third and fourth columns come from the fit while the errors in the last column include statistical and systematic errors (see text). 70

Table 6.3 Fit results of ELE (Level 2) turn-on curves of ELE_JET_HIGHA. The Level 2 threshold is 17 GeV. Two scales, $q = 1.3$ and $q = 1.4$, were used for both CC and EC electrons. The fit parameters from the two scales were averaged and listed in the last column. The error in the third and fourth columns come from the fit while the errors in the last column include statistical and systematic errors (see text). 71

Table 6.4 Fit results of the JT/JET turn-on curve of ELE_JET_HIGH for a single jet. The errors are from the fit. 73

Table 6.5 Probability of an online electron to pass the JT/JET requirement of the ELE_JET_HIGH trigger. 73

Table 6.6 Comparison of the ELE_JET_HIGH trigger efficiency. The second column lists the efficiencies the top group measured using $W+$ jet data events [44]; the third and fourth columns list the simulated efficiencies by putting the VECBOS $W+$ jet sample through FMCØ. "EJ" and "MW" refer to the two QCD dynamic scales at which the VECBOS samples were generated (see text). 74

Table 6.7 Comparison of kinematic acceptance of GEANT (HERWIG as generator) FMCØ (HERWIG and PYTHIA as generators) events as a function of inclusive jet multiplicity (N_{jet}). All three samples are $t\bar{t}$ events with m_{top} = 170 GeV/c^2. The errors of the acceptance of the GEANT $t\bar{t}$ sample include statistical error and the error on the MC electron ID efficiency. The errors on the FMCØ samples are statistical only. 76

Table 7.1 Estimated number of QCD multijet background events, N_{QCD}, as a function of inclusive jet multiplicity, N_{jet} in the ELE_JET_HIGH sample. CC and EC results are combined. σ_1, σ_2, σ_3, and σ_4 are errors from four different sources (see text). 81

Table 7.2 Estimated number of the $t\bar{t}$ background events, $N_{t\bar{t}}$, in ≥ 3 and ≥ 4 jet data samples (ELE_JET_HIGH(A)). The errors (in the form of relative error) come from cross section (σ_{xsec}), trigger/ID efficiency (σ_ε), difference in MC (σ_{MC}) and luminosity (σ_{lum}). 81

Table 7.3 Estimated number of WW background events, N_{WW}, in ≥ 3 and ≥ 4 jet data samples (ELE_JET_HIGH(A)). The errors (in the form of relative error) come from cross section (σ_{xsec}), trigger/ID efficiency (σ_ε), difference in MC (σ_{MC}), jet energy scale (σ_{escale}) and luminosity (σ_{lum}). 82

Table 7.4 Estimated number of $W+ \geq n$ jet events, $\overline{N}_n^W$ as a function of inclusive jet multiplicity in the EM1_EISTRKCC_MS data. They were obtained by normalizing MC to data in the NN output region where $W+ \geq n$ jet events dominate (see text). 87

Table 7.5 Estimated of the number of $W+ \geq 3$ and $W+ \geq 4$ jet events as a function of jet multiplicity in ELE_JET_HIGH(A) data. They were obtained by normalizing MC to data in the NN output region where $W+ \geq n$ jet events dominate (see text). 88

Table 8.1 Number of observed data events—N_{obs}, expected total background events N_{bkgd}^{total} and its breakdown in various sources, expected signal events N_{SUSY}, signal acceptance a_{SUSY} and significance $\overline{s}$ as a function of NN output cut. The signal was generated with $M_0 = 170$ GeV, $M_{1/2} = 58$ GeV and $\tan(\beta) = 3.0$. 101

Table 8.2 Number of observed data events N_{obs}, expected total background events N_{bkgd}^{total} and expected signal events N_{SUSY} corresponding to the optimal NN cut for different model points. The signal acceptance before NN cut a_{SUSY}^{preNN} and after NN cut a_{SUSY}^{postNN}, $mSUGRA$ production cross section at each model point and the calculated 95% C.L. cross section upper limit are also listed. All models have $\tan(\beta) = 3$. This table lists results for 150 GeV $\leq M_0 \leq$ 200 GeV. 102

Table 8.2 (continued) Number of observed data events N_{obs}, expected total background events N_{bkgd}^{total} and expected signal events N_{SUSY} corresponding to the optimal NN cut for different model points. The signal acceptance before NN cut a_{SUSY}^{preNN} and after NN cut a_{SUSY}^{postNN}, $mSUGRA$ production cross section at each model point and the calculated 95% C.L. cross section upper limit are also listed. All models have $\tan(\beta) = 3$. This table lists results for 210 GeV $\leq M_0 \leq$ 260 GeV. 103

Table 10.1 Estimating the scaling factor α by fitting N_i to Equation 10.1 (see text). The numbers are pertinent to the EM1_EISTRKCC_MS trigger. 106

Table 10.2 Numbers used in Equation 10.3. They are pertinent to the ELE_JET_HIGH(A) trigger. 108

Table 10.3 Number of events for each background source after NN optimization (NNOutput ≥ 0.8). 110

Table C.1 Object resolutions. The operator $\bigoplus$ denotes a sum in quadrature. . . . 120

ABSTRACT

We describe a search for a Minimal Supergravity (mSUGRA) signature in Run 1 data taken by the DØ detector at the Fermilab Tevatron from 1995-1996. The total data luminosity is 92.7 pb^{-1}. The data were examined for events with a single electron, four or more jets and large missing transverse energy. The major backgrounds are from W+jets, QCD, $t\bar{t}$, and WW events. We observed no excess of events in our data. Based on the data and the expected signal rate we obtain new limits on new physics in terms of mSUGRA model parameters.

ACKNOWLEDGMENTS

I had never thought of becoming a High Energy Physicist when I first came to the states. It almost looked like a conspiracy that I was assigned to an office with Bryan Lauer, then a graduate student in HEP. All those second year graduate students neighboring our office also happened to be in either HEP or Nuclear Physics. Somehow, they managed to influence my interest with their enthusiasms. I also remember Walter Anderson's enthusiasm when he gave the first-year graduate students an introduction to what He and John Hauptman were doing in their α-HEP group. With sheer interest but not really knowing what it would take to pursue HEP, I talked with John about joining the group. And there was no return since then.

These were seven very exciting years. I was able to work at DØ, Fermilab on many interesting physics problems. One of them, is of course, the topic of this thesis – a search for an mSUGRA signature. I am really amazed at the result because what we observe is just what we expect even though there are very complicated underling physical theories and statistical principles involved. HEP is just beautiful.

These were also seven very difficult years. I was really depressed when I found out that my original thesis topic – a search for color coherence, could not produce a conclusive result and I had to switch to a new topic. But "tribulation produces perseverance; and perseverance, character; and character, hope. Now hope does not disappoint" (Romans 5:3-5). These verses have become my favorite because they are indeed true. Thus, in this acknowledgement, the first person (if I may call Him a person) I want to thank is God. It was He who saved me from destruction and gave me a new birth into a living hope. I thank Him for putting these people and these circumstances in my life so that I can see Him and know Him more. This thesis is firstly dedicated to Him.

I want to thank my parents. They have worked hard all their lives in order that my sister and I can come to states to pursue better lives. In the past seven years I was not able to take care of them at all, yet they have been extremely patient and understanding to me. I also want to thank my grandparents. They brought me up and gave me their best. Unfortunately, I could not finish early enough to let my grandpa share the joy.

I want to thank my advisor, John Hauptman. His support and encouragement were indispensable for the completion of my Ph.D. work. He is to me like a father and a friend who cared for my work as well as my well-being. I enjoyed these seven difficult years largely because he has always been there for me. In terms of physics, I really admire his ability to quickly grasp the essence of a problem and to solve it with simplicity. I hope one day I can be as good too.

I want to thank Walter Anderson, another professor in our group. His support and advice helped me on many facets of life as an international graduate student.

I cannot thank more to the people on DØ, especially Greg Landsberg, whose knowledge and insight in physics analysis have been crucial to this thesis; Rich Genik, who patiently taught me nearly everything about DØ after I switched to the New Phenomena group; Levan Babukhadia, Jim Cochran, John Krane, Sarah Eno, Russell Gilmartin, Ann Heinson, John Hobbs, Dan Karmgard, Myungyun Pang, Scott Snyder, Dave Toback, and Taka Yasuda who directly helped this analysis; Don Lincoln, Rob Snihur and Kate Frame for their hands-on teaching in the K_T group; and Don, Tom Ferbel, Elizabeth Gallas, John Womersley, the Fermion Soccer Team (indoor and outdoor champion in the 1998-1999 season), and fellow graduate students Zarah Casilum, Tina Hebert, Andy Green, Kristal Mauritz, Jorge Molina, Miroslav Siket, Yan Song, and Hai Zheng who all made my stay at DØ a fun experience.

I also want to thank my friends from church. They are: Pastor Lee and his wife Grace, Ling Cherd Ho, Astrid Li, Heather Xia, Fangli and Lichu Chang, Tiffanie Chou, Ming-Jer and Sharon Wong, Paul Ngan, everyone in the choir, and everyone in my bible study small group. They are another family of mine. Their love and prayers have been the comfort and support over all these years.

Finally, I want to thank those fellow ISU graduate students and postdocs who inspired me to

get into HEP. They are Derek Brammeier, Clay Fenlason, Dave Flory, Bryan Lauer, Alaakabha Datta and Di Wang.

Life will move on. Yet, let's cherish what we have today.

1 THE STANDARD MODEL AND BEYOND

1.1 Brief History of Particle Physics

Under the heavens, human beings are the only creatures which are gifted with the ability to reason. We are not satisfied with the mere existence of ourselves, we quest for what we are, where we came from, why we are here and where we are going. We are fascinated (unfortunately, frustrated more often) with the ever-changing world around us and wonder why it is changing as it is.

Particle physics, as a unique discipline, tries to address the fundamental questions of the physical world. Those questions are what this world is made of, what its building blocks (so called fundamental particles) are, how they interact with each other, and why they interact that way.

Ancient Chinese philosophers believed that the world was made of five elements: gold, wood, water, fire, and earth. Similar thoughts were developed in the western world. Between 500 BC and 370 BC, three Greek thinkers, Anaxagoras, Empedocles, and Democritus started maybe the earliest particle physics. Anaxagoras thought that changes in matter were due to different orderings of indivisible particles. Empedocles reduced these indivisible particles into four elements: earth, air, fire, and water, which bear amazing resemblance to the ancient Chinese philosophy. Later, Democritus developed a theory that the universe consists of empty space and an (almost) infinite number of invisible particles which differ from each other in form, position, and arrangement. In his theory, those particles are called indivisible a-tomos, or atoms.

Science, not particle physics in particular, experienced a boom during the Renaissance period. Most important of all is the realization of the importance of measurement and experimentation, thanks to people such as Copernius, Kepler, and Galileo. Their discoveries also laid

the foundation that the physical world could be described by mathematical laws.

In the 18th and 19th century, chemistry was actively studied and developed. Scientists came to agree that a lot of chemical reactions could be understood if there existed a number of elements, i.e., atoms, that form the substances involved in the chemical reactions. These substances "break up" in the chemical reactions to form new substances. Indeed, many kinds of atoms were discovered and in 1872, Mendeleev [1] successfully organized them into what we call the Periodic Table.

The mere fact that there are more than 100 elements categorized in an orderly way in the Periodic Table strongly suggests that these elements are not the fundamental (meaning, indivisible) particles. In 1897, Thompson discovered the electron [2]. In 1911, after an experiment in which α particles were scattered by gold foils, Rutherford inferred that the atoms had a small, heavy, and positively charged nucleus which was surrounded by electrons [3]. In 1913, Bohr formulated a theory which incorporated ideas of quantized angular momenta [4] to describe the interaction between the nucleus and electrons in the atom. The spectrum of Hydrogen calculated by his theory spectacularly agreed with experimental observation. This success heralded the beginning of quantum mechanics. Nuclear decays also led physicists to believe that the nucleus also had substructure. By the late 1920's, with the development of quantum mechanics and more experiments, physicists generally agreed that the nucleus consisted of two kinds of particles: proton, which has one unit of positive charge, and neutron, a particle of similar mass but charge neutral. Protons and neutrons are bound by a strong force [1] to form the nucleus. The proton was found by Rutherford in 1919 [5] and the neutron was found by Chadwick in 1932 [6].

Just when physicists thought that they had finally found all the building blocks of the world: proton, neutron, and electron, a few new startling experimental results indicated "trouble". In the late 1940's, from cosmic rays, physicists found the muon, a particle which has the same electromagnetic property as the electron but is about 200 times heavier. They also found the pion, a particle which mediates strong forces between nucleons [7]. Not many physicists

[1] The force must be strong in order for the protons to overcome the repulsive electric force in the nucleus.

anticipated the discovery of these particles. Yet, more was to come. With the invention of the bubble chamber and high energy accelerators, a great number of new particles which interact strongly like the proton, neutron, and the pion were discovered. They were called hadrons and were categorized into mesons which had integer spin and baryons which had half-integer spin. All these discoveries suggested that there was something more fundamental.

Just as experimental particle physics was making great progress, so was theoretical physics. Dirac, Schwinger, Feynman, and others incorporated Einstein's relativity into quantum mechanics and developed so-called Quantum Electrodynamics (QED) [8]. Yang and Mills constructed what was later called a gauge theory [9]. This theory laid the foundation of modern quantum field theory. In 1964, Gell-Mann and Zweig put forth the quark model [10]. Analogous to explaining the nuclear spectrum using its constituents, the proton and the neutron, they postulated that the mesons and baryons consisted of three types of quarks: up, down and strange. The model beautifully simplified and organized the meson and baryon spectrum. By that time, all four types of fundamental interactions were known: the electromagnetic interaction, the weak interaction, the strong interaction, and the gravitational interaction. In 1967, Weinberg and Salam proposed a theory that unified electromagnetic and weak interactions and predicted the existence of massive and weakly interacting gauge boson W and Z particles [11]. However, no one had seen quarks or the W/Z particles. Whether there were particles smaller than protons or neutrons was still to be experimentally tested.

In 1968, there came an experimental breakthrough. By scattering high energy electron beams (17 GeV) on to a target [12] at Stanford Linear Accelerator Center (SLAC), physicists found evidence of quarks inside protons and neutrons based on the Parton Model [2] by Bjorken and Feynman [13]. Since 1968, more quarks have been discovered: charm in 1974 [14], bottom in 1977 [15] and top in 1995 [16]. During these years, the European Organization for Nuclear Research (CERN) discovered the W and the Z particles [17].

As of today, particle physicists have observed three families of quarks, three families of leptons (each family has two particles) and four interaction-mediators. They are listed in

[2] Partons are point particles in a proton or a neutron.

Tables 1.1 and 1.2. These particles, together with the Higgs, which is responsible for particle masses but has yet to be observed, form the fundamental building blocks of our universe [3].

Table 1.1 Quark and leptons in the Standard Model. The quarks are denoted as: u—up, d—down, c—charm, s—strange, t—top, b—bottom. The leptons are denoted as: e—electron, μ—muon, τ—tau and their corresponding neutrinos. The numbers in the parentheses are electric charge (in units of proton charge) and mass or mass limit (in GeV). Each particle has its anti-particle, which has equal mass and equal physical properties but opposite charge.

Names	Family 1	Family 2	Family 3
quarks	u ($\frac{2}{3}$, 0.003) d ($-\frac{1}{3}$, 0.006)	c ($\frac{2}{3}$, 1.3) s ($-\frac{1}{3}$, 0.1)	t ($\frac{2}{3}$, 175) b ($-\frac{1}{3}$, 4.3)
leptons	e (-1, 0.000511) ν_e (0, $< 3 \times 10^{-9}$)	μ (-1, 0/106) ν_μ (0, < 0.00019)	τ (-1, 1.777) ν_τ (0, < 0.0182)

Table 1.2 Particles that carry forces in the Standard Model. The numbers in the parentheses are electric charge (in units of proton charge) and mass (in GeV). The photon (γ), Z and gluon (g) are their own anti-particles, while W^+ and W^- are anti-particles of each other. The gluon is responsible for mediating strong interaction between the quarks.

γ (0, 0)	$W^\pm$ (± 1, 80.4)	Z (0, 90.187)	g (0, 0)

1.2 The Standard Model

With all these fundamental particles, a natural question to ask is how these particles interact. The *Standard Model* (SM), which is a quantum theory that includes the theory of strong interac-

[3] We still do not know what the dark matter of the universe is. It is believed that they are not particles listed in Tables 1.1 and 1.2.

tions (quantum chromodynamics or QCD) and the unified theory of weak and electromagnetic interactions (electroweak theory), tries to answer this question. The SM Lagrangian [4] $\mathcal{L}$ is:

$$\begin{aligned}
\mathcal{L} \;=\; & \overline{q}\gamma^{\mu}(i\partial_{\mu} - g_s T_a G^a_{\mu})q - \frac{1}{4}G^a_{\mu\nu}G^{\mu\nu}_a \\
& + \overline{L}\gamma^{\mu}\left(i\partial_{\mu} - \frac{g}{2}\boldsymbol{\tau}\cdot\mathbf{W}_{\mu} - \frac{g'}{2}B_{\mu}Y\right)L + \overline{R}\gamma^{\mu}\left(i\partial_{\mu} - \frac{g'}{2}B_{\mu}Y\right)R \\
& - \frac{1}{4}W_{\mu\nu}W^{\mu\nu} - \frac{1}{4}B_{\mu\nu}B^{\mu\nu} \\
& + \left|\left(i\partial_{\mu} - \frac{g}{2}\boldsymbol{\tau}\cdot\mathbf{W}_{\mu} - \frac{g'}{2}B_{\mu}Y\right)\phi\right|^2 - V(\phi) \\
& - G_e\left(\overline{L}\phi R + \overline{R}\phi^{\dagger}L + h.c.\right). \qquad (1.1)
\end{aligned}$$

The SM Lagrangian in Equation 1.1 observes the $\mathrm{SU}(3)_C \otimes \mathrm{SU}(2)_L \otimes \mathrm{U}(1)_Y$ [5] symmetry. The first line describes the strong interaction, which has a strong coupling constant g_s and involves the gluon gauge field. The second and the third lines describe the electroweak interaction, which has the coupling constants g and g', respectively, and involves electroweak gauge fields W and B. The SM could be completely formulated with these 3 lines had the masses of the particles in the theory been zero. In order to generate mass, the SM spontaneously breaks [18] its own symmetry through a mechanism called the Higgs mechanism [19]. The fourth line introduces two $\mathrm{SU}(2)_L \otimes \mathrm{U}(1)_Y$ gauge invariant terms for a scalar field (the Higgs), with the second term $V(\phi)$ being the Higgs potential. If the Higgs potential happens to be in the right form, e.g.,

$$V(\phi) = \mu^2\phi^{\dagger}\phi + \lambda(\phi^{\dagger}\phi)^2, \qquad (1.2)$$

with $\mu^2 < 0$ and $\lambda > 0$, the W and B field will mix to give rise to three massive gauge bosons, the $W^{\pm}$ and Z, and one massless gauge boson, the photon. The fifth line describes the Yukawa coupling between the fermions and the scalar field. This Yukawa coupling gives mass to the fermions.

[4] Lagrangian is the fundamental specification of a quantum field theory. From Lagrangian, the equation of motion can be derived.

[5] C stands for color, L stands for weak-isospin, and Y stands for weak-hypercharge.

1.3 Beyond the Standard Model and Supersymmetry

The Standard Model has been a great achievement in particle physics. A large number of experimental results have confirmed nearly every feature of the theory to a high degree of precision. However, it is by no means the ultimate theory because it poses many unanswered questions and problems [20, 21]. Here are a few most noted ones.

First of all, the SM has eighteen free parameters which can only be put in hand with the aid of experiments. Of the eighteen parameters, nine come from the masses of quarks and charged leptons. Four come from the CKM matrix [22] which describes the mixing among the three families of quarks in their mass eigenstates [6]. The strong, weak, and electromagnetic coupling constants account for three more parameters. The last two parameters come from the Higgs mechanism. One is the vacuum expectation value of the Higgs field and the other is the Higgs mass [7]. The existence of a large number of free parameters strongly suggests that the theory is far from being "ultimate".

Secondly, the Higgs mechanism which is responsible for the spontaneous *Electroweak Symmetry Breaking* (EWSB) was introduced in an *ad hoc* way into the theory. No first principle tells us why the Higgs potential should be written as shown in Equation 1.2.

Thirdly, the SM Higgs self-interaction through fermion loops [27] leads to quadratic divergence of the Higgs mass. The Higgs mass $m_H^2 = -2\mu^2 + c\Lambda^2$, requires a cut-off Λ at which new physics occurs. If the SM is valid up to the GUT [8] scale, the electroweak scale will be driven to the GUT scale, which is obviously wrong. One way to cure this is by fine-tuning the first mass term $-2\mu^2$ so that it cancels exactly the second mass term $c\Lambda^2$. But the tuning has to be accurate to 1 part in 10^{16} [26] at all orders, which is considered to be highly unnatural.

In order to solve these problems, the SM must be extended. One such extension results

[6] The mass eigenstates are not necessarily the same as the weak gauge eigenstates

[7] Note that these eighteen parameters only form the minimal set of free parameters of the Standard Model. If the neutrinos have mass, as strongly suggested by recent experiments [23], we would have three more mass parameters. This would then lead to a corresponding CKM matrix in the lepton sector [24], which adds four more parameters. We have also ignored a parameter called the QCD vacuum angle. It is related to strong CP violation but is deemed to be very small [25]. Thus, the total number of free parameters in the Standard Model can be as many as 26.

[8] GUT stands for Grand Unified Theory, which proposes that the strong, electroweak and gravitational interactions unify at a very high mass scale M_G, e.g. the Planck scale: 10^{19} GeV.

in a theory which incorporates an additional symmetry between fermions and bosons – *Supersymmetry* (SUSY) [28]. It solves the fine tuning problem in the SM by exact cancellation from the loop contribution of SM fermions and their SUSY spin-0 partners. By evolving the SUSY parameters from the GUT scale down to the electroweak scale, one finds that the determinant of Higgs mass matrix in the Higgs potential turns negative resulting in spontaneous EWSB. An additional attractive feature of the theory is that it can be naturally incorporated into GUT. By assuming that the mass of all the SUSY particles is around 1 TeV and by evolving the theory up from the EWSB scale, we find that the coupling constants meet at a scale of about 10^{16} GeV. In fact, many physicists consider this unification of coupling constants as the most important motivation for SUSY [26].

In SUSY, each SM particle and its superpartner (with spin differing by 1/2) form a supermultiplet. The superpartner of a SM fermion is called a *sparticle* (e.g., selectron $\widetilde{e}$ is the superpartner of electron e) and the superpartner of a SM gauge particle is called a *gaugino*, (e.g., gluino $\widetilde{g}$ is the superpartner of gluon g). Among the many extensions of the SM, the one which adds the least number of model parameters is called the Minimal Supersymmetric extension to the SM, or the MSSM. Table 1.3 illustrates the chiral and gauge supermultiplets in the MSSM [28]. Note that two Higgs supermultiplets are required in order to cancel the triangle anomaly [28]. As in the SM, SUSY gauge eigenstates are not necessarily the mass eigenstates. Table 1.4 shows the correspondence between gauge and mass eigenstates in the MSSM [28].

SUSY must be broken or we would have already discovered SUSY particles such as selectrons with $m_{\widetilde{e}} = 0.511$ MeV/c^2. Currently the SUSY breaking mechanisms are still being actively studied theoretically. It is expected that SUSY must be spontaneously broken at a high mass scale, e.g., at the GUT scale. It is "hidden" from us because its mass scale is too high to be reached by current collider experiments. It is also clear that SUSY breaking cannot originate from any of the chiral supermultiplets of the MSSM, the "visible" sector which is accessible by current collider experiments, e.g. the Tevatron. Therefore SUSY breaking has to be mediated from the "hidden" sector to the "visible" sector by flavor-blind interactions [9]. There

[9] If the interaction were not flavor-blind, we would expect contribution from μ_L and e_L mixing in $\mu \to e\gamma$ decay. The current 90% upper limit sets $BR(\mu \to e\gamma) < 1.2 \times 10^{-11}$ [29] strongly restricting the magnitude of

Table 1.3 Chiral and gauge supermultiplets in the MSSM.

Names	spin 0	spin 1/2	spin 1
squarks, quarks (×3 families)	$(\widetilde{u}_L \;\; \widetilde{d}_L)$ $\widetilde{u}^*_R$ $\widetilde{d}^*_R$	$(u_L \;\; d_L)$ $u^\dagger_R$ $d^\dagger_R$	
sleptons, leptons (×3 families)	$(\widetilde{\nu} \;\; \widetilde{e}_L)$ $\widetilde{e}^*_R$	$(\nu \;\; e_L)$ $e^\dagger_R$	
Higgs, higgsinos	$(H^+_u \;\; H^0_u)$ $(H^0_d \;\; H^-_d)$	$(\widetilde{H}^+_u \;\; \widetilde{H}^0_u)$ $(\widetilde{H}^0_d \;\; \widetilde{H}^-_d)$	
gluino, gluon		$\widetilde{g}$	g
winos, W bosons		$\widetilde{W}^\pm \;\; \widetilde{W}^0$	$W^\pm \;\; W0$
bino, B boson		$\widetilde{B}^0$	B^0

are two main competing mechanisms for the mediating interactions: the gravity-mediated and the gauge-mediated interaction. This analysis searches for MSSM in the framework of gravity-mediated supersymmetry breaking. The particular scenario we studied here is called *minimal Supergravity* – mSUGRA [28] [10]. There are only five model parameters in mSUGRA:

- m_0: common scalar particle mass at the SUSY breaking scale M_X [11];
- $m_{1/2}$: common gaugino mass at the M_X scale;
- A_0: common trilinear coupling at the M_X scale;
- $\tan(\beta)$: ratio of the vacuum expectation values of the two Higgs doublets;
- sign(μ): μ is the Higgsino mass parameter.

There is one more important parameter in all SUSY theories, the R-parity. It is defined in Equation 1.3 [30]:

μ_L and e_L mixing.

[10] In general, gravity is not necessarily flavor-blind. The mSUGRA model assumes that gravity is flavor-blind.

[11] M_X is usually the GUT Scale (10^{16} GeV) or the Planck scale (10^{19} GeV).

Table 1.4 Mass and gauge eigenstates in the MSSM.

Names	Spin	Mass Eigenstates	Gauge Eigenstates
Higgs bosons	0	$h^0\ H^0\ A^0\ H^\pm$	$H_u^0\ H_d^0\ H_u^+\ H_d^-$
squarks	0	$\widetilde{u}_L\ \widetilde{u}_R\ \widetilde{d}_L\ \widetilde{d}_R$ $\widetilde{s}_L\ \widetilde{s}_R\ \widetilde{s}_L\ \widetilde{s}_R$ $\widetilde{t}_1\ \widetilde{t}_2\ \widetilde{b}_1\ \widetilde{b}_2$	" " " " $\widetilde{t}_L\ \widetilde{t}_R\ \widetilde{b}_L\ \widetilde{b}_R$
sleptons	0	$\widetilde{e}_L\ \widetilde{e}_R\ \widetilde{\nu}_e$ $\widetilde{\mu}_L\ \widetilde{\mu}_R\ \widetilde{\nu}_\mu$ $\widetilde{\tau}_1\ \widetilde{\tau}_2\ \widetilde{\nu}_\tau$	" " " " $\widetilde{\tau}_L\ \widetilde{\tau}_R\ \widetilde{\nu}_\tau$
neutralinos	1/2	$\widetilde{\chi}_1^0\ \widetilde{\chi}_2^0\ \widetilde{\chi}_3^0\ \widetilde{\chi}_4^0$	$\widetilde{B}^0\ \widetilde{W}^0\ \widetilde{H}_u^0\ \widetilde{H}_d^0$
charginos	1/2	$\widetilde{\chi}_1^\pm\ \widetilde{\chi}_2^\pm$	$\widetilde{W}^\pm\ \widetilde{H}_u^+\ \widetilde{H}_d^-$
gluino	1/2	$\widetilde{g}$	" "
gravitino/goldstino	3/2	$\widetilde{G}$	" "

$$R \equiv (-1)^{3(B-L)+2s}, \tag{1.3}$$

for a particle with baryon number B, lepton number L, and spin s. A SM particle has $R = +1$ and a SUSY particle has $R = -1$. For theories in which R-parity is conserved, there can be no baryon or lepton number violating interactions [28]. Two corollaries also follow if R-parity is conserved:

- SUSY particles must be produced in pairs from SM particles;
- There exists a lightest SUSY particle (LSP) which has an extremely weak coupling to SM particles.

This analysis assumes that R-parity is conserved and that the lightest neutralino $\widetilde{\chi}_1^0$ is the LSP.

2 INTRODUCTION TO THIS ANALYSIS

Under the assumption that R-parity is conserved, SUSY particles must be pair-produced and subsequently cascade decay [1] into LSP through neutralinos, charginos and SM particles. Since the LSP interacts extremely weakly with ordinary matter, it escapes detection and results in a missing transverse energy ($\not{E}_T$) signature. The charginos decay into standard model electroweak gauge bosons (real or virtual), producing leptons or jets [2] in the final state. Figure 2.1 shows one of the many possible scenarios in which a pair of gluinos which are produced ($2 \rightarrow 2$) at the hard scattering decay into a final state with an electron, 4 jets and $\not{E}_T$.

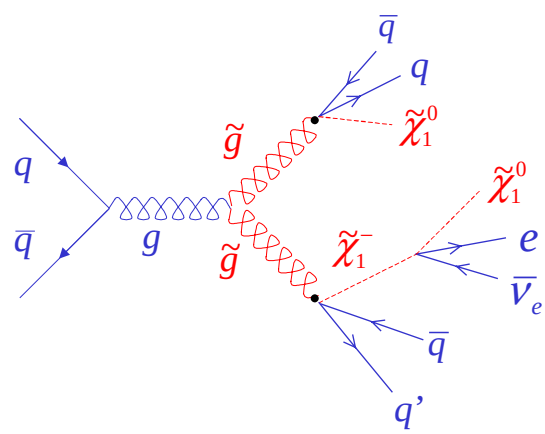

Figure 2.1 Feynman diagram for gluino pair production and decay to one electron, 4 jets, and $\not{E}_T$.

[1] Refers to a chain of decay from initial SUSY particles to LSP and SM particles.

[2] Jets are a group of collimated hadrons traveling in the same direction. The hadrons are produced by quark or gluon fragmentation.

Searches for mSUGRA signature have been performed at LEP [31] and the Tevatron. Previous DØ analyses focused on short cascade decay chains. For example, the DØ dilepton analysis [41] mainly searched for chargino production and its direct decay to leptons, while the DØ $\not\!\!E_T$+jets analysis [42] mainly searched for $\widetilde{g}$ pair, $\widetilde{q}$ pair,and $\widetilde{g}$-$\widetilde{q}$ pair production and their direct decays to jets and $\not\!\!E_T$. Multi-lepton channels have advantages in that they are less contaminated by SM QCD multijet background while the $\not\!\!E_T$+jets channel benefits from large production cross section because of the strong coupling between quarks/gluons and squarks/gluinos. From the results of both analyses it is evident that different final states are complementary in probing the SUSY parameter space.

In this analysis we present a search for an mSUGRA signature in the final states containing a single isolated electron, four or more jets, and large $\not\!\!E_T$. We choose this final state because for large M_0, sleptons and sneutrinos are heavy and the decay of charginos and neutralinos to sleptons and sneutrinos are kinematically forbidden. The charginos and neutralinos instead decay to SM W and/or Z particles which have large branching ratios to jets. The rest of this thesis is organized as follows: we briefly describe the DØ experiment in Chapter 3. The data event selection is described in Chapter 4. The object identification efficiency is described in Chapter 5. Monte Carlo event simulation is described in Chapter 6. Chapter 7 and 8 describe the background and signal analysis, respectively. Chapters 9 and 10 present our results and conclusions. The appendices serve as reference to the tools, extra studies, and more detailed information pertaining to this analysis.

The current limit for mSUGRA in terms of its parameters obtained in the DØ dilepton analysis [41] is shown in Figure 2.2. We will present our results in a similar form. We also fix sign(μ) to be negative and $A_0 = 0$ in this analysis for the following reasons:

- sign(μ) affects the mass difference of gauginos. Positive μ leads to smaller mass difference than negative μ. Smaller mass difference results in electrons with E_T less than DØ electron identification threshold;

- only the lighter stop mass is directly affected by A_0. Tevatron searches with lepton(s) in the final state are not sensitive to A_0.

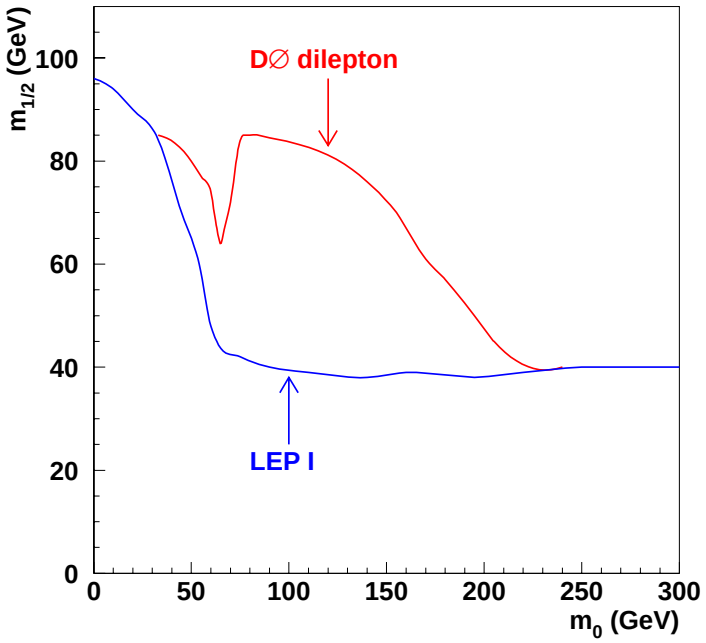

Figure 2.2 The current exclusion contour from the DØ dilepton analysis for $\tan(\beta) = 3$ [41]. Also plotted is the LEP 1 exclusion contour [31]. Parameter space below the contour is excluded.

3 THE DØ EXPERIMENT

3.1 Overview

The DØ Experiment is a collaboration of hundreds of physicists and engineers who study QCD and electroweak physics and search for new physics beyond the Standard Model. The collaboration designed, constructed and used a general-purpose detector located on the Tevatron ring to detect particles coming out of proton and antiproton collisions. Both proton and antiproton are accelerated to an energy of 900 GeV, making the Tevatron the highest energy collider in the world.

The DØ detector weighs approximately 5,500 tons and stands 13 meters in height and 20 meters in length. Shown in Figure 3.1, the detector is comprised of three major systems. From the inside out, they are the central tracking detectors, the calorimeter, and the muon toroid. They are concentric to the beam line.

Because what we want to measure is the energy and the direction of the particles, DØ uses a special coordinate: the η-ϕ coordinate, where η is the pseudorapidity and ϕ is the azimuthal angle. We first define the proton direction as the $+z$ direction. Once the interaction vertex on the z axis and the location of particle energy deposition (usually the center of energy location) are measured, the particle's polar angle θ with respect to the z axis is fixed. We define

$$\eta = -\ln(\tan(\frac{\theta}{2})). \tag{3.1}$$

Angle ϕ of the particle is simply its azimuthal angle around the z axis. The reason we use the η-ϕ coordinate is because η is an additive quantity under Lorentz boost along the z axis.

The pseudorapidity defined in Equation 3.1 is usually called the physics pseudorapidity.

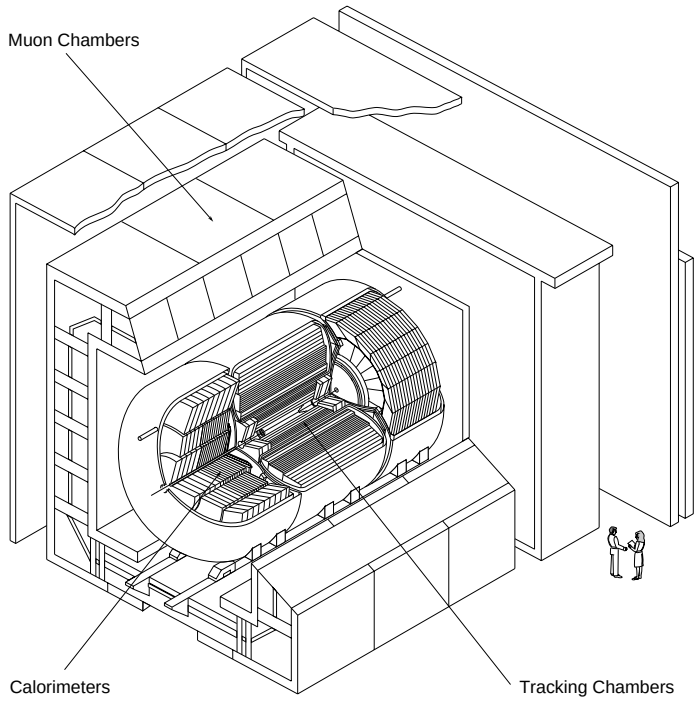

Figure 3.1 The DØ detector.

There is another quantity called the detector pseudorapidity η_d, which is calculated from the polar angle defined by the line connecting the location of particle energy deposition to the origin on the z axis. The detector pseudorapidity tells us where exactly the object is in the detector.

The DØ detector was turned on to take collider data between 1992 and 1996. There were three run periods: 1a, 1b, and 1c. This analysis uses 1b and 1c data.

3.2 Luminosity and Cross Section

For search physics, the most important thing is to estimate how many events we expect to have in our data for the physical processes of interest. The number of events is calculated by Equation 3.2

$$N_{event} = \sigma \cdot \mathcal{L} \cdot a, \tag{3.2}$$

where σ is the cross section of the physical process under study. It is proportional to the probability for the physical process to happen. $\mathcal{L}$ is called the integrated luminosity. It is a measure of the amount of data taken during a certain period of time. The last variable, a, is the acceptance of the physical process after various data selection cuts (see for example Chapter 4 and 6).

3.3 The Central Tracking System

The central tracking system measures the three-dimensional trajectories (tracks) of particles passing through them. From the tracks, the interaction vertex is determined. The system is comprised of four parts: the Vertex Drift Chamber (VTX), the Transition Radiation Detector (TRD), the Central Drift Chamber (CDC), and two Forward Drift Chambers (FDC). The tracking system is positioned radially about the beam line with an inner radius of 3.7 cm and an outer radius of 78 cm. It is shown in Figure 3.2.

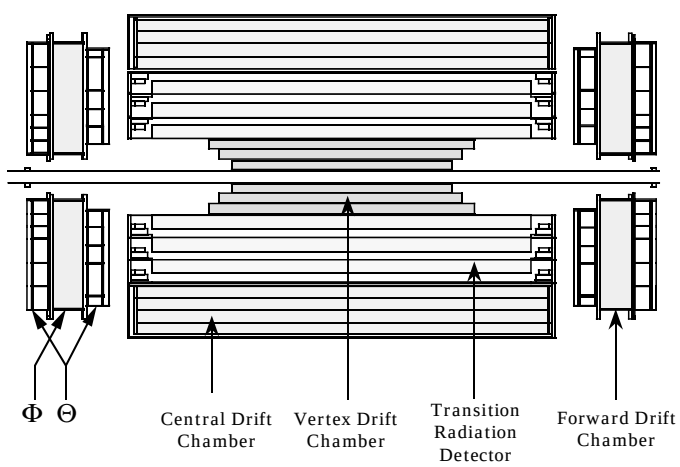

Figure 3.2 The central tracking system.

3.3.1 The Vertex Drift Chamber (VTX)

The VTX is the inner most tracking chamber. It is designed to measure accurately the $p\overline{p}$ interaction vertex along z axis. It extends from 3.7 cm to 16.2 cm in radius, and to ± 116 cm in z. It consists of three concentric cylindrical drift chambers, holding arrays of sense wires parallel

to the beam line. The sense wires operate at an electric potential of 2.5 kV. Carbon dioxide (CO_2) mixed with 5% ethane (C_2H_6) and 0.5% water functions as the *active medium*. Incoming charged particle ionizes the active medium and produces electrons which drift to the sense wire in the electric field. By measuring the electron drift time the trajectory of the incoming particle can be reconstructed. This is the basic principle of a drift chamber. The spatial resolution of the VTX is about 60 μm in $r\phi$ and 1.5 cm in z.

3.3.2 The Transition Radiation Detector (TRD)

When a highly relativistic charged particle crosses the boundary of two materials with different dielectric constants, it radiates photons in the forward direction. The intensity of the radiation is proportional to the energy-mass ratio of the particle. Thus for heavy particles such as pions, the radiation is hardly measurable while for the electron, there is considerable transition radiation that can be measured. The radiation spectrum emitted by multi-GeV electrons is in the form of X-rays.

The TRD is designed to achieve a 10^4 rejection factor against charged pions while remaining 90% efficient with isolated electrons. It is located just outside of the vertex drift chamber. It consists of three layers. Each layer has a radiator consisting of 393 layers of 18 μm-thick polypropylene foil with a mean separation of 150 μm. The gaps are filled with dry nitrogen (N_2). Surrounding each radiator is a cylindrical drift chamber filled with mixture of xenon (Xe), methane (CH_4), and ethane gas (91% : 7% : 2%). This drift chamber is for detection of X-ray radiation. The physical reach of the TRD is $|\eta_d| < 1.1$.

3.3.3 The Central Drift Chamber (CDC)

The CDC lies between the TRD and the calorimeter. It consists of four concentric layers of cells located between 49.5 cm and 74.5 cm in radius and between 92 cm in z. It covers $|\eta_d| < 1.2$. An end view of a portion of the CDC is shown in Figure 3.3.

Each layer of CDC has 32 identical modules, which are arranged in a cylinder. Each layer is also offset by one half cell from the previous layer. Each cell contains seven sense wires (indicated

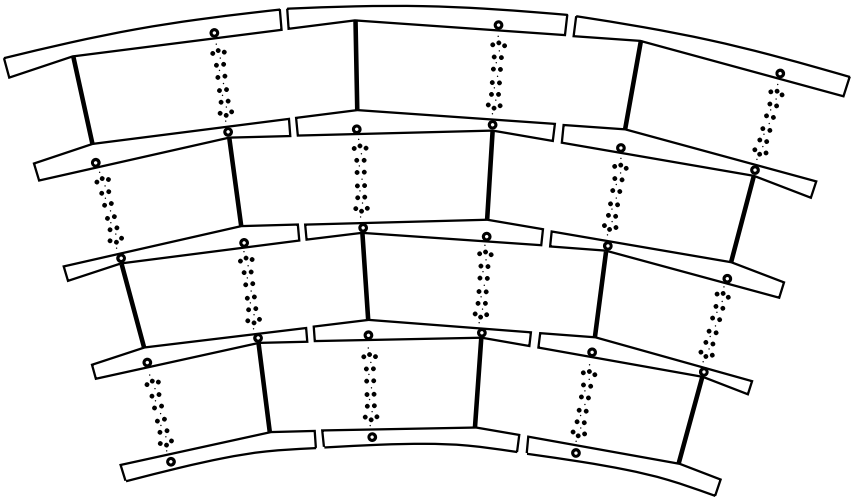

Figure 3.3 The Central Drift Chamber.

by the smallest dots in Figure 3.3) with two grounded potential wires between them. Two delay lines lie inside the inner and outer cell walls. The active medium in CDC is gaseous argon (Ar), methane, carbon dioxide, and water in the ratio of 92.5%, 4%, 3%, and 0.5%. The $r\phi$ position measurement is achieved by the same drift chamber principle discussed in section 3.3.1. For the z position, the delay lines are used. The delay lines are inductive wires which will transmit an induced electric pulse when an avalanche occurs nearby. By measuring the difference in pulse arrival time to both ends of the delay line we can infer the z position of the avalanche. For CDC, the $r\phi$ resolution is about 180 μm and the z resolution is about 2.9 mm.

The CDC is crucial in track reconstruction. The event vertex is determined from tracks (see section 3.7.2). The characteristics of the track also give a hint as to whether the track is formed by an electron or by a heavier particle.

3.3.4 The Forward Drift Chamber (FDC)

The FDC has a tracking coverage of $1.0 < |\eta| < 3.2$. There are two sets of chambers, one located at each end of the CDC. Figure 3.4 shows an exploded view of one of the FDCs. Each FDC consists of three layers of chambers: one Φ layer sandwiched between two Θ layers. The Φ layer is a single chamber divided into 36 azimuthal drift cells, each containing sixteen axial

sense wires. Each of the four quadrants of a Θ chamber consists of six rectangular cells. Each cell contains eight sense wires and one delay line. The two Θ chambers are rotated in ϕ by 45° to obtain optimal position resolution. The operating principle of FDC is the same as that of CDC. The $r\phi$ resolution is about 200 μm and the z resolution is about 4 mm.

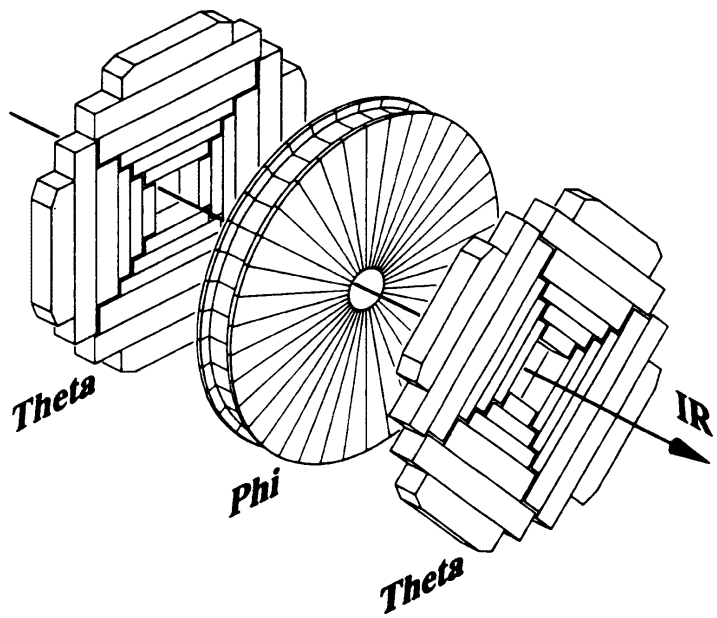

Figure 3.4 Exploded view of one of the two Forward Drift Chambers.

3.4 The Calorimeter

DØ relies on the calorimeter to measure the energies of interacting particles (except for the muons). The geometry of the calorimeter is shown in Figure 3.5. It is segmented into 3 major parts: one central calorimeter (CC) and two end calorimeters (EC), each consisting of an inner electromagnetic (EM) section, a fine hadronic (FH) section and a coarse hadronic (CH) section, housed in a steel cryostat. Between the cryostats is the inter-cryostat detector (ICD) and the "massless gap" (MG) detector.

Electromagnetic particles (electrons and photons) and hadronic particles (e.g., charge pions) lose energy in a material through different mechanisms. A high-energy electron ($\gg$ 10 MeV) loses its energy primarily through bremsstrahlung, while a high-energy photon loses energy primarily through the electron-positron pair production. The particles emitted in these processes

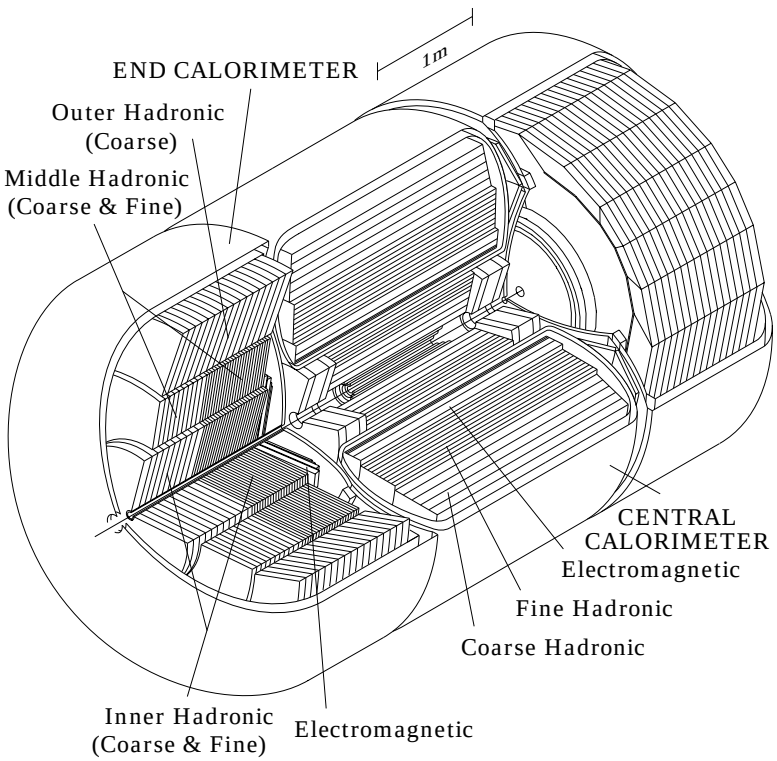

Figure 3.5 The DØ calorimeter.

can themselves undergo bremsstrahlung and pair production, producing secondary electrons, positrons, and photons. This process is call the *electromagnetic shower*. The rate at which an incident EM object loses energy can be described in Equation 3.3

$$\frac{dE}{E} = -\frac{dx}{X_0}, \tag{3.3}$$

where X_0 is called the *radiation length*. It is a constant for same type of material. For uranium, it is about 3.2 mm.

Hadronic particles also produce showers in material, but through a qualitatively different process. Hadrons lose energy primarily through inelastic collisions with atomic nuclei. These collisions produce secondary hadrons, which result in *hadronic showers*. The energy loss can also be characterized by Equation 3.3, with X_0 being the *nuclear interaction length*. The nuclear interaction length is about 10.5 cm for uranium. Thus, a hadronic shower in general expands a longer distance than an electromagnetic shower.

The showering process converts a single high-energy particle into many low-energy particles. The next step is to measure the energy of these particles. In order to build a calorimeter to contain most of the high-energy showers and keep the cost reasonable, DØ uses a technique called *sampling*. A sampling calorimeter alternates layers of dense, inert absorber with layers of active medium which is sensitive to particles passing through it. Since most of the energy is absorbed in the inert material, only a portion of the incident energy can be detected. From the sampling fraction, which is known by design, the incident energy is inferred. A schematic view of DØ calorimeter units (called *calorimeter cells*) is shown in Figure 3.6. At DØ, liquid argon is used as the active medium while plates of uranium (3mm thick), uranium mixed with 1.7% niobium (Ni) (6 mm thick), and copper/steel (46.5 mm) are used as the absorber in the EM, FH, and CH calorimeter respectively.

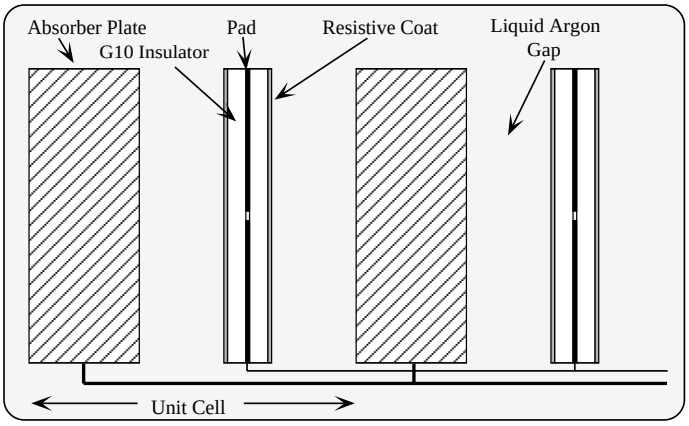

Figure 3.6 Schematic view of two units of calorimeter cells.

The material used for the absorber is important. It needs to be dense enough to hold the showers within reasonable size and is desirable to produce equal response to electron and pion, or e/π ratio = 1. A hadronic shower contains neutral pions (π^0) which predominantly decay to two photons. The photons subsequently produce electromagnetic showers. If the e/π ratio $\neq 1$, then the measured shower energy is subject to fluctuations in the number of pions in the shower, leading to a degraded energy resolution. Also, hadronic response is in general smaller because

the energy to break up nuclei and the energy carried by neutrinos [1] are invisible. In order to compensate for these effects, DØ uses uranium as the primary absorber material. The energy lost to break up nuclei will induce fission which will produce measurable energy to compensate for the lost energy. DØ achieved e/π ratio ≈ 1.1, favorably compared to 1.4 for most other calorimeters [32].

A side view of one quadrant of the DØ calorimeter is shown in Figure 3.7. Each EM section is 21 radiation lengths deep and is divided into four longitudinal layers: EM1–EM4 layers. The hadronic sections are 7–9 nuclear interaction lengths deep and are divided into four (CC) or five (EC) layers. The cells are aligned in towers projecting back toward the center of the detector. The size of each tower is $\Delta\eta \times \Delta\phi = 0.1 \times 0.1$. The third layer of the EM calorimeter, in which the maximum of EM showers is expected, is segmented twice as finely into cells of size $\Delta\eta \times \Delta\phi = 0.05 \times 0.05$. The layout facilitates event triggering and reconstruction. The CC coverage is $|\eta_d| < 1.0$ and the EC coverage is $1.3 < |\eta_d| < 4.0$. In the inter-cryostat region (ICR), ICD (arrays of scintillating counters) mounted on the inner walls of the EC cryostat and MG (consisting of signal board immersed in liquid Argon) positioned inside both the CC and EC cryostat walls are used to supplement coverage: $0.8 < |\eta| < 1.4$.

The calorimeter energy resolutions of electrons and pions were measured using test beams. They are shown in Equation 3.4 and 3.5, respectively. Symbol $\oplus$ means addition in quadrature.

$$\left.\frac{\sigma(E)}{E(\mathrm{GeV})}\right|_{e} = \frac{15\%}{\sqrt{E}} \oplus 0.3\%. \tag{3.4}$$

$$\left.\frac{\sigma(E)}{E(\mathrm{GeV})}\right|_{\pi^{\pm}} = \frac{40\%}{\sqrt{E}}. \tag{3.5}$$

For hadronic jets, the energy resolution was measured by a dijet balance method [33]. The result is

$$\left.\frac{\sigma(E)}{E(\mathrm{GeV})}\right|_{jet} = \frac{80\%}{\sqrt{E}}. \tag{3.6}$$

[1] Weak decay of hadrons always leads to neutrino production. In a highly boosted hadronic jet, the neutrinos follow the same direction of its parent hadrons. This leads to under-measurement of hadron energies.

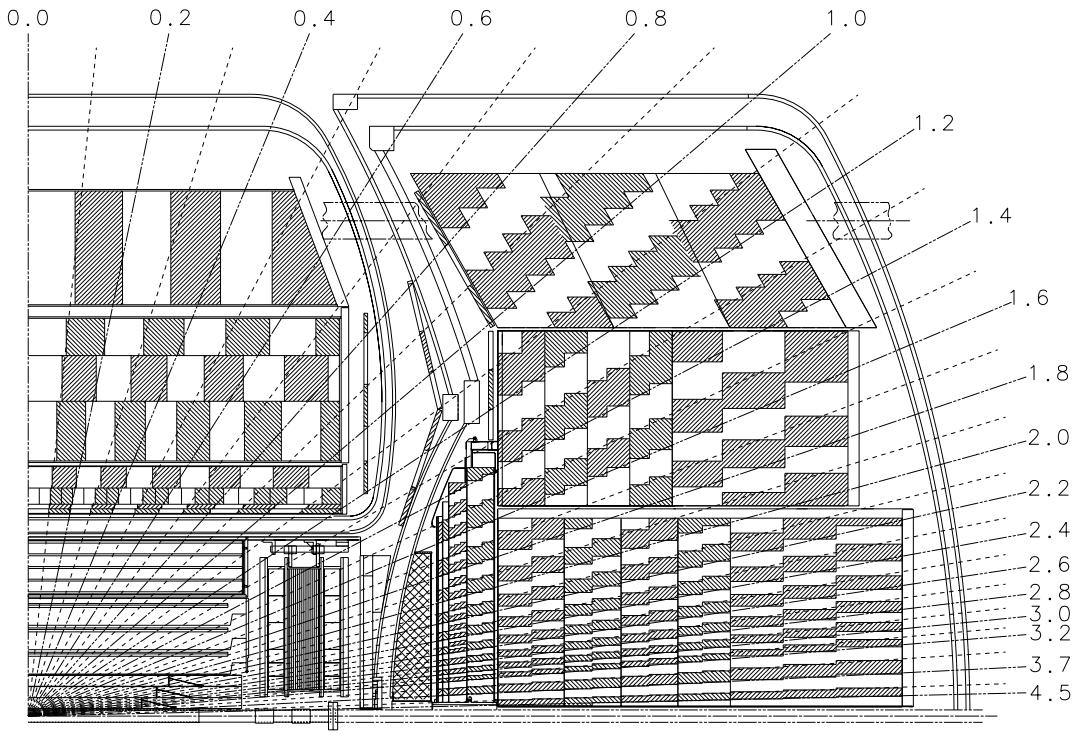

Figure 3.7 Side view of one quadrant of the DØ calorimeter. Also shown are lines of constant pseudorapidity (η_d) lines.

3.5 The Muon System

Since muons are minimum ionizing particles (MIP) they only deposit a small amount of energy in the calorimeter and are seldom absorbed. The detection and momentum measurement of muons are thus achieved by the outermost part of the DØ detector, the muon system. It consists of several layers of proportional drift tube (PDT) chambers on either side of the five toroidal iron magnets with a field strength of approximately 2 Tesla. These magnets are used to bend the tracks of muons passing through the system. Through the angular bend the momentum and charge of the muon are measured. The toroids and associated PDT layers are shown in Figure 3.8

The entire system is divided into two spectrometers: the wide angle muon spectrometer (WAMUS) and the small angle muon spectrometer (SAMUS). The WAMUS occupies three of the five magnets: the Central Fe (CF), covering range $|\eta_d| < 1$, and the two End Fe's

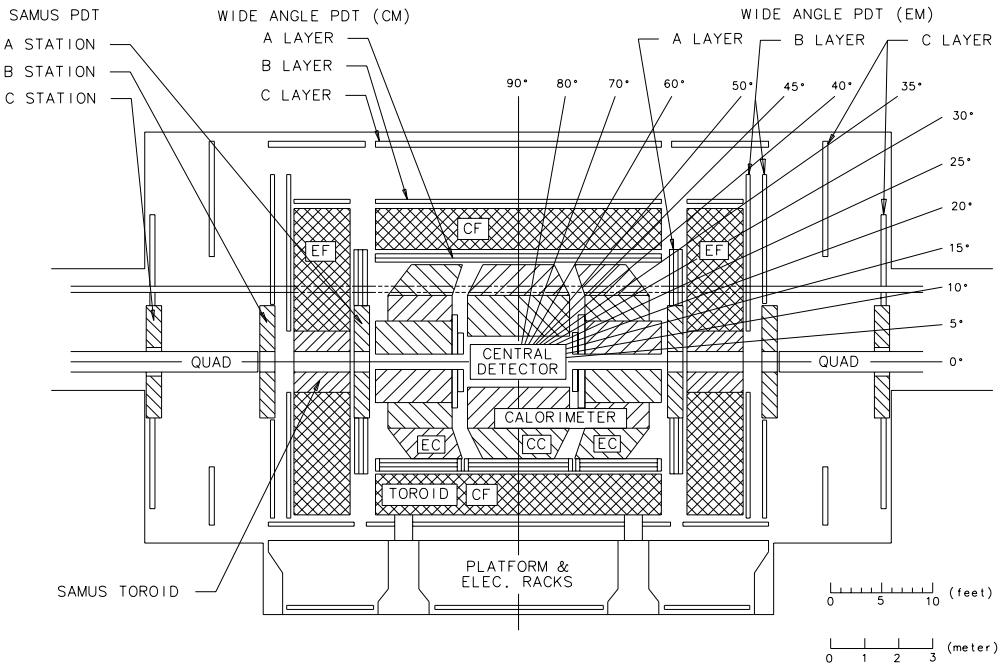

Figure 3.8 Side view of the DØ muon system.

(EF), covering range $1 < |\eta_d| < 2.5$. The CF has nearly 360° coverage in ϕ, except for two gaps underneath the detector required for support structures for the calorimeter. The SAMUS occupies the rest of the magnets. Due to accidental high background rates in this region, the SAMUS is not used in this analysis.

The WAMUS chambers are deployed in three layers: The A layer between the calorimeter and the toroid, and the B and C layers after the toroid. Each plane in the A layer chambers contains four PDTs. They can determine the incident direction of a muon to 0.6 $m$rad, and its position to 100 μm. The B and C layer chambers contain three PDTs each. They can can determine an outgoing muon direction to 0.2 $m$rad, and its position to 170 μm.

The measured muon momentum resolution is parameterized in Equation 3.7

$$\sigma(1/p) = 0.18(p - 2.0)/p^2 \oplus 0.003, \tag{3.7}$$

for muons with momentum $p > 4.0$ GeV/c.

3.6 Triggering and Data Acquisition (DAQ)

At the interaction region $p\overline{p}$ beam crossings occur every 3.5 μs. With the typical run luminosity, on average, at least one collision will occur every crossing. However, not all of these collisions are of equal interest (most events are QCD multijet events). Besides, the electronic and computer system could not handle such a high event rate. A multilevel triggering and filtering system is used at DØ to collect event information and to select apparently interesting events to record. There are altogether four levels of triggering: the Level 0, the Level 1, the Level 1.5, and the Level 2.

3.6.1 The Level 0 Triggers

The Level 0 trigger uses a set of scintillation counters located in front of each EC. It performs the following four functions:

- triggers on inelastic $p\overline{p}$ collision by requiring coincidence between hits in the scintillation counters at two sides of the detector;
- measures the relative instantaneous luminosity;
- identifies multiple interactions within one beam crossing;
- determines the z position of the interaction vertex by calculating the difference in arrival time of hits in the scintillation counters at two sides of the detector.

Events which are flagged as inelastic collisions are passed along to Level 1 triggers.

3.6.2 The Level 1 Triggers

The Level 1 triggering system is comprised of fast and programmable digital signal processors (DSPs). The system uses coarse, rapidly digitized information from the calorimeter and the muon system to determine in less than 3.5 μs if a particular event meets specific criteria on energy deposits and topological requirements to merit further processing. Calorimeter trigger towers with $\Delta\eta \times \Delta\phi = 0.2 \times 0.2$ are used. For electrons, Level 1 requires the transverse energy

in the EM section of a trigger tower to be above programmed thresholds. For jets, it requires the sum of transverse energy in the EM and FH sections of a trigger tower to be above programmed thresholds. For muons, Level 1 provides the number of muon candidates in different regions of the muon spectrometer. The rate out of Level 1 is roughly 800 Hz.

3.6.3 The Level 1.5 Triggers

The Level 1.5 triggering system is also implemented in DSPs. It performs crude clustering of electromagnetic calorimeter tower energies and basic track-finding with hits in the muon chambers. It improves the accuracy of electron energy measured at Level 1 and also has the capability to select purer electron candidates by using variables such as the cluster EM fraction and the EM isolation. These variables are defined in section 3.7.3.1 and 3.7.3.7. The rate out of Level 1.5 is reduced to 200 Hz.

3.6.4 The Level 2 Triggers

The fully digitized data are available at Level 2 triggering system allowing it to reconstruct and to identify specific objects such as electrons, photons, jets, muons, and $\not\!\!E_T$. The system uses a large farm of general-purpose processors which run software filters. The filter usually requires a certain number of objects to be above certain E_T thresholds and to be within certain detector regions. The algorithms to reconstruct objects at Level 2 are summarized below.

- Level 2 electrons: Using the trigger towers that were above threshold at Level 1 as seeds, the Level 2 electron algorithm forms clusters which include all cells in the four EM layers and the first FH layers in a region of $\Delta\eta \times \Delta\phi = 0.3 \times 0.3$, centered around the tower with the highest E_T. Requirements on the longitudinal and transverse energy profile of the cluster are applied to identify Level 2 electrons. In some filters, track and energy cluster matching is also required to pass Level 2 electrons.

- Level 2 jets: A cone jet algorithm is used to reconstruct jets at Level 2. The cone size is: $R = 0.3$, where $R = \sqrt{\Delta\eta^2 + \Delta\phi^2}$. The summed E_T of towers inside the jet cone defines the Level 2 jet E_T.

- Level 2 $\not\!\!E_T$: The $\not\!\!E_T$ is computed using the vector sum of E_T of all calorimeter and ICD cells with respect to the z position of the interaction vertex.

- Level 2 muons: The first stage of the offline reconstruction is performed. Three dimensional track is reconstructed. The track quality is determined by examining various variables associated with the track. Tracks with good quality are accepted. Muon momentum is measured by using the positions of muon PDT hits and the interaction vertex.

The event rate drops to 2 Hz out of Level 2. Any event passing Level 2 is written to tape for offline reconstruction. A diagram of the DØ trigger and data acquisition system is shown in Figure 3.9.

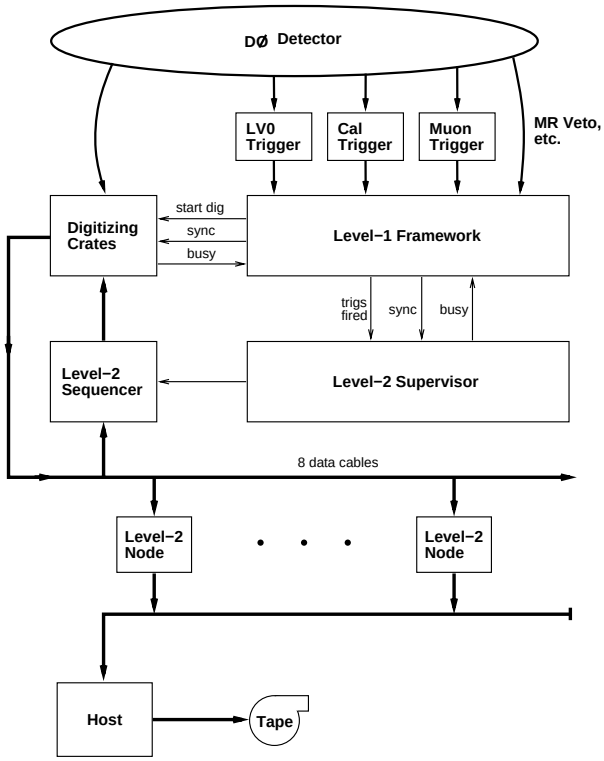

Figure 3.9 A diagram of the DØ trigger and data acquisition system.

3.7 Event Reconstruction and Object Identification

The data written to tape are further processed through the DØ reconstruction program, DØRECO [34]. At this stage, detailed information from the full tracking system and the calibration information of each detector subsystem is available. A full scale event calibration and reconstruction is thus possible and needed. The output of DØRECO consists of the energy and direction of the physical objects: electrons, photons, jets, muons, and $\not\!\!E_T$.

3.7.1 Tracking Finding

Track finding is performed in two steps: first in the $r\phi$ view and then in the rz view. Using the CDC as an example, the algorithm of track finding is described below:

- The outermost hits in each of the four cylindrical layers are paired with the innermost hits in that layer within a segment of ϕ. Hits between each pair are added to form a track segment if they lie on the line defined by the pair;
- The track segments are combined into tracks traversing all four layers of the CDC by beginning with the track segment in the outermost layer, adding the best-fitting segment in the next-outermost layer, and the next-outermost layer until the segments in the innermost layer have been added. Up to one layer may be skipped if collinear segments are found in the remaining three layers;
- After fitting tracks in the $r\phi$ view in this manner, delay line measurements are used to determine the rz positions of the tracks.

Tracks obtained in this way have a resolution about $2.5m$rad in ϕ and $28m$rad in θ. Tracks in the FDC are found using a similar algorithm. Track-finding efficiencies measured from $Z \to ee$ events are $80 \pm 1\%$ in the CDC and $74 \pm 1\%$ in the FDC.

3.7.2 Event Vertex

The event vertex is determined using tracking information from the CDC (or from the FDC if the vertex is not found by the CDC). The steps are:

- For each event, every track is extrapolated to the z axis. Those tracks with impact parameter within 2.5 cm to the z axis are selected.
- These tracks are clustered into different groups based on their z intercepts. The group with the largest number of tracks is selected.
- The z intercepts of these selected tracks are fit to a Gaussian. The mean of the fit is used as the primary event vertex.
- Other groups of tracks undergo a similar fit and the resultant vertices are dubbed as the secondary event vertices, which are deemed to come from minimum bias interactions [2].

This method achieves vertex z resolution to $1-2$ cm. Multiple vertices can be identified if they are separated by at least 7 cm.

3.7.3 Electron and Photon Reconstruction

Electron and photon candidates are reconstructed using a nearest neighbor clustering algorithm. Starting with the most energetic tower in the EM calorimeter, neighboring towers with $E_T > 50$ MeV are added. A neighboring tower is defined as a tower being adjacent or immediately diagonal in $\eta - \phi$ space. This process is repeated with the next most energetic tower in the EM calorimeter not already clustered until all unclustered EM tower have $E_T < 50$ MeV. A cluster which satisfies the following criteria is considered as an electron or photon candidate:

- $E_{total} > 1.5$ GeV;
- $E_T > 1.5$ GeV;
- at least 90% of its energy is in the EM calorimeter;
- at least 40% of its energy is in a single tower.

An EM cluster centroid $\vec{x}_{cog}$ is defined as

[2] The trigger requirement for a minimum bias interaction is that an inelastic collision has happened. Because the large cross section of QCD parton scattering most minimum bias events are low P_T QCD multijet events.

$$\vec{x}_{cog} = \frac{\sum_i w_i \vec{x}_i}{\sum_i w_i}, \tag{3.8}$$

where the sum is over all the cells in the cluster. w_i is the weight of the ith cell and is defined as

$$w_i = \max(0.0, w_0 + \ln(\frac{E_i}{E_{clus}})). \tag{3.9}$$

Electron and photon candidates are then distinguished from each other by whether the cluster has a CDC or an FDC track within a road of size 0.1×0.1 in $\eta - \phi$ space pointing from the primary vertex to the cluster centroid.

Prompt photon or photon pairs from π° decay can mimic an electron if the shower is overlapped with a random track. Carefully chosen variables have been developed to enhance the selection of purer electrons. These variables are EM fraction of the cluster (f_{em}), shower shape H-matrix chi-squared (χ^2_{hm}), track energy loss per unit path length dE/dx, track match significance (σ_{trk}), and the TRD transition efficiency (ε_{TRD}). Because TRD only extends to $|\eta_d| = 1.1$, only the first four variables are used for electron candidates in the EC calorimeter. Each variable has different strength in rejecting different backgrounds. We discuss these variables in detail below.

3.7.3.1 EM fraction of the electron candidate (f_{em})

The EM fraction of an electron candidate is defined as $f_{em} = E_{\rm em}/E_{\rm total}$, where E_{em} is the amount of cluster energy in the EM calorimeter. Figure 3.10 shows the distribution of f_{em} for electron candidates from $Z \to ee$ events, and for electron candidates from multijet events. The former is dominated by signal while the latter is dominated by background.

3.7.3.2 Shower shape H-matrix chi-squared (χ^2_{hm})

The shower shape of an electron or a photon has a distinctive profile from that of a jet. It follows a well known teardrop pattern [35]. Fluctuations cause the energy deposition to vary

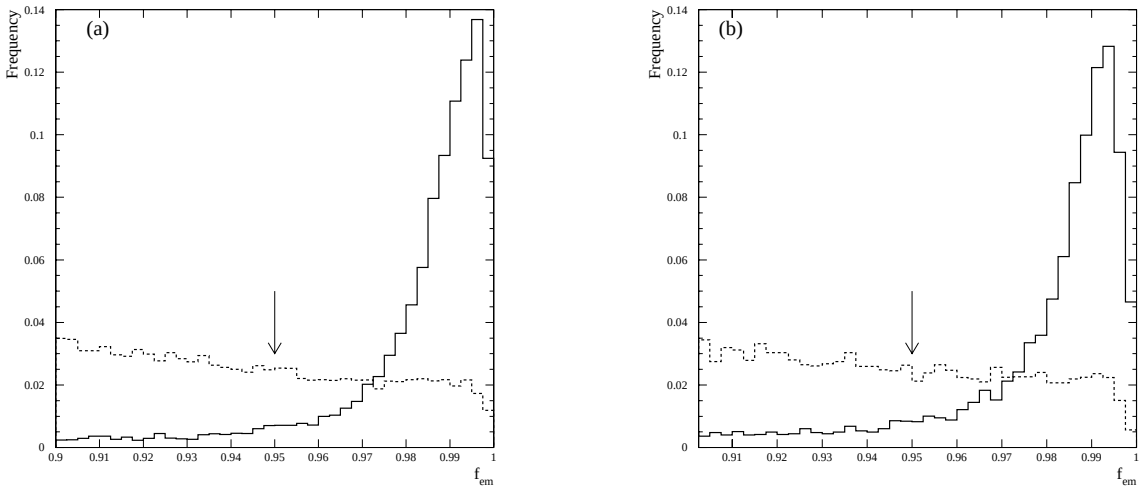

Figure 3.10 EM fraction (f_{em}) of electron candidates from $Z \to ee$ events (solid) and from multijet triggered data (dashed), for (a) central electrons and (b) forward electrons. The arrows in the plots indicate the "standard" cut used in other DØ analyses.

from the average in a correlated fashion among the cells and layers. This correlation is described by a covariance matrix, which is constructed by modeling the electron shower shape with a full detector simulation program such as GEANT [36]. For a sample of N Monte Carlo electrons the covariance matrix is defined as

$$M_{ij} = \frac{1}{N} \sum_{n=1}^{N} (x_i^n - \overline{x}_i)(x_j^n - \overline{x}_j),$$

where x_i^n is the ith variable of nth electron. There are altogether 41 variables used in the covariance matrix: the fraction of energy in layer 1, 2, and 4 of the EM calorimeter, the fraction of energy in each of the cells in a 6×6 square of EM3 cells centered on the hottest tower, the logarithm of the cluster energy, and the vertex position.

A χ^2-like quantity can then be defined for each electron shower

$$\chi^2_{hm} = \sum_{i,j=1}^{41} (x'_i - \overline{x}_i)\, H_{ij}\, (x'_j - \overline{x}_j), \tag{3.10}$$

where x'_i is the ith variable and the H-matrix $H = \mathbf{M}^{-1}$. χ^2_{hm} is used to measure how consistent a shower shape is with an electron shower. Because the variables are not normally distributed, in general χ^2_{hm} does not follow a χ^2 distribution. Figure 3.11 shows the distribution of χ^2_{hm} for electron candidates from $Z \to ee$ events, and for electron candidates from multijet events.

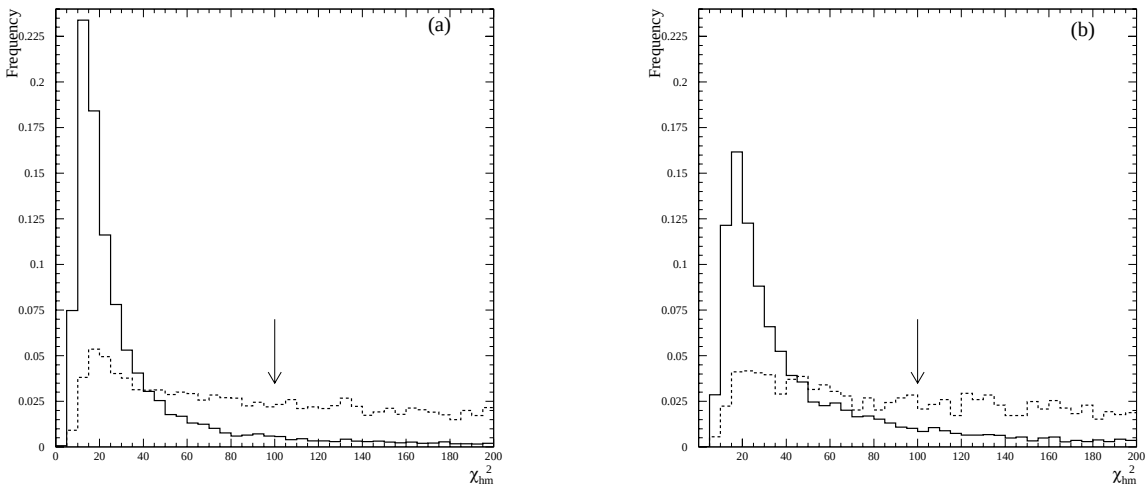

Figure 3.11 Shower shape H-matrix chi-squared (χ^2_{hm}) of electron candidates from $Z \to ee$ events (solid) and from multijet triggered data (dashed), for (a) central electrons and (b) forward electrons. The arrows in the plots indicate the "standard" cut used in other DØ analyses.

3.7.3.3 Track energy loss per unit path length (dE/dx)

In the tracking chambers charged heavy particles lose their energies faster than electrons, yielding a larger dE/dx. For $\gamma \to e^+e^-$ conversion where one of the tracks is not resolved, its dE/dx would be just twice as much as that of one electron. Thus dE/dx in the tracking chamber is a useful variable to distinguish electrons from hadrons and photons. The dE/dx distributions for electron and background are shown in Reference [37].

3.7.3.4 Track match significance (σ_{trk})

By projecting the track to the EM3 layer, where EM shower centroid $\vec{x}_{cog}$ (see Equation 3.8) is most likely to reside, we can calculate the track-shower match significance

$$\sigma_{trk} = \frac{\Delta z}{\delta z} \oplus \frac{\Delta \phi}{\delta \phi}, \tag{3.11}$$

in the CC, and

$$\sigma_{trk} = \frac{\Delta r}{\delta r} \oplus \frac{\Delta \phi}{\delta \phi}, \tag{3.12}$$

in the EC. Here Δz, $\Delta \phi$, and Δr are distance in corresponding directions between the track projection and the EM centroid in EM3, while δz, $\delta \phi$, and δr are the corresponding resolutions.

For an electron, its track should well match the center of its shower. For a photon misidentified as an electron or a π° decayed to a pair of photons, because a random track is in road, the match is expected to be poor. Figure 3.12 shows the distribution of σ_{trk} for electron candidates from $Z \to ee$ events, and for electron candidates from multijet events.

3.7.3.5 TRD transition efficiency (ε_{TRD})

With E_i as the energy measured in ith layer of TRD (recall there are three TRD layers, see section 3.3.2), we define the truncated energy as

$$E_{truc} = E_1 + E_2 + E_3 - \max(E_1, E_2, E_3). \tag{3.13}$$

The distribution of E_{truc}, ($\frac{\delta N}{\delta E_{truc}}$), is measured from a sample of $W \to e\nu$ events. Then the TRD transition efficiency, ε_{TRD}, of an EM cluster is defined as the cumulative probability of the measured truncated energy

$$\varepsilon_{TRD} = \frac{\int_{E_{truc}}^{\infty} \frac{\delta N}{\delta E} dE}{\int_{0}^{\infty} \frac{\delta N}{\delta E} dE}. \tag{3.14}$$

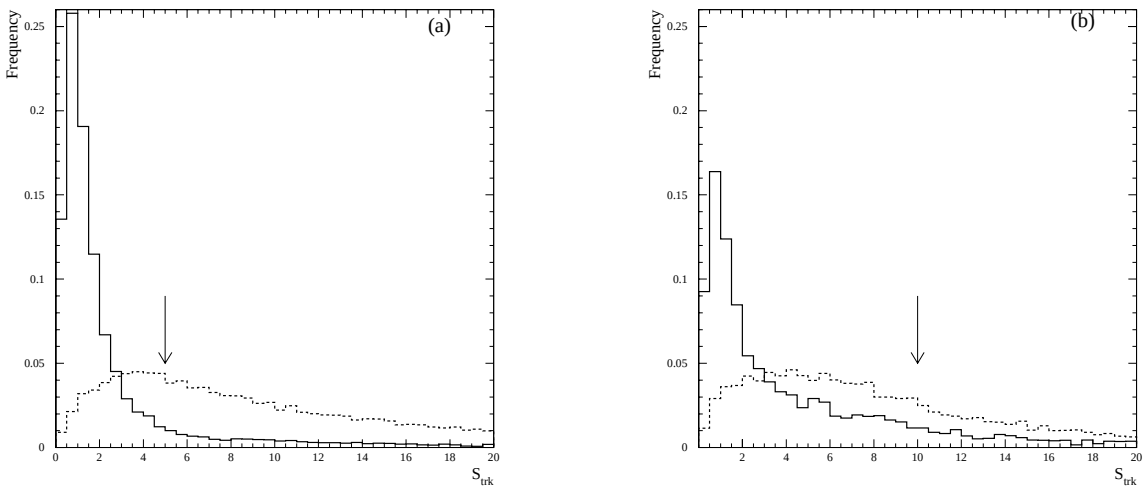

Figure 3.12 Track match significance (σ_{trk}) of electron candidates from $Z \rightarrow ee$ events (solid) and from multijet triggered data (dashed), for (a) central electrons and (b) forward electrons. The arrows in the plots indicate the "standard" cut used in other DØ analyses.

Because charged hadrons leave little transition energy in TRD their E_{truc} essentially peaks at zero. Correspondingly their ε_{TRD} distribution peaks at 1. Electrons, on the other hand, leave significant radiation in TRD. Their ε_{TRD} distribution is flat [37].

3.7.3.6 Electron likelihood

Each of the five identification variables discussed above has distinguishing power in selecting electron against backgrounds. Some analyses selected electrons by cutting directly on the variables, such as those "standard" cuts shown in Figure 3.10–3.12. However, electron and background may not be separated exclusively by a five-dimension box, making straight cuts on several dimensions less optimal. In order to have an optimal discrimination of electron against background, a likelihood ratio is defined

$$L^e = \frac{p(\vec{x}|b)}{p(\vec{x}|e)}, \tag{3.15}$$

where $p(\vec{x}|b)$ and $p(\vec{x}|e)$ are the likelihood of the variable vector $\vec{x}$, given that they come from

background and from electron, respectively. L^e is called the "electron likelihood" even though it is actually a likelihood ratio. It is found that to a good approximation these five identification variables are independent of each other [38]. Thus $p(\vec{x}|H)$ can be written as

$$p(\vec{x}|H) = p_1(f_{em}|H) \times p_2(\chi^2_{hm}|H) \times p_3(dE/dx|H) \times p_4(\sigma_{trk}|H) \times p_5(\varepsilon_{TRD}|H), \tag{3.16}$$

where H can be b (background) or e (electron).

The last multiplication in Equation 3.16 is not included for EC electrons because we do not have TRD coverage in the EC region. L^e is used to select our electron events (see Chapter 4). The efficiency of L^e cut is discussed in detail in Chapter 5.

3.7.3.7 Electron isolation fraction

There is one more variable which helps distinguish electron from background. It is called the electron isolation fraction, f_{iso}, and is defined as

$$f_{iso} = \frac{E^{tot}_{0.4} - E^{EM}_{0.2}}{E^{EM}_{0.2}}, \tag{3.17}$$

where $E^{tot}_{0.4}$ ($E^{EM}_{0.2}$) is the total energy (EM energy) in a cone of size 0.4 (0.2) in $\eta - \phi$ space around the centroid of an EM cluster.

This variable is useful in selecting isolated electrons, e.g., those from W decay. It is not included in the electron likelihood because f_{iso} is not really a measure of the electron cluster but rather its environment and is therefore rather sensitive to the physics process being studied. Figure 3.13 shows the distribution of f_{iso} for electron candidates from $Z \to ee$ events, and for electron candidates from multijet events.

3.7.4 Jet Reconstruction

The jets are reconstructed by the following algorithm:

1. From the list of calorimeter readout towers (size $\Delta\eta \times \Delta\phi = 0.1 \times 0.1$), select those which have E_T above 1 GeV as seeds.

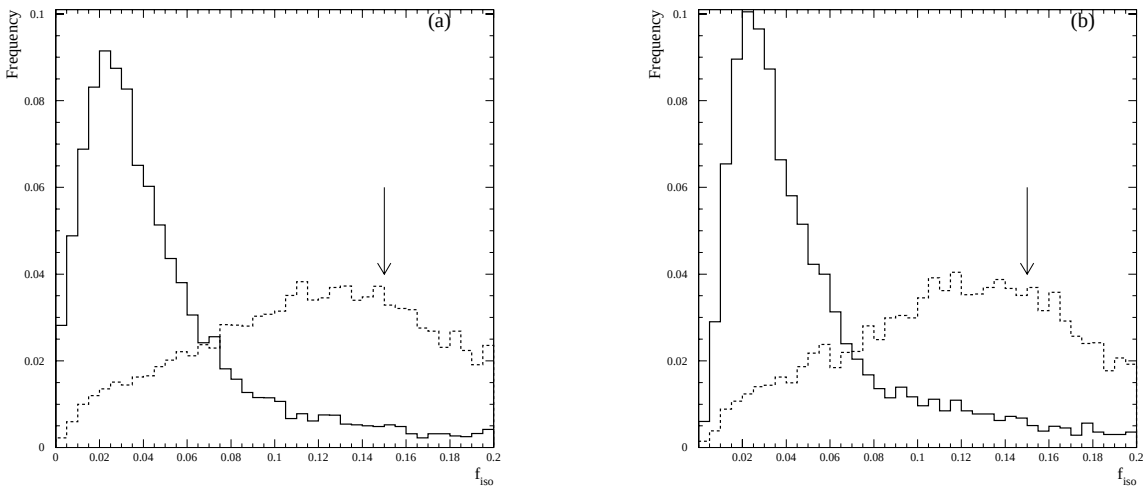

Figure 3.13 Electron isolation fraction ($fiso$) of electron candidates from $Z \rightarrow ee$ events (solid) and from multijet triggered data (dashed), for (a) central electrons and (b) forward electrons. The arrows in the plots indicate the "standard" cut used in other DØ analyses.

2. Beginning with the highest-E_T seed on the list. All towers within ± 3 units in η and ϕ adjacent to the seed are pre-clustered together. Any other seeds inside this area are considered part of this pre-cluster and are removed from the list. Energies in the area are added and a E_T-weighted (η, ϕ) centroid is calculated from the component towers.

3. Repeat step 2 until all seeds have been examined. Sort the pre-clusters in decreasing order in E_T.

4. For each pre-cluster, calculate a new E_T-weighted (η, ϕ) centroid using all towers within a cone of specific radius R (jet cone size) centered around the starting pre-cluster. We use $R = 0.5$ in this analysis. From the new centroid we draw a new cone of radius R and calculate yet a even newer centroid. This process is repeated until the centroid stabilizes, i.e., until $\Delta R < 0.01$. The resulting clusters are jets.

5. Drop those jets which have E_T less than 8 GeV.

6. Recalculate jet variables using the towers in the cone:

$$E_i^{jet} = \sum_k^{\text{towers}} E_i^k, \tag{3.18}$$

where $i = x$, y, z, and total. The three-vector components of each tower are defined with respect to the primary vertex found by DØRECO. The jet E_T is defined as the scalar sum of the tower E_T's

$$E_T^{jet} = \sum_k^{\text{towers}} E_T^k. \tag{3.19}$$

From the three-vector components the jet angles are defined as

$$\phi^{jet} = \arctan\left(\frac{E_y^{jet}}{E_x^{jet}}\right), \tag{3.20}$$

$$\theta^{jet} = \arccos\left(\frac{E_z^{jet}}{\sqrt{(E_x^{jet})^2 + (E_y^{jet})^2 + (E_z^{jet})^2}}\right), \tag{3.21}$$

$$\eta^{jet} = -\ln\left[\tan\left(\frac{\theta^{jet}}{2}\right)\right]. \tag{3.22}$$

Besides jet kinetic variables, the fractions of jet energy and E_T in the EM, FH, and CH calorimeters are calculated. These variables are important quality variables in identifying jets (see Chapter 5).

7. Jets can be merged or split based on the fractional energy shared relative to the lower E_T jet. If the shared energy is greater than 50% the jets are merged, otherwise the jets are split. For split jets, each shared cell is assigned to the nearest jet. In either case, the jet kinematic and identification variables are recalculated.

8. Since jets are collimated showers of low energy particles, the energy measured in the calorimeter is not the actual energy of the jet. An energy scale is derived at DØ to correct jet energy to the particle energy [39]. The correction takes into account the effects

of calorimeter response, calorimeter noise, event pile-up, leakage out of jet cone, and underlying event [3].

3.7.5 Muon Reconstruction

Muon candidates are reconstructed in four steps: hit sorting, track finding, quality determination, and global quality determination.

Hit sorting takes raw data and converts hits into points in the DØ coordinate system. Pattern recognition algorithms then find hits which are consistent with passage of a single particle through the muon chambers.

Track segments are constructed in muon PDT layers (see section 3.5). At least two hits in layer A and 4 hits in layer B and C together are required for each track segment. The nearby track segments are combined to form track candidates. For each track candidate, MIP traces are searched for in the hadronic layers of the calorimeter in a wide road of the primary vertex. If layers do not contain energy, searches are conducted in roads formed from secondary vertices. For tracks confirmed by the calorimeter, a road is formed in the central tracking chambers to search for a matching track. At each stage of the track finding, a set of quantities defining the quality of the track is calculated.

The combined information on vertex, the best matching central track, the muon track in the calorimeter, and the tracks in the muon spectrometer are put in a global fit. Sixteen data points are fit to seven parameters. The sixteen data points include the vertex position in the x and y direction, the angles and positions of track segments, and two angles representing the multiple scattering of the muon in the calorimeter. Of the seven parameters, four describe the position and angle of the track before the calorimeter, two describe the effects due to multiple scattering and the last is the inverse of the muon momentum [34].

Many variables can be used to enhance the muon selection purity against background. Those used in this analysis are

[3] An underlying event is usually caused by interactions between the spectator quarks and interactions between the spectator quark and the hard scattering quark.

- the quality word of the global track fit (IFW4). The smaller the IFW4 means the better the track fit quality;
- A-stub veto, which requires that the track has hits in the B or C layer;
- verification from calorimeter of associated energy deposition consistent with that of a MIP track [40]). Two particular variables are examined: the fraction of hadronic calorimeter layers containing energy deposits along the path of the muon track (HFrac) and the fraction of energy deposited in the outermost layer of the hadronic calorimeter (EFracH1) along the track;
- magnetic field integral along the path of muon trajectory ($\int B \cdot dL$). A smaller $\int B \cdot dL$ usually results from a muon which does not traverse enough magnetic field. The momentum of such a muon is poorly measured; and,
- the track impact parameter.

3.7.6 $\not\!\!E_T$ reconstruction

The $\not\!\!E_T$ algorithm used in DØRECO is the same as that used at Level 2. All energies in the calorimeter and ICD cells are summed vectorially. And $\not\!\!E_T$ is calculated as

$$\vec{\not\!\!E}_T = -\sum_i \vec{E}_{T\,i}, \tag{3.23}$$

where i sums over all cells. Measured from minimum bias data, the $\not\!\!E_T$ resolution is 1.08 GeV + $0.019(\sum_i E_{T\,i})$, where $\sum_i E_{T\,i}$ is the scalar sum of the transverse energies of all cells.

4 INITIAL DATA SELECTION

4.1 Trigger

The data used in this analysis were taken by the DØ collaboration during the 1995-1996 run. The data were reprocessed through an utility called "DØ fix" [1]. We require events to pass ELE_JET_HIGH trigger for Run 1b and the first period of Run 1c, and ELE_JET_HIGHA trigger for the second period of Run 1c. The total luminosity is 107.6 ± 5.7 pb^{-1}. The details of the trigger are listed in Table 4.1.

4.2 Initial Offline Data Selection

There are three categories of initial cuts: data cleaning cuts, object kinematic and fiducial cuts and object ID cuts.

4.2.1 Data Cleaning Cuts

Because the main ring passed through the DØ Run 1 calorimeter, it often led to large energy deposits in the calorimeter when beams were injected into the Tevatron. Large beam loss in the main ring could also result in energy deposits which were not related to $p\overline{p}$ collisions in the calorimeter. We applied MRBS_LOSS [2] and MICRO_BLANK [3] offline vetoes on our data. Since the MISSING_ET (Run 1b) and MISSING_ET_HIGH (Run 1c) triggers had these two vetoes applied online and the two triggers were always turned on during the respective runs,

[1] We used the "DØ fixed" data because there was an improvement in the electron tracking algorithm in the reconstruction program which resulted in higher electron efficiency. There was also significant improvement in muon identification efficiency.

[2] MRBS_LOSS is "true" if the event was taken within 400 ms of beam injection.

[3] MICRO_BLANK is "true" if the event was taken within 1.6 μs when the main ring beam passed through calorimeter.

we measured the luminosity from these two triggers using the luminosity database. The result is 89.9 pb^{-1}. Since our luminosity database was built, a new total inelastic cross section was measured by E811. Taking that into account, the DØ luminosity should be scaled up by 1.031. The error on the luminosity is 4.4% [43]. Our final data luminosity is then 92.7 ± 4.1 pb^{-1}.

4.2.2 Object Kinematic and Fiducial Cuts

We impose the following requirements on the data events:

- electron:
  - One "tight" electron (see next section for definition) with $E_T^e > 20$ GeV
  - $|\eta_d^e| < 1.1$ (CC) or $1.5 < |\eta_d^e| < 2.5$ (EC) [4]
  - $|\eta^e| < 2.0$ [5]
  - No extra "loose" electron (see next section for definition) with $E_T > 15$ GeV in CC or EC;
- jets (cone size = 0.5):
  - Four or more "good" jets (see next section for definition) with $E_T^j > 15$ GeV [6]
  - $|\eta_d^j| < 2.5$
  - $\Delta r_{e-j} > 0.5$ in $\eta - \phi$ space, where the electron is required to pass tight ID cuts;
- $\not\!\!E_T > 25$ GeV [7];

[4] DØ has good EM object coverage in these two regions.

[5] We required this cut in order to reduce the QCD multijet background in the EC region.

[6] All events were processed through "CAFIX" to calibrate the energies of the objects in the event. Due to a bug in the code, the jet energy wasn't calculated correctly after it was "CAFIX'ed" in the "DØ fixed" data. We corrected the jet energy by Equation 4.1 [43]. The correction factor f_{corr} is listed in the table below. The jet *emf*, *icdf* and *chf* were corrected accordingly. These corrections were performed before any jet cut.

$$E_{corr}^j = E_{reco}^j \times f_{corr} \tag{4.1}$$

η_d^j	$-2.5 < \eta_d^j < -1.4$	$-1.4 \leq \eta_d^j \leq -0.8$	$-0.8 < \eta_d^j < 0.8$	$0.8 \leq \eta_d^j \leq 1.4$	$1.4 < \eta_d^j < 2.5$
f_{corr}	0.9426	0.9476	0.9527	0.9536	0.9544

[7] $\not\!\!E_T$ is taken from PNUT(4), the calorimeter $\not\!\!E_T$ without muon P_T correction.

- No isolated tight muons (see below) with $P_T^{\mu} > 4$ GeV/c.

We also require all CC electrons to be away from ϕ-cracks between the calorimeter modules by 5% of the width of the EM calorimeter module: $0.05 < \Delta\phi_{crack} < 0.95$, where $\Delta\phi_{crack}$ is defined as:

$$\Delta\phi_{e-crack} = \mathrm{MOD}(\frac{32}{2\pi}\phi_{\mathrm{e}}, 1). \tag{4.2}$$

4.2.3 Object ID Cuts

- "Tight" electron definition:
  - CC EM: $L_5^e < 0.5$, EC EM: $L_4^e < 0.3$,

    where L_5^e is the 5-variable electron likelihood. The electron likelihood is defined in section 3.7.3.6. Since the TRD does not cover the EC region, we only use the first 4 variables to construct electron likelihood, L_4^e, for the EC EM objects.
  - $f_{iso} < 0.1$,

    where the isolation fraction f_{iso} is defined in section 3.7.3.7.
- "Loose" electron definition [8]
  - $L_5^e < 1.0$ for CC or $L_4^e < 1.0$ for EC EM object
  - $f_{iso} < 0.3$
- "Good" jet definition: We used two jet quality variables: *emf* and *chf*, the fraction of jet E_T in the EM and Coarse Hadronic calorimeter respectively to identify good jets. We required *emf* < 0.95 and *chf* < 0.4 for all jets. Additional cuts are:
  - For CC jets ($|\eta_d^j| < 1.0$)
    - if $15 < E_T^j < 25$ GeV, *emf* > 0.2;
    - if $25 < E_T^j < 30$ GeV, *emf* > 0.15;

[8] This definition is the same as the "good" electron definition used in the dilepton analysis. Thus, this analysis is orthogonal to the dilepton analysis.

    * if $30 < E_T^j < 35$ GeV, $emf > 0.1$;
    * if $E_T^j > 35$ GeV, $emf > 0.05$.
  - For ICR jets ($1.0 < |\eta_d^j| < 1.5$) there is no additional cut.
  - For EC jets ($1.5 < |\eta_d^j| < 2.5$) $emf > 0.05$.

- Isolated tight muon definition [9]:
  - QUAD ≤ 4 (CC muon) or $5 \leq$ QUAD ≤ 12 (EC muon);
  - IFW4 ≤ 1 for CC muon or IFW4 $= 0$ for EC muon in events with run number $\geq$ 89000 [10];
  - A-Stub veto;
  - HFrac $= 1$ or HFrac ≥ 0.6 and EfracH1 ≥ 0;
  - $\int B \cdot dL > 0.55$;
  - 3D impact parameter < 20 cm;
  - separated from all reconstructed jets by 0.5 in $\eta - \phi$ space.

4.2.4 Vertex Cut

We require $|z_{vertex}| \leq 60$ cm, where z_{vertex} is the interaction vertex determined by the DØRECO program.

4.2.5 Conclusion

After applying the initial selection to the data, we are left with 72 events. The major SM backgrounds are as follows:

- Physics backgrounds:

[9] We used the same definition as in the $t\bar{t}$ cross section analysis [44]. The description of these muon ID variables can be found in section 3.7.5

[10] Due to out-gassing of organic binding material in the muon cathode boards the muon chamber sense wires were covered with a insulating film. This led to poor muon identification efficiency in the EC. A short and high current impulse, known as "zapping", was applied to the sense wires to clean up the covering film just before run 89000.

- $W+ \geq 4$ jets $\rightarrow e + \nu + \geq 4$ jets
- $t\bar{t} \rightarrow Wb\,Wb \rightarrow e + \nu + \geq 4$ jets
- $WW+ \geq 2$ jets $\rightarrow e + \nu + \geq 4$ jets

- Instrumental background:
  - QCD ≥ 5 jet events with one jet faking an electron and the jet energies fluctuating to give rise to $\not{E}_T$.

Table 4.1 Triggers used for the electron channel analysis. The Level 2 "electron" requires the EM object passes the electron transverse and longitudinal shower shape cut. The EM1_EISTRKCC_MS triggered data are used for background study (see Chapter 7).

Trigger Name	Exposure (pb^{-1})	Level 1		Level 2	
EM1_EISTRKCC_MS (Run 1b)	89.9	1EM tower:	$E_T > 10$ GeV $\|\eta\| < 2.5$	1 electron:	$E_T > 15$ GeV w/track
		1 jet tower:	$E_T > 3$ GeV	$\not\!\!E_T^{cal} > 15$ GeV [a]	
		1 EX tower [b]:	$E_T > 15$ GeV $\|\eta\| < 0.85$		
ELE_JET_HIGH (Run 1b)	95.4	1EM tower:	$E_T > 12$ GeV $\|\eta\| < 2.6$	1 electron:	$E_T > 15$ GeV $\|\eta\| < 2.5$
		2 jet towers:	$E_T > 5$ GeV $\|\eta\| < 2.0$	2 jets (0.3-cone):	$E_T > 10$ GeV $\|\eta\| < 2.5$
				$\not\!\!E_T^{cal} > 14$ GeV	
ELE_JET_HIGH (Run 1c)	1.77	ditto		ditto	
ELE_JET_HIGHA (Run 1c)	10.5	ditto		1 electron:	$E_T > 17$ GeV $\|\eta\| < 2.5$
				ditto for the jets and $\not\!\!E_T^{cal}$	

[a] $\not\!\!E_T^{cal}$ was calculated using energy deposited in the calorimeter only. Some particles, e.g., muons, do not deposit much energy in the calorimeter. Although the momenta of the muons are measured in the muon chamber, their momenta were not included in calculating $\not\!\!E_T^{cal}$.

[b] EX denotes Level 1.5 electron trigger.

5 ELECTRON AND JET IDENTIFICATION EFFICIENCY

5.1 Electron Identification Efficiency

The electron identification (ID) efficiency was measured using $Z \to ee$ data. Run 1b data passing the EM2_EIS_ELE filter were streamed requiring one PELC [1] with $E_T > 18$ GeV. In order to select real electrons for efficiency measurement, we plotted the invariant mass of the two leading EM objects. For $Z \to ee$ events, the invariant mass spectrum should peak around the Z mass. Events in the Z-mass window, (82,102) GeV, were considered as signal candidates for efficiency calculation. Two sub-samples were constructed. One is called the parent sample in which we required one EM object to satisfy $L_5^e < 0.5$ for CC EM (or $L_4^e < 0.5$ for EC EM) and $f_{iso} < 0.15$. These requirements greatly reduced the Drell-Yan background, which is the major contamination to our signal. We then made our daughter sample by applying ID cuts on the other EM object. There are still background events left in both samples. We estimate their numbers by using the method described below. After subtracting the number of background events from the number of candidate signal events in the Z-mass window, we obtained the number of electrons in both parent and daughter samples. The electron identification efficiency (ε_{eid}) is then defined in Equation 5.1. The statistical error on the efficiency is binomial. An example of this method is shown in Figure 5.1.

$$\varepsilon_{eid} = \frac{N_{daughter}}{N_{parent}}. \tag{5.1}$$

The background in the Z-mass window in the parent and daughter samples was estimated by the side-band method. We constructed two side-bands on each side of the Z-mass window,

[1] A PELC is an EM object with a track in road to the reconstructed hard-interaction vertex. It's considered an electron candidate.

each with one half of the width of Z-mass window, (71,81) and (101-111) GeV. The Drell-Yan background has an exponential distribution in terms of di-electron mass but can be well approximated with a linear function in this mass range. Thus, the expected number of background events in the Z-mass window is simply the sum of number of events in the two side-bands [2].

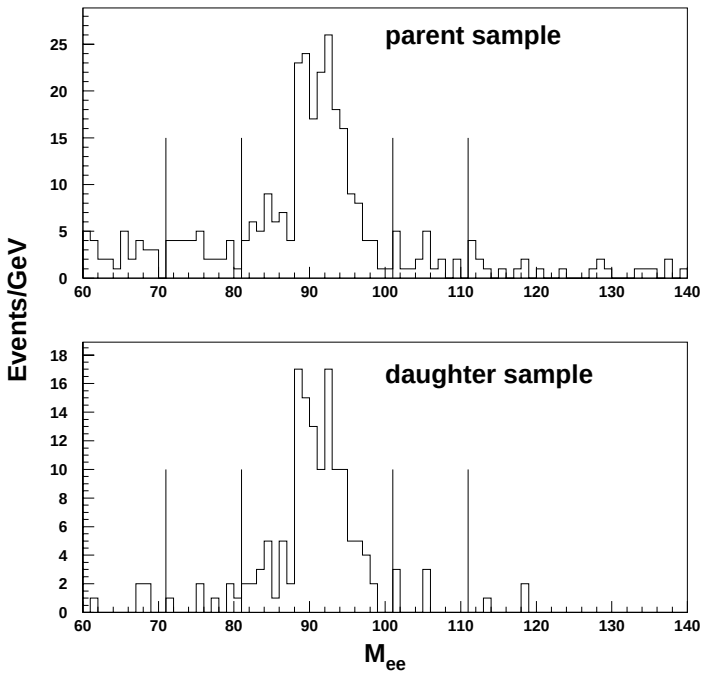

Figure 5.1 Method of measuring electron identification efficiency. The two regions between the lines on either side of the signal region, (81,101) GeV, are the side-bands for background calculation (see text).

To estimate the systematic error of our measurement we used an alternative method. We again prepared two samples, one requiring that both EM objects passed ID cuts (N_2) and the other requiring one and only one EM object passed ID cuts (N_1). The ID efficiency is then:

$$\varepsilon_{eid} = \frac{2 \times N_2}{2 \times N_2 + N_1}. \tag{5.2}$$

[2]We assumed that no signal events were present in the side-bands.

The difference between the ε_{eid} derived by the nominal and alternative methods was assigned as systematic error. Note, the alternative method was only used for the CC-CC events which had large statistics. For EC electrons we used two different side-bands, (61,71) and (111,121) GeV, to estimate the systematic error. We also used different side-bands on the CC ε_{eid} measurement but found the difference to be smaller than that between the nominal and alternative ε_{eid}.

Figure 5.2 shows the ε_{eid} distribution as a function of *eid* cuts. For CC electron the ε_{eid} is also a function of jet multiplicity. The presence of jets confuses the reconstruction program, which leads to lower ε_{eid}. However, with higher number of jets (≥ 3) in the event, the inefficiency of locating the correct hard scattering vertex becomes smaller. This is reflected in the left plot in Figure 5.2 as the ε_{eid}^{CC} saturates at a jet multiplicity equal to 2 or more. Because in EC the electron tracking efficiency is higher and jets are more likely in the CC, the ε_{eid}^{EC} is not affected by the presence of jets. The ε_{eid} we used for our 4-jet final state were derived from the sample with 2 or more jets and are listed in Table 5.1.

Table 5.1 Electron ID efficiency used in this analysis. The electron likelihood cuts are $L_5^e < 0.5$ for CC electrons and $L_4^e < 0.3$ for EC electrons.

Detector Region	CC	EC
ε_{eid}	0.674 ± 0.039	0.242 ± 0.075

5.2 Jet Identification Efficiency

The ID efficiency for 0.5-cone jets was measured for Run 1a data. Since there were many hardware and software improvements during Run 1b [45], the Run 1b jets are much cleaner. This section describes a new set of jet ID cuts pertaining to Run 1b 0.5-cone jets. We followed the conventional procedure the QCD group used to derive the 0.7-cone jet ID efficiency [46]. The data ntuples were the standard Run 1b QCD ntuples (unfixed data). We first restored the AIDA

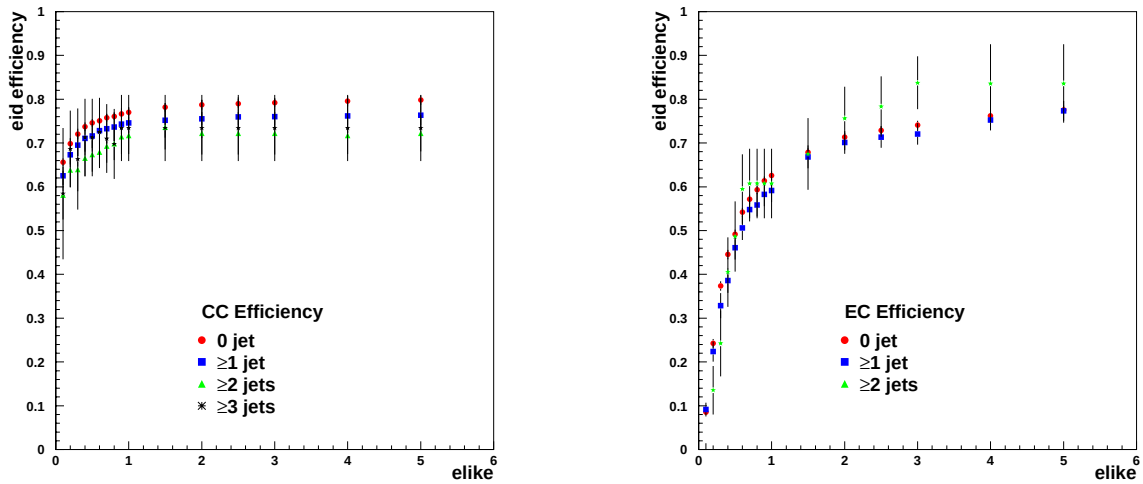

Figure 5.2 CC (left) and EC (right) electron efficiency as a function of *eid* cuts and the number of jets present in the event.

cells [3] in the jets and recalculated the event $\not\!\!E_T$ for each vertex found by DØ reconstruction program. The vertex corresponding to the smallest $\not\!\!E_T$ was chosen as the hard scattering vertex. We required this new vertex to satisfy $|z_{vertex}| < 60$ cm. The jet variables we examined were *emf* (the fractional jet E_T in EM calorimeter), *chf* (the fractional jet E_T in the coarse hadronic calorimeter), and *hcf* (the ratio in E_T of the second hottest cell to the hottest cell in the jet). Because the noise level and the calorimeter components are different in CC, ICR and EC regions, the efficiencies were measured separately in each of the three regions. We define:

$$CC: \quad |\eta_d^j| < 1.0;$$

$$ICR: \quad 1.0 < |\eta_d^j| < 1.5;$$

$$EC: \quad 1.5 < |\eta_d^j| < 2.5.$$

[3] AIDA cells are those calorimeter cells which were considered as hot cells by online AIDA hot cell algorithm but were later determined to be normal cells with large energy deposition.

5.2.1 CC Jet *emf* Efficiency

Usually a quark or a gluon jet deposits a significant fraction of its energy in the hadronic calorimeter while an electron or a photon deposits a large fraction of its energy in the EM calorimeter. We therefore expect that a quark or a gluon jet would have a moderate *emf*. Figure 5.3 shows the raw distribution of jet *emf* at different jet E_T. Only the $|z_{vertex}| < 60$ cm cut was applied in the plots. In order to obtain a clean sample we apply the R_{MET} cut to our sample. R_{MET} is defined as:

$$R_{\mathrm{MET}} = \frac{E_T^{j_1}}{\not{E}_T}, \tag{5.3}$$

where "j_1" stands for the leading jet [4]. Since most events in our initial data sample are di-jet events we expect that the event $\not{E}_T$ to be close to 0. For real di-jet events the only reason that they have non-zero $\not{E}_T$ is the finite jet energy resolution and limited calorimeter coverage. This is reflected by the smooth spectrum in the large R_{MET} region in Figure 5.4. The presence of fake jets creates large non-physical $\not{E}_T$ and leads to low R_{MET} as shown by the low end spectrum of R_{MET} in Figure 5.4. For low-E_T jets most fake jets arise from main ring noise while for high-E_T jets most fake jets arise from hot cells and cosmic rays. From Figure 5.4 we decided to apply a $R_{\mathrm{MET}} > 1.43$ [5] cut to clean up the sample. Figure 5.5 shows the *emf* distribution after the R_{MET} cut. To derive the *emf* cut, we plot the ratio of *emf* distribution after and before the R_{MET} cut in Figure 5.6. The R_{MET} cut should not change the *emf* distribution for good jets. The deficiency observed at low and high ends of the ratio plots tells us where the effect of fake jets is non-negligible. The lines in the plots indicate the *emf* cuts we apply to the data.

We calculate the *emf* cut efficiency from the *emf* distribution cleaned up by the R_{MET} cut. We count N_{low}, the number of events below the low *emf* cut, N_{high}, the number of events above the high *emf* cut, and N, the number of events in between. The *emf* efficiency is then defined as:

[4] Jets are ordered in E_T.

[5] This is equivalent to $1/R_{\mathrm{MET}} = \not{E}_T/E_T^{j_1} < 0.7$, the same as the conventional cut developed by the QCD group.

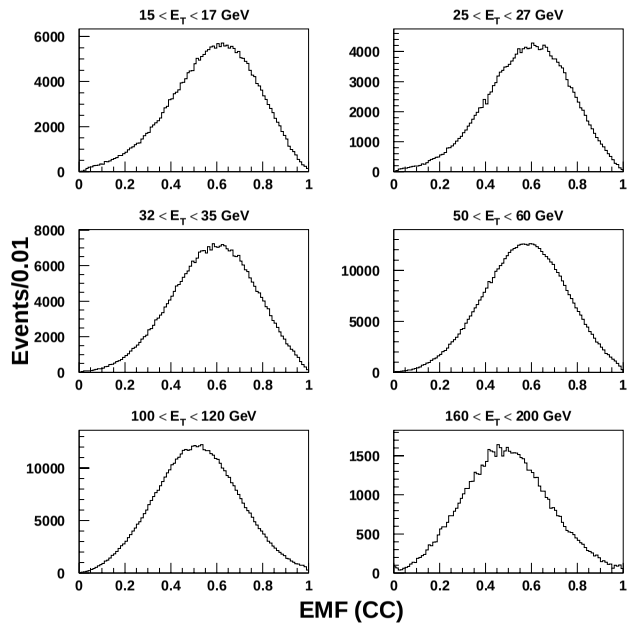

Figure 5.3 Raw CC jet *emf* distribution.

$$\varepsilon_{emf}^{jet} = \frac{N}{N + N_{low} + N_{high}}. \tag{5.4}$$

The statistical error on ε_{emf}^{jet} is binomial. The systematic error was estimated by using different methods to estimate N_{low} and N_{high}. The difference between the results obtained by these methods and the nominal was assigned as systematic error. The procedure is described in detail below and is illustrated in Figure 5.7:

- We used two methods to estimate N_{low}:
  - fit the *emf* spectrum to an empirical function: $y = p_1 x + p_2 x^2$ (method 1);
  - derive the tangential line at the cut point from the *emf* spectrum itself (method 2);
  - assuming that the clean *emf* distribution below the cut point could have either form (polynomial of second-order or a straight line), we integrate the two curves in the *emf* region where the number of events is not zero. The resulting integrals are the number of good jet events that would have been cut out at the low end;

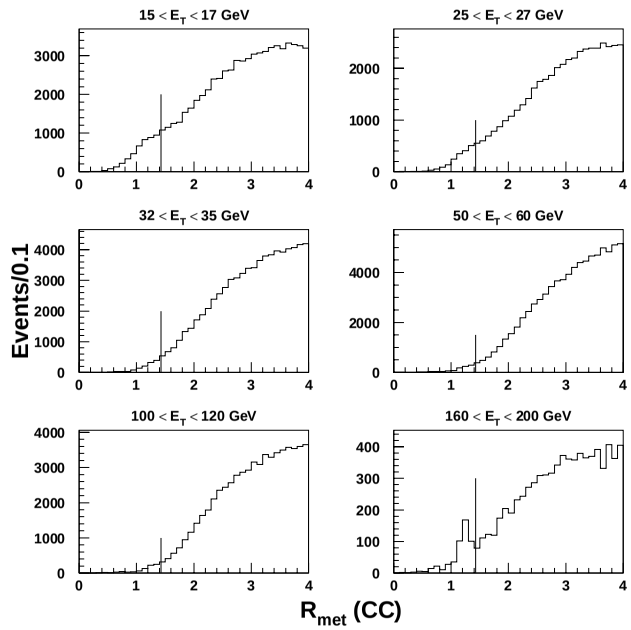

Figure 5.4 R_{MET} distribution for the CC jets. The lines indicate the R_{MET} cut ($R_{\mathrm{MET}} > 1.43$) which would be applied to clean up the sample (see text).

  - the lower number of the two integrals is used to estimate the systematic error on N_{low}.

- For the high end, we simply fit the *emf* distribution to another empirical function shown in Equation 5.5. We integrate the function from the high *emf* cut point to $emf = 1.0$ and used the integral to estimate the systematic error on N_{high}.

$$y = p_1(1-x) + p_2(1-x)^2 + p_3(1-x)^3 \tag{5.5}$$

5.2.2 CC Jet *chf* Efficiency

Because the main ring passes through the coarse hadronic calorimeter, main ring beam loss will introduce noise to our data resulting in jets with large *chf*. The effect is non-negligible even if we require our jets to be away from the main ring ϕ region. In order to identify the

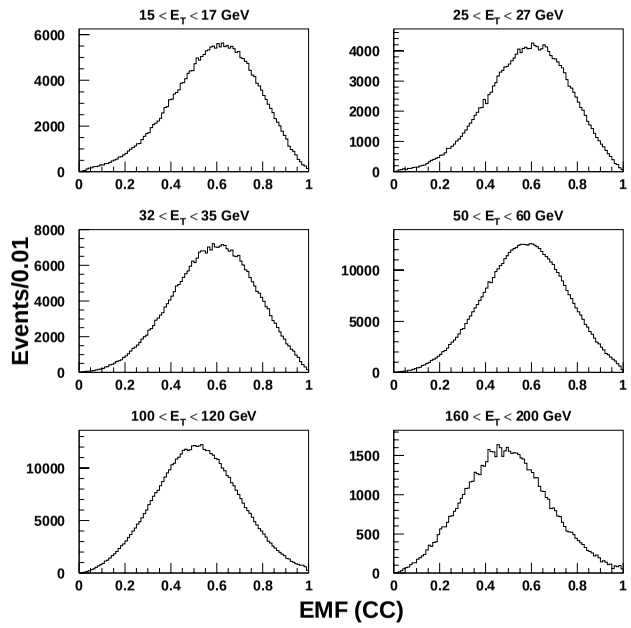

Figure 5.5 CC jet *emf* distribution after the R_{MET} cut.

noisy *chf* regions, we again use R_{MET} cut. We first required the jets to be away from the main ring: $\phi_{jet} < 1.0$ or $\phi_{jet} > 2.2$ [6]. Then two samples were produced, the first with only the *emf* cut applied and the second with both the *emf* and R_{MET} cuts applied. The ratio of the *chf* distribution of the second sample to the first sample is shown in Figure 5.8. We found that the noise starts to impact the *chf* distribution at *chf* > 0.4 for low E_T jets and at *chf* > 0.6 for high E_T jets. We chose a universal *chf* > 0.4 cut for simplicity. Figure 5.9 is the *chf* distribution after the R_{MET} cut.

We count the number of events below the cut (N_1) and the total number of events (N_{tot}) in Figure 5.9. The *chf* efficiency is then:

$$\varepsilon_{chf}^{jet} = \frac{N_1}{N_{tot}}. \tag{5.6}$$

The statistical error on ε_{chf}^{jet} is binomial. To estimate the systematic error, one more sample with jets only in the lower half of the calorimeter, i.e., $\pi < \phi_{jet} < 2\pi$ was prepared. The

[6] The Main ring is at $\phi \sim 1.6$.

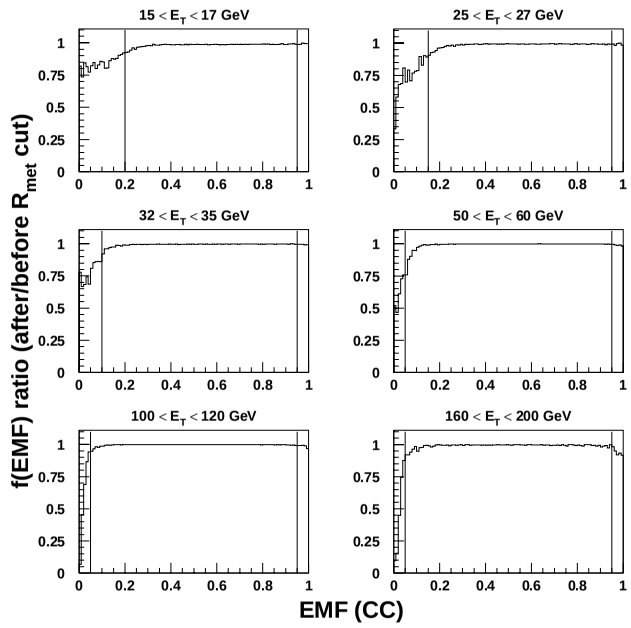

Figure 5.6 Ratio of the CC jet *emf* after and before the R_{MET} cut as a function of *emf*. The lines indicate the *emf* ID cuts applied to the data. Jets with *emf* between the lines are accepted.

efficiency of the same *chf* cut was calculated and the difference between this result and the nominal is assigned as the systematic error.

5.2.3 CC Jet *hcf* Efficiency

While we found the CC jet *emf* and *chf* distributions were virtually the same for unfixed and fixed data, the *hcf* distribution is vastly different. The difference is shown in Figure 5.10. Further examination of the jet *hcf* distribution (see Figure 5.11) shows that an *hcf* cut for the fixed data is not necessary.

5.2.4 Total CC Jet ID Efficiency

Total CC jet ID efficiency as a function of E_T^j is shown in Table 5.2 and plotted in Figure 5.12. We fit the efficiencies to two second-order polynomials as a function of E_T^j (Equation 5.7) in two different E_T^j regions. The results of the fit are shown in Table 5.3.

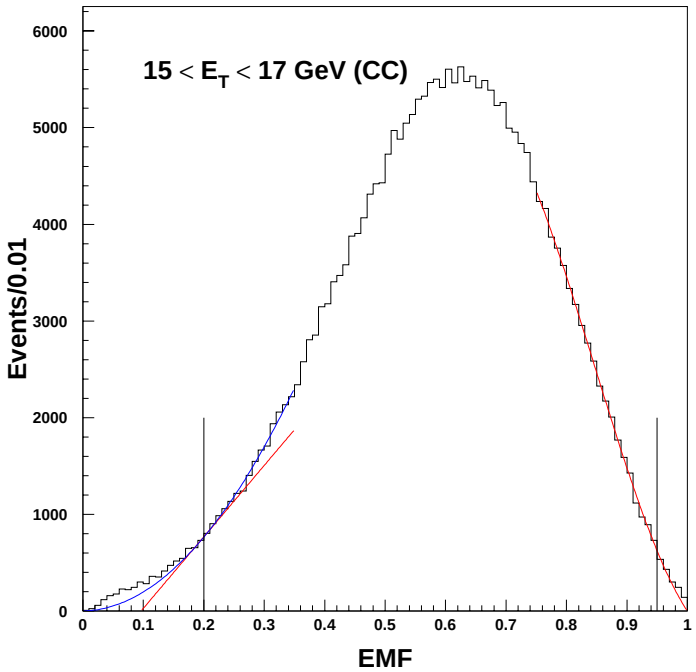

Figure 5.7 Calculating CC *emf* cut efficiency. The jets in this plot are required to pass $15\text{GeV} < \text{E}_\text{T}^\text{j} < 17\text{GeV}$. The histogram is the *emf* distribution after the R_{MET} cut. The curves are functions fitted (see text) to the *emf* within the region they are drawn. The straight line is the tangential line of the histogram at which the *emf* cut($emf > 0.2$) was applied.

$$\varepsilon_{tot}^{jet} = p_0 + p_1 \times E_T^j + p_2 \times (E_T^j)^2 \tag{5.7}$$

5.2.5 ICR Jet Efficiency

The ICR jet ID efficiency was derived the same way as the CC jet ID efficiency. Since there was virtually no EM energy coverage in the ICR, we did not apply a lower bound *emf* cut. The only cut on *emf* is $emf < 0.95$. We also raised the *chf* cut to $chf < 0.6$ because there was much less material in front of the coarse hadronic calorimeter in the ICR than in the CC and EC. The noise level in the ICR is lower than that in the CC, which allows us to use a uniform *emf*

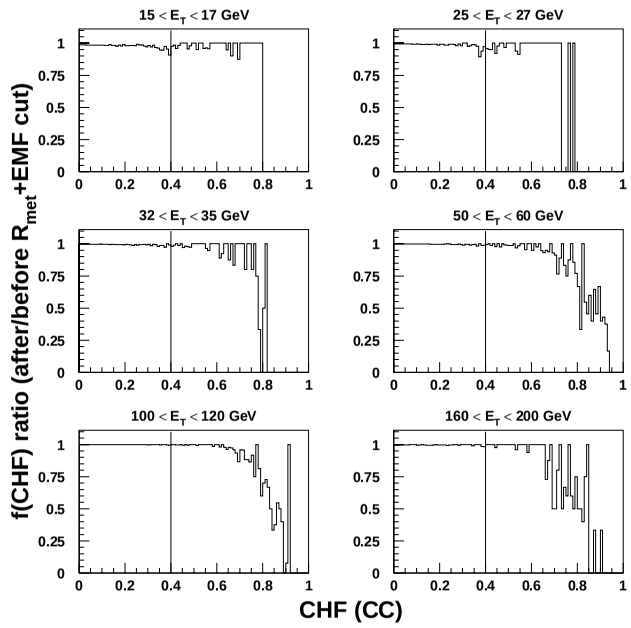

Figure 5.8 Ratio of the CC jet *chf* after and before the R_{MET} cut as a function of the jet *chf*. The lines indicate the *chf* ID cut ($chf < 0.4$) applied to the data. Both samples have had *emf* ID cuts applied.

cut even at low jet E_T. Details of the derivation are given in Appendix A. The efficiency as a function of E_T^j is listed in Table 5.4 and plotted in Figure 5.13. We again fit the efficiencies to two second-order polynomials in E_T^j (Equation 5.7) in two different E_T^j regions. The results of the fit are shown in Table 5.5.

5.2.6 EC Jet Efficiency

The EC jet ID efficiency was derived the same way as the CC and ICR jet ID efficiency. As in the ICR, the noise level in the EC is much lower than that in the CC, which allows us to have a uniform *emf* cut even at low jet E_T. Details of the derivation are given in Appendix A. The EC jet ID efficiency as a function of E_T^j is listed in Table 5.6 and plotted in Figure 5.14. We fit the efficiency to a second-order polynomial in E_T^j (Equation 5.7). The results of the fit are shown in Table 5.7.

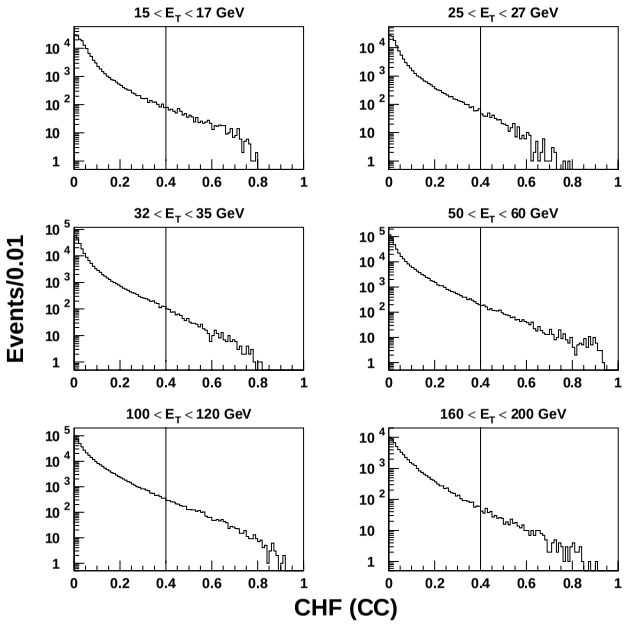

Figure 5.9 CC jet *chf* distribution after the R_{MET} and the *emf* cuts. The lines indicate the *chf* ID cut ($chf < 0.4$) applied to the data.

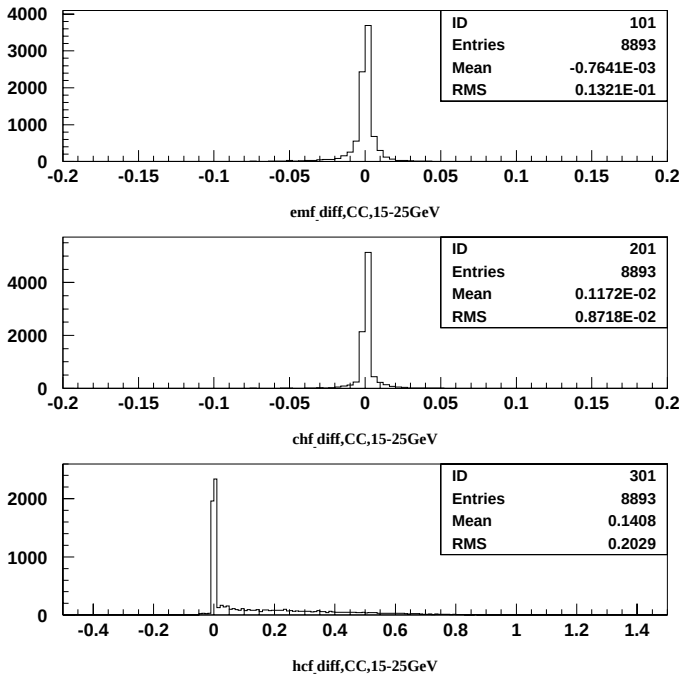

Figure 5.10 CC jet *emf*, *chf*, and *hcf* difference between the unfixed and the fixed data. The jets are from the same events from Run 1b ELE_JET_HIGH triggered data (our signal sample) and are matched to 0.1 in $\eta - \phi$ space (to ensure that they are the same jet). The jets were required to pass 15 GeV $< E_T^{jet} <$ 25 GeV. The plots indicate that while there is little difference in jet *emf* and *chf* there is a large difference in jet *hcf* between the unfixed and the fixed data.

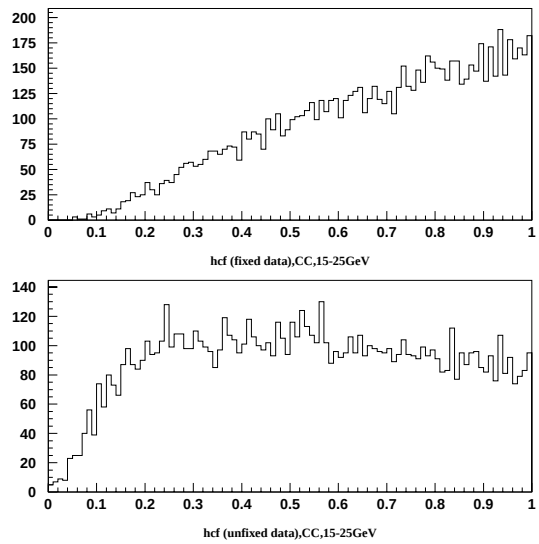

Figure 5.11 CC jet *hcf* distribution for the fixed and the unfixed data. Cut on *hcf* is not necessary for the fixed data.

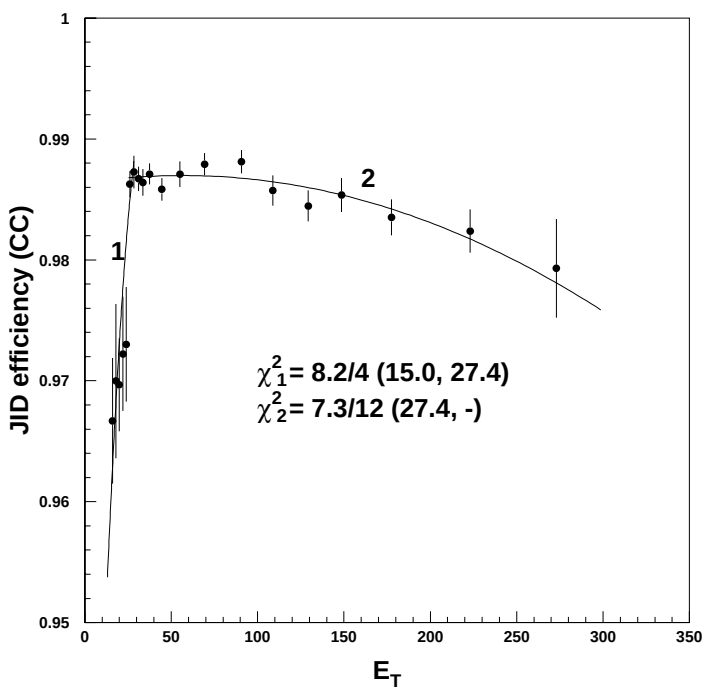

Figure 5.12 CC Jet ID efficiency as a function of E_T^j. Two second-order polynomials were used to fit the points in regions 1 and 2 respectively.

Table 5.2 CC jet ID efficiency as a function of E_T^j.

E_T^j (GeV)	ε_{emf}	ε_{chf}	ε_{total}
$15.0 - 17.0$	0.9740 ± 0.0052	0.9925 ± 0.0007	0.9667 ± 0.0052
$17.0 - 19.0$	0.9763 ± 0.0064	0.9936 ± 0.0006	0.9700 ± 0.0064
$19.0 - 21.0$	0.9751 ± 0.0038	0.9944 ± 0.0004	0.9697 ± 0.0038
$21.0 - 23.0$	0.9775 ± 0.0047	0.9946 ± 0.0004	0.9722 ± 0.0047
$23.0 - 25.0$	0.9780 ± 0.0047	0.9949 ± 0.0005	0.9730 ± 0.0047
$25.0 - 27.0$	0.9909 ± 0.0010	0.9954 ± 0.0003	0.9863 ± 0.0011
$27.0 - 30.0$	0.9919 ± 0.0013	0.9953 ± 0.0003	0.9873 ± 0.0013
$30.0 - 32.0$	0.9918 ± 0.0009	0.9948 ± 0.0004	0.9867 ± 0.0010
$32.0 - 35.0$	0.9913 ± 0.0011	0.9951 ± 0.0003	0.9864 ± 0.0011
$35.0 - 40.0$	0.9936 ± 0.0007	0.9935 ± 0.0005	0.9871 ± 0.0009
$40.0 - 50.0$	0.9941 ± 0.0007	0.9917 ± 0.0006	0.9858 ± 0.0009
$50.0 - 60.0$	0.9932 ± 0.0010	0.9938 ± 0.0003	0.9871 ± 0.0011
$60.0 - 80.0$	0.9943 ± 0.0009	0.9935 ± 0.0003	0.9879 ± 0.0009
$80.0 - 100.0$	0.9951 ± 0.0009	0.9930 ± 0.0003	0.9881 ± 0.0010
$100.0 - 120.0$	0.9946 ± 0.0012	0.9911 ± 0.0003	0.9857 ± 0.0013
$120.0 - 140.0$	0.9944 ± 0.0012	0.9900 ± 0.0004	0.9845 ± 0.0013
$140.0 - 160.0$	0.9951 ± 0.0014	0.9903 ± 0.0004	0.9854 ± 0.0014
$160.0 - 200.0$	0.9944 ± 0.0014	0.9890 ± 0.0007	0.9835 ± 0.0015
$200.0 - 250.0$	0.9940 ± 0.0014	0.9883 ± 0.0012	0.9824 ± 0.0018
$250.0 - 300.0$	0.9936 ± 0.0027	0.9856 ± 0.0031	0.9793 ± 0.0041

Table 5.3 Fitted results of CC jet ID efficiency. The two curves intersect at $E_T^j = 27.36$ GeV (see text and Figure 5.12).

E_T^j (GeV)	p_0	p_1	p_2	$\chi^2/ndof$
15–27.36	0.8994 ± 0.0070	$(5.04 \pm 0.45) \times 10^{-3}$	$(-6.7 \pm 1.0) \times 10^{-5}$	8.2/4
≥ 27.36	0.98636 ± 0.00047	$(2.16 \pm 0.57) \times 10^{-5}$	$(-1.90 \pm 0.30) \times 10^{-7}$	7.3/12

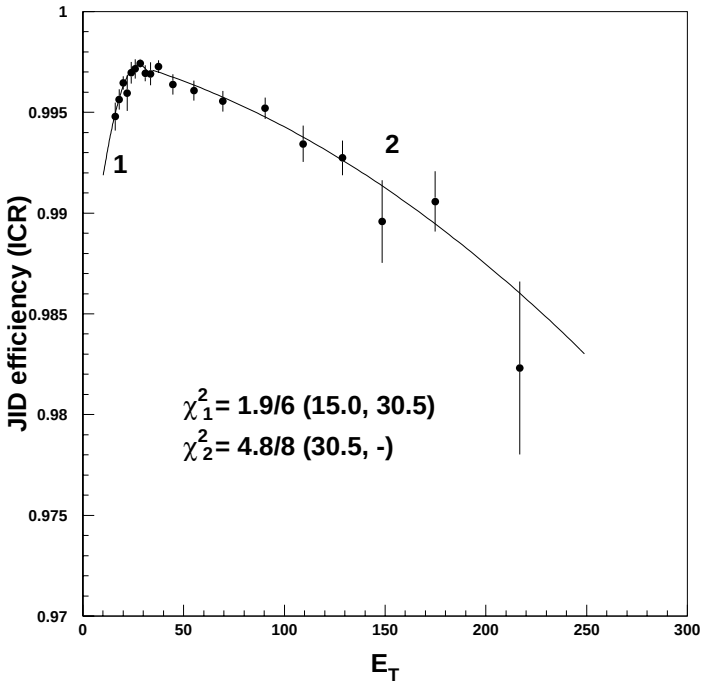

Figure 5.13 ICR Jet ID efficiency as a function of E_T^j. Two second-order polynomials were used to fit the points in region 1 and 2 respectively.

Table 5.4 ICR jet ID efficiency as a function of E_T^j.

E_T^j (GeV)	ε_{emf}	ε_{chf}	ε_{total}
$15.0 - 17.0$	0.9992 ± 0.0003	0.9956 ± 0.0006	0.9948 ± 0.0007
$17.0 - 19.0$	0.9992 ± 0.0003	0.9964 ± 0.0004	0.9956 ± 0.0005
$19.0 - 21.0$	0.9991 ± 0.0002	0.9974 ± 0.0003	0.9965 ± 0.0003
$21.0 - 23.0$	0.9990 ± 0.0006	0.9970 ± 0.0007	0.9960 ± 0.0009
$23.0 - 25.0$	0.9991 ± 0.0004	0.9979 ± 0.0003	0.9970 ± 0.0005
$25.0 - 27.0$	0.9989 ± 0.0004	0.9982 ± 0.0002	0.9972 ± 0.0005
$27.0 - 30.0$	0.9991 ± 0.0001	0.9983 ± 0.0002	0.9974 ± 0.0002
$30.0 - 32.0$	0.9989 ± 0.0003	0.9980 ± 0.0003	0.9969 ± 0.0004
$32.0 - 35.0$	0.9986 ± 0.0005	0.9983 ± 0.0002	0.9969 ± 0.0006
$35.0 - 40.0$	0.9987 ± 0.0003	0.9986 ± 0.0001	0.9973 ± 0.0003
$40.0 - 50.0$	0.9986 ± 0.0005	0.9978 ± 0.0001	0.9964 ± 0.0005
$50.0 - 60.0$	0.9984 ± 0.0005	0.9977 ± 0.0002	0.9961 ± 0.0005
$60.0 - 80.0$	0.9982 ± 0.0005	0.9974 ± 0.0002	0.9956 ± 0.0005
$80.0 - 100.0$	0.9985 ± 0.0005	0.9967 ± 0.0002	0.9952 ± 0.0005
$100.0 - 120.0$	0.9978 ± 0.0009	0.9956 ± 0.0002	0.9934 ± 0.0009
$120.0 - 140.0$	0.9980 ± 0.0008	0.9947 ± 0.0004	0.9927 ± 0.0009
$140.0 - 160.0$	0.9969 ± 0.0019	0.9926 ± 0.0008	0.9896 ± 0.0021
$160.0 - 200.0$	0.9976 ± 0.0011	0.9929 ± 0.0010	0.9906 ± 0.0015
$200.0 - 250.0$	0.9969 ± 0.0026	0.9853 ± 0.0034	0.9823 ± 0.0043

Table 5.5 Fitted results of ICR jet ID efficiency. The two curves intersect at $E_T^j = 30.46$ GeV (see text and Figure 5.14).

E_T^j (GeV)	p_0	p_1	p_2	$\chi^2/ndof$
15–30.46	0.9838 ± 0.0017	$(9.76 \pm 1.33) \times 10^{-4}$	$(-1.76 \pm 0.27) \times 10^{-5}$	1.9/6
≥ 30.46	0.9981 ± 0.00085	$(-2.27 \pm 2.26) \times 10^{-5}$	$(-1.52 \pm 1.22) \times 10^{-7}$	4.8/8

Table 5.6 EC jet ID efficiency as a function of E_T^j.

E_T^j (GeV)	ε_{emf}	ε_{chf}	ε_{total}
$15.0 - 17.0$	0.9890 ± 0.0019	0.9954 ± 0.0003	0.9844 ± 0.0019
$17.0 - 19.0$	0.9891 ± 0.0010	0.9960 ± 0.0003	0.9851 ± 0.0011
$19.0 - 21.0$	0.9888 ± 0.0004	0.9959 ± 0.0003	0.9847 ± 0.0005
$21.0 - 23.0$	0.9885 ± 0.0016	0.9964 ± 0.0003	0.9850 ± 0.0017
$23.0 - 25.0$	0.9896 ± 0.0004	0.9968 ± 0.0003	0.9863 ± 0.0005
$25.0 - 27.0$	0.9886 ± 0.0019	0.9967 ± 0.0003	0.9854 ± 0.0019
$27.0 - 30.0$	0.9893 ± 0.0009	0.9965 ± 0.0002	0.9858 ± 0.0009
$30.0 - 32.0$	0.9892 ± 0.0008	0.9966 ± 0.0003	0.9858 ± 0.0008
$32.0 - 35.0$	0.9892 ± 0.0003	0.9970 ± 0.0002	0.9862 ± 0.0004
$35.0 - 40.0$	0.9863 ± 0.0010	0.9970 ± 0.0002	0.9834 ± 0.0010
$40.0 - 50.0$	0.9860 ± 0.0010	0.9963 ± 0.0002	0.9823 ± 0.0010
$50.0 - 60.0$	0.9873 ± 0.0019	0.9969 ± 0.0002	0.9843 ± 0.0019
$60.0 - 80.0$	0.9855 ± 0.0007	0.9961 ± 0.0002	0.9817 ± 0.0007
$80.0 - 100.0$	0.9886 ± 0.0006	0.9948 ± 0.0003	0.9834 ± 0.0006
$100.0 - 120.0$	0.9871 ± 0.0004	0.9938 ± 0.0005	0.9810 ± 0.0006
$120.0 - 140.0$	0.9858 ± 0.0029	0.9921 ± 0.0010	0.9780 ± 0.0030
$140.0 - 160.0$	0.9870 ± 0.0013	0.9918 ± 0.0014	0.9789 ± 0.0019
$160.0 - 200.0$	0.9839 ± 0.0039	0.9900 ± 0.0026	0.9740 ± 0.0047

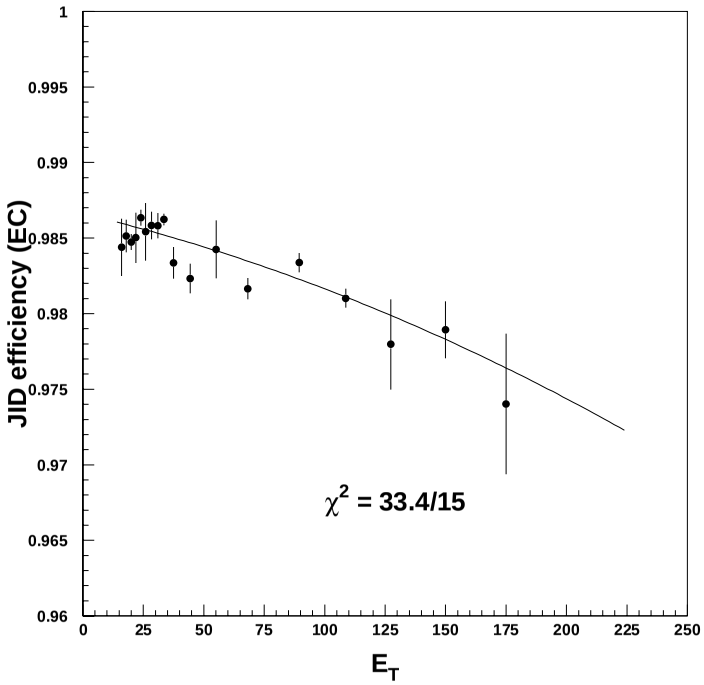

Figure 5.14 EC Jet ID efficiency. A second-order polynomial was used to fit the points.

Table 5.7 Fitted results of EC jet ID efficiency.

p_0	p_1	p_2	$\chi^2/ndof$
0.98661 ± 0.00037	$(-3.81 \pm 1.05) \times 10^{-5}$	$(-1.15 \pm 0.75) \times 10^{-7}$	33.4/15

6 FAST MONTE-CARLO

Because of the large SUSY parameter space we plan to study in this analysis, the traditional detector simulation using the GEANT package [36] is too slow. Therefore, we used a fast Monte-Carlo program called FMCØ [47]. It consists of two major parts: detector simulation and trigger simulation. The goal of FMCØ is to directly obtain the acceptance of any physics process passing our trigger and offline selection cuts. This section will discuss the details of both parts of the FMCØ package and their integration.

6.1 Detector Simulation

Detector simulation in FMCØ is done by smearing the physics objects: electrons, muons, jets, and $\not\!\!E_T$. The program is called QSIM [49] which stands for "Quick Simulation." In QSIM, stable interacting particles (not neutrinos or LSP's) which are generated by physics generator (PYTHIA [50] or HERWIG [51] for this analysis in particular) are grouped into jets by the D0pjet algorithm [1] when they hit our calorimeter or simply designated as electrons or muons if they are isolated from the jets. The energies of these objects were smeared according to their resolutions as measured from data. $\not\!\!E_T$ in QSIM was calculated based on all the smeared objects as well as the unclustered energy. Comparison of QSIM and GEANT found that the agreement between the respective jet and electron E_T spectra as well as the $\not\!\!E_T$ spectra was very good [49].

[1] The D0pjet algorithm is very similar to the cone jet algorithm which was used on data. Parameters of the algorithm were tuned to match GEANT and FMCØ acceptances. The tuning was done on PYTHIA files only since the mSUGRA signal was generated using PYTHIA.

6.2 Trigger Simulation

Because different algorithms were used in online and offline calculations of object E_T, the trigger efficiency is not a step function but has a gradual turn-on in offline E_T. Since our offline cuts fall in the region where our trigger is not fully efficient, one has to measure these turn-on curves in order to accurately calculate the acceptance of physical processes. We measured the efficiencies of all three parts – ELE, JET, and MS of our signal trigger ELE_JET_HIGH for Run 1b and ELE_JET_HIGHA for Run 1c. (The trigger definitions are listed in Table 4.1.)

6.2.1 Level 1 EM and Level 2 ELE Efficiency

The traditional method of measuring trigger efficiency requires two triggers. Denote t_1 as the trigger of interest and t_2 as another trigger which has a lower E_T threshold. If t_2 is fully efficient for events passing t_1, then the ratio of the number of events passing t_1 to that passing t_2 as a function of offline object E_T defines the turn-on curve. Unfortunately we did not have a trigger with a lower threshold than EM (Level 1) or ELE (Level 2) in ELE_JET_HIGH. However, we follow the same concept to measure the efficiencies with a few assumptions. The assumptions are:

- the shape of the turn-on curve doesn't change over a few GeV;
- the offline object E_T scales with trigger threshold E_T, i.e., if $E_T^{t_1}(\text{threshold}) = q \cdot E_T^{t_2}(\text{threshold})$ then $E_T^{t_1}(\text{offline}) = q \cdot E_T^{t_2}(\text{offline})$.

The validity of these assumptions was discussed in [48].

Denote t_1 as the trigger of interest and t_2 as a hypothetical trigger. We require $E_T^{t_2}(\text{threshold}) = q \cdot E_T^{t_1}(\text{threshold})$ with $q > 1$ and also large enough that t_1 is fully efficient for events passing t_2. Using the traditional method a turn-on curve of t_2 can be obtained. From the first assumption, we can scale the turn-on curve down to the threshold of t_1, provided that the thresholds of t_1 and t_2 are only a few GeV apart. The magnitude of the scaling is based on the second assumption, i.e., we scale the offline E_T in the t_2 spectrum by a factor of $1/q$. The resulting curve as a function of the scaled offline E_T is the turn-on curve of t_1. We compared the traditional

method and our method on some applicable triggers and found that they agreed well with each other [48].

Figure 6.1 shows the EM (Level 1) turn-on curves. All the points were fitted to the turn-on function as defined in Equation 6.1. Two scales, $q = 2.0$ and $q = 2.5$ were used. The fit results are shown in Table 6.1. We averaged the fit parameters from two q scales to obtain the final parameters used in FMCØ. There are also two sets of parameter errors from the fits. For each parameter the larger fitted error of the two fits was assigned as the statistical error and one half of the differences between the two fits was assigned as the systematic error.

$$\varepsilon_{trig} = 0.5 \cdot p_3 \cdot [1 + erf(\frac{E_T - p_1}{\sqrt{2}p_2})] \tag{6.1}$$

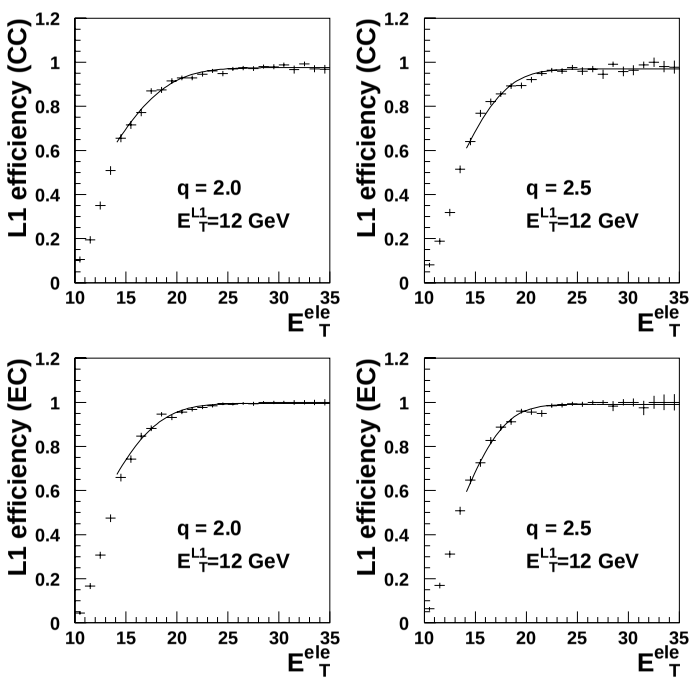

Figure 6.1 EM Level 1 turn-on curve as a function of offline electron E_T. The Level 1 threshold is 12 GeV. Two scales, $q = 2.0$ and $q = 2.5$ (see text), were used for both CC and EC electrons.

Table 6.1 Fit results of EM (Level 1) turn-on curves of ELE_JET_HIGH. Two scales, $q = 2.0$ and $q = 2.5$, were used for both CC and EC electrons. The fit parameters from the two scales were averaged and listed in the last column. The errors in the third and fourth columns come from the fit while the errors in the last column include statistical and systematic errors (see text).

Fiducial region	*param.*	$q = 2.0$	$q = 2.5$	averaged
CC Level 1	p_1	12.15 ± 0.34	12.84 ± 0.17	12.50 ± 0.48
	p_2	5.04 ± 0.38	3.94 ± 0.26	4.49 ± 0.67
	p_3	0.9759 ± 0.0035	0.9700 ± 0.0046	0.9729 ± 0.0055
	$\chi^2/ndof$	22.7/21	31.6/21	
EC Level 1	p_1	12.05 ± 0.52	13.24 ± 0.14	12.64 ± 0.79
	p_2	4.54 ± 0.47	3.53 ± 0.20	4.04 ± 0.69
	p_3	0.9956 ± 0.0028	0.9910 ± 0.0041	0.9933 ± 0.0047
	$\chi^2/ndof$	19.2/13	12.2/13	

For the ELE term at Level 2, we used $q = 1.3$ and $q = 1.4$ scales. Since the Level 2 electron E_T thresholds for ELE_JET_HIGH and ELE_JET_HIGHA are 15 and 17 GeV respectively, the parameters for the two thresholds were measured separately. The final efficiency was weighted by their luminosity fractions: $\varepsilon_{L2}^{elec} = 0.894 \cdot \varepsilon_{15}^{elec} + 0.106 \cdot \varepsilon_{17}^{elec}$. The plots and fit results are shown in Figure 6.2, 6.3 and Table 6.2, 6.3. The fit parameters and their errors were derived the same way as those for Level 1.

6.2.2 Level 1 JT and Level 2 JET Efficiency

The Level 1 JT and Level 2 JET efficiencies were measured in one step to obtain a combined efficiency. We used a data set with minimal JT/JET requirement and measured the probability that the events pass ELE_JET_HIGH. The data used were Run 1b data passing EM1_EISTRKCC_MS trigger. EM1_EISTRKCC_MS has only one jet-related trigger requirement: one Level 1 jet tower with E_T greater than 3 GeV, which is much looser than that of

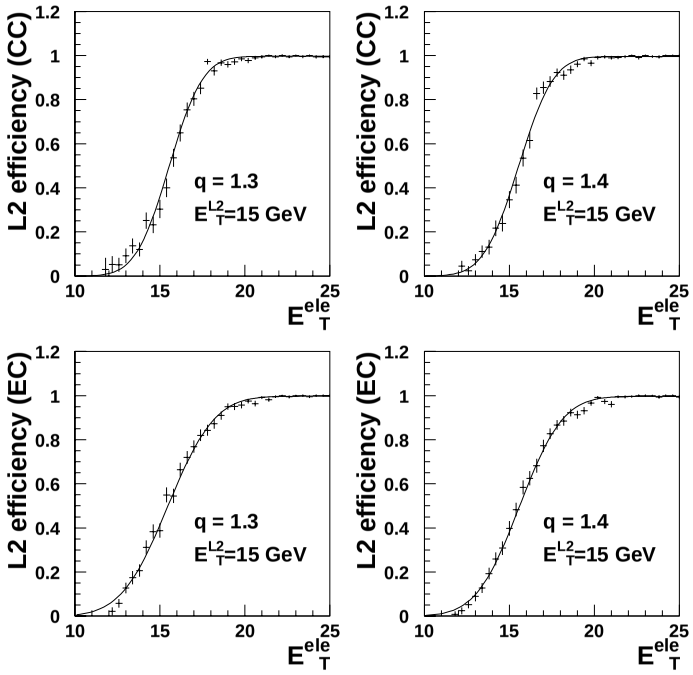

Figure 6.2 ELE Level 2 turn-on curve of ELE_JET_HIGH as a function of offline electron E_T. The Level 2 threshold is 15 GeV. Two scales, $q = 1.3$ and $q = 1.4$ (see text), were used for both CC and EC electrons.

ELE_JET_HIGH (see Table 4.1). Thus, the data were minimally biased for JT/JET trigger efficiency measurement. In fact we will see later that if there is an electron in the event it will almost always satisfy the jet requirement in ELE_JET_HIGH, making the bias negligible. We applied the same selection cuts to this sample as to our signal sample, except that we require $E_T^{elec} > 25$ GeV and $N_{jets} = 1$. The requirement on E_T^{elec} is to make sure that the EM and ELE term in ELE_JET_HIGH is fully efficient while the requirement on $Njets$ is to obtain the probability of turn-on curve per jet [2].

Figure 6.4 shows the JT/JET turn-on curves per jet of ELE_JET_HIGH for a jet in CC, ICR, and EC respectively. The points were fitted to Equation 6.1 and the fit results are shown in Table 6.4.

[2]We need a turn-on curve per jet because we need to construct the probability that a multijet event passes our signal trigger, a procedure which is described in the text later.

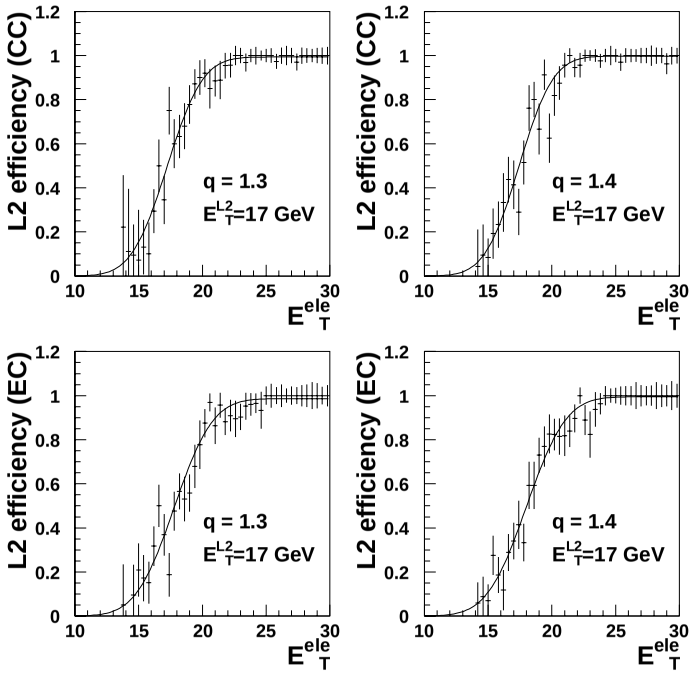

Figure 6.3 ELE Level 2 turn-on curve of ELE_JET_HIGHA as a function of offline electron E_T. The Level 2 threshold is 17 GeV. Two scales, $q = 1.3$ and $q = 1.4$ (see text), were used for both CC and EC electrons.

Electrons can fire the jet trigger because there is no maximum electromagnetic fraction cut on online jets. This effect needs to be taken into account when the overall trigger efficiency is calculated. The probability of an electron passing the JT/JET requirement of the ELE_JET_HIGH trigger is listed in Table 6.5 [48].

6.2.3 Level 2 $\not\!\!E_T$ Efficiency

According to [44] and [48] Level 2 $\not\!\!E_T$ is 100% efficient for offline cut $\not\!\!E_T > 25$ GeV.

Table 6.2 Fit results of ELE (Level 2) turn-on curves of ELE_JET_HIGH. The Level 2 threshold is 15 GeV. Two scales, $q = 1.3$ and $q = 1.4$, were used for both CC and EC electrons. The fit parameters from the two scales were averaged and listed in the last column. The error in the third and fourth columns come from the fit while the errors in the last column include statistical and systematic errors (see text).

Fiducial region	*param.*	$q = 1.3$	$q = 1.4$	averaged
CC Level 2	p_1	15.554 ± 0.055	15.543 ± 0.050	15.548 ± 0.055
	p_2	1.556 ± 0.063	1.621 ± 0.063	1.589 ± 0.071
	p_3	0.9966 ± 0.0018	0.9962 ± 0.0017	0.9964 ± 0.0019
	$\chi^2/ndof$	41.0/29	35.7/29	
EC Level 2	p_1	15.473 ± 0.052	15.599 ± 0.048	15.536 ± 0.081
	p_2	2.167 ± 0.062	2.013 ± 0.054	2.090 ± 0.099
	p_3	0.9975 ± 0.0018	0.9968 ± 0.0020	0.9972 ± 0.0020
	$\chi^2/ndof$	29.3/29	30.4/29	

6.2.4 Overall Trigger Efficiency

The overall trigger efficiency is calculated in Equation 6.2:

$$\begin{aligned} \varepsilon_{trig}^{total} &= \varepsilon_{trig}^{elec} \cdot \varepsilon_{trig}^{jet} \cdot \varepsilon_{trig}^{\not{E}_T} \\ &= \varepsilon_{L1}^{elec} \cdot (0.894 \cdot \varepsilon_{15}^{elec} + 0.106 \cdot \varepsilon_{17}^{elec}) \cdot \varepsilon_{trig}^{jet}. \end{aligned} \tag{6.2}$$

Because ε_{trig}^{jet} is a function of jet multiplicity, we describe this term in detail in this subsection.

We wrote ε_{trig}^{jet} in terms of p_i's, where p_0 is the probability shown in Table 6.5 and $p_{1,2,3,4,5}$ are the single jet trigger efficiency for the 5 leading jets as determined by the turn-on curve parameters in Table 6.4. Specifically,

Table 6.3 Fit results of ELE (Level 2) turn-on curves of ELE_JET_HIGHA. The Level 2 threshold is 17 GeV. Two scales, $q = 1.3$ and $q = 1.4$, were used for both CC and EC electrons. The fit parameters from the two scales were averaged and listed in the last column. The error in the third and fourth columns come from the fit while the errors in the last column include statistical and systematic errors (see text).

Fiducial region	*param.*	$q = 1.3$	$q = 1.4$	averaged
CC Level 2	p_1	17.24 ± 0.20	17.42 ± 0.18	17.33 ± 0.22
	p_2	2.21 ± 0.30	2.12 ± 0.24	2.16 ± 0.31
	p_3	0.9936 ± 0.0109	0.9972 ± 0.0096	0.9954 ± 0.0110
	$\chi^2/ndof$	13.1/29	19.5/29	
EC Level 2	p_1	17.80 ± 0.18	18.01 ± 0.18	17.90 ± 0.21
	p_2	2.39 ± 0.26	2.44 ± 0.26	2.42 ± 0.27
	p_3	0.9864 ± 0.0155	0.9949 ± 0.0155	0.9907 ± 0.0161
	$\chi^2/ndof$	26.8/29	16.4/29	

$$\varepsilon_{trig}^{jet} = 1 - \prod_{i=0}^{5}(1 - p_i), \tag{6.3}$$

where $\prod_{i=0}^{5}(1 - p_i)$ is the probability that none of the electron or jets fires the JT/JET term of the ELE_JET_HIGH trigger.

We compared the total trigger efficiency measured by the top group [44] using W+jet data events with that from FMCØ by putting VECBOS [53] W+jet events through FMCØ. Two sets of VECBOS samples were generated, one with QCD dynamic scale at $Q^2 = (\frac{1}{n}\sum_i E_T^{parton})^2$ (the "EJ" sample) and the other at $Q^2 = M_W^2$ (the "MW" sample). The partons from VECBOS output were put through HERWIG for fragmentation. The results are shown in Table 6.6. Our simulated trigger efficiencies agree very well with the data-based measurements at all four jet multiplicities. One may also note that the "EJ" sample agrees with data better than the "MW" sample. This is discussed in detail in Appendix B.

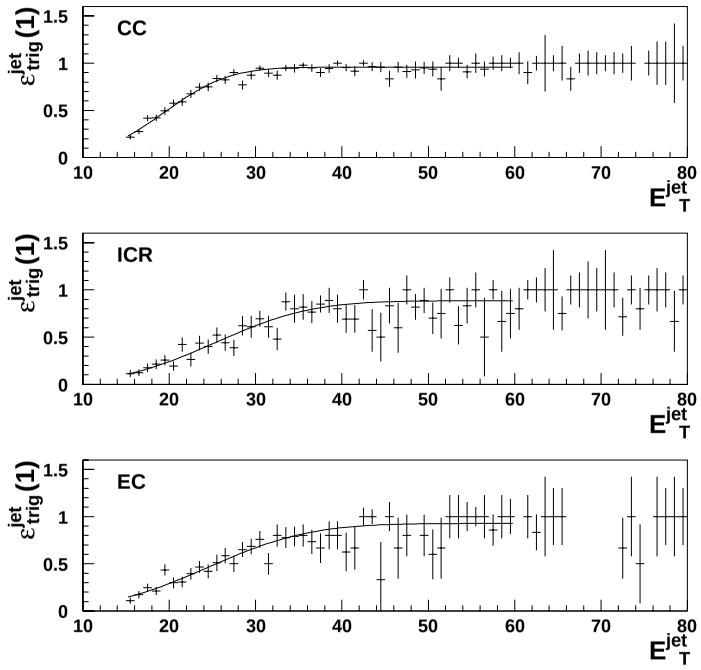

Figure 6.4 Combined Level 1 JT and Level 2 JET turn-on curve of ELE_JET_HIGH for a single jet. It is a function of offline jet E_T and jet fiducial region. The Level 1 jet tower E_T threshold is 5 GeV and the Level 2 jet E_T threshold is 10 GeV. The fits were performed in the region where the curves were drawn.

6.3 The Integrated FMCØ

With detector simulation and trigger/ID efficiencies in place, we set out to integrate FMCØ. The flow-chart of FMCØ is shown in Figure 6.5. Although its underlying physics generator is PYTHIA5.7 with the SPYTHIA extension [52], FMCØ is not restricted to one physics generator only. Any Monte-Carlo events in Run I ISAJET format can be put through FMCØ. Events first go through the D0pjet to form jets. Then the electrons, jets, muons, and $\not\!\!E_T$ in the events are smeared in QSIM. Then kinematic cuts, e.g., our offline signal cuts were applied to the smeared objects. Each passed event is then weighted with trigger and ID efficiencies. The outputs of FMCØ are a kinematic ntuple which contains the kinematics (E_T, η, ϕ, etc.) of every object of the passed events and a run summary ntuple which contains the total acceptance of the physics

Table 6.4 Fit results of the JT/JET turn-on curve of ELE_JET_HIGH for a single jet. The errors are from the fit.

param	CC	ICR	EC
p_1	19.40 ± 0.21	25.34 ± 0.82	24.50 ± 0.83
p_2	5.92 ± 0.37	8.80 ± 0.94	9.33 ± 0.99
p_3	0.9568 ± 0.0094	0.8846 ± 0.0362	0.9275 ± 0.0402
$\chi^2/ndof$	33.9/44	36.7/44	34.0/43

Table 6.5 Probability of an online electron to pass the JT/JET requirement of the ELE_JET_HIGH trigger.

$\lvert\eta_d\rvert$	$0.0 - 1.2$	$1.5 - 2.0$
p_0	0.994 ± 0.004	0.998 ± 0.008

process simulated. The acceptance A is calculated in Equation 6.4:

$$A = \frac{1}{N_{gen}} \sum_{i}^{N_{passed}} \varepsilon_{trig}^{total} \cdot \varepsilon_{id}^{e,j}, \tag{6.4}$$

where N_{gen} is the number of generated events and N_{passed} is the number of events that passed the offline kinematic cuts. The error on acceptance δ_A is calculated in Equation 6.5:

$$\delta_A = \frac{1}{N_{gen}} \sum_{i}^{N_{passed}} \delta_{\varepsilon}, \tag{6.5}$$

where δ_ε comes from the usual error propagation from the errors on $\varepsilon_{trig}^{total}$ and $\varepsilon_{id}^{e,j}$. The equation takes into account the fact that the errors event by event are 100% correlated.

We made several checks on the acceptances of FMCØ and GEANT. In the first check we compared the kinematic acceptance of $WW+ \geq 2$ jet events. Both samples were generated by PYTHIA. The GEANT sample was taken from the single top analysis [43] in which one W

Table 6.6 Comparison of the ELE_JET_HIGH trigger efficiency. The second column lists the efficiencies the top group measured using $W+$ jet data events [44]; the third and fourth columns list the simulated efficiencies by putting the VECBOS $W+$ jet sample through FMCØ. "EJ" and "MW" refer to the two QCD dynamic scales at which the VECBOS samples were generated (see text).

N_{jet}	top group	VECBOS (EJ)	VECBOS (MW)
≥ 1	0.589 ± 0.019	0.579 ± 0.022	0.623 ± 0.022
≥ 2	0.826 ± 0.027	0.833 ± 0.020	0.862 ± 0.019
≥ 3	0.928 ± 0.031	0.925 ± 0.016	0.940 ± 0.014
≥ 4	0.944 ± 0.037	0.957 ± 0.012	0.963 ± 0.012

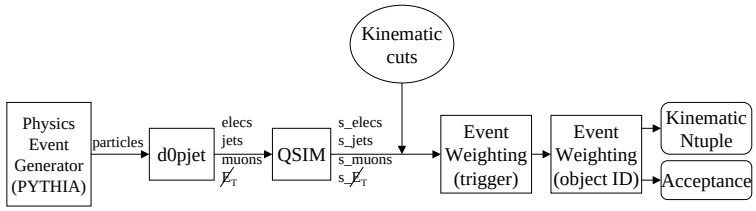

Figure 6.5 Flow-chart of FMCØ. Prefix "s" refers to smeared objects.

was required to decay into an electron or a τ and the other W was required to decay to jets. The FMCØ sample didn't impose any restriction on the W decay. We applied our final signal kinematic selection cuts to both samples. We found 234 CC and 47 EC events (CC/EC are in terms of the electron fiducial region) out of 50,000 GEANT events. After taking into account the PELC efficiency of Monte Carlo, which are 0.9475 ± 0.0064 in CC and 0.9069 ± 0.0157 in EC respectively [44], we obtain the kinematic acceptance of the GEANT sample:

$$A^{kin}_{GEANT} = 2 \cdot \frac{2}{9} \cdot \frac{234/0.9475 + 47/0.9069}{50000}$$
$$= 0.00266 \pm 0.00015, \tag{6.6}$$

where the factor 2/9 comes from the branching ratio of W to electron and τ. The error includes statistical error as well as the error on the MC electron ID. The kinematic acceptance of FMCØ is 0.00259 ± 0.00003. The error is statistical only. The two kinematic acceptances agree very well with each other.

The second check was to compare the kinematic acceptances of $t\bar{t}$ events. The kinematics of $t\bar{t}$ events is very close to that of mSUGRA signal because both require production of a pair of heavy objects in the hard scattering. Thus, the kinematics of $t\bar{t}$ and signal being much harder than that of QCD, $W+ \geq 4$ jet, and $WW+ \geq 2$ jet events. PYTHIA and HERWIG $t\bar{t}$ events with $m_{top} = 170$ GeV/c^2 were generated for FMCØ. The GEANT sample was generated by HERWIG with the same top mass and with the requirement that at least one W decayed to a lepton. (This sample again came from the single top analysis.) It has 81141 events. The kinematic acceptance of GEANT sample is then:

$$A^{kin}_{GEANT} = \frac{5}{9} \cdot \frac{N_{cc}/0.9475 + N_{ec}/0.9069}{81141}, \tag{6.7}$$

where N_{cc} and N_{ec} are the number of MC events with the single electron in CC and EC respectively. The kinematic acceptances are shown in Table 6.7. We found that all three samples agreed well with each other. We assigned the difference in acceptance between FMCØ (HERWIG) and FMCØ (PYTHIA) as one of the systematic errors on the acceptance. Difference between GEANT(HERWIG) and FMCØ (HERWIG) is not included in the systematic error because the parameter tuning in D0pjet was done on PYTHIA files only and that its impact is small as can be seen in the ≥ 4 jet case in particular.

Finally we made a check on the overall acceptance. The benchmark we compared FMCØ with is the VECBOS (EJ) $W+ \geq 2$ jet cross section measured in the analysis of triple-gauge

Table 6.7 Comparison of kinematic acceptance of GEANT (HERWIG as generator) FMCØ (HERWIG and PYTHIA as generators) events as a function of inclusive jet multiplicity (N_{jet}). All three samples are $t\bar{t}$ events with m_{top} = 170 GeV/c^2. The errors of the acceptance of the GEANT $t\bar{t}$ sample include statistical error and the error on the MC electron ID efficiency. The errors on the FMCØ samples are statistical only.

N_{jet}	N_{cc}	N_{ec}	GEANT(HERWIG)	FMCØ (HERWIG)	FMCØ (PYTHIA)
≥ 1	13544	1320	0.1078 ± 0.0012	0.1008 ± 0.0005	0.0991 ± 0.0009
≥ 2	13170	1298	0.1050 ± 0.0010	0.0989 ± 0.0005	0.0970 ± 0.0009
≥ 3	10945	1122	0.0876 ± 0.0009	0.0858 ± 0.0005	0.0828 ± 0.0008
≥ 4	6465	665	0.0517 ± 0.0007	0.0559 ± 0.0004	0.0514 ± 0.0005

boson coupling in $e\nu jj$ channel [54]. In that analysis, the dominant QCD multijet and WW backgrounds were subtracted from $e + \not\!\!E_T + \geq 2$ jet data. The number of data events remaining was divided by the VECBOS acceptance to obtain the VECBOS cross section: 138.6 ± 14.3 pb. Note the $t\bar{t}$ background was ignored in that analysis.

We generated the VECBOS sample with the exact conditions as that in triple-gauge boson analysis. We then made our offline selection on our ELE_JET_HIGH(A) data (both Run 1b and Run 1c). The selections were exactly the same as that in our signal selection except that we only required two good jets. We observed 1661 events. The measured number of QCD multijet background events was 243.1 ± 42.4 (see Chapter 7 for detail). From FMCØ, the expected number of WW events (which result in $e + \not\!\!E_T + \geq 2$ jet final state) is 31.2 ± 2.5. Thus the expected number of $W + \geq 2$ jet events is 1363.5 ± 42.1. The acceptance of the VECBOS sample is 0.123 ± 0.011 (the error includes statistical error and the error due to trigger and ID efficiencies). The VECBOS cross section is then: $1363.5/(0.123 \times 92.7) = 119.4 \pm 12.3$ pb (ignoring $t\bar{t}$ contribution). Thus, the VECBOS cross section measured based on FMCØ agrees with that measured based on GEANT.

6.4 Summary

We use FMCØ as the major analysis tool to estimate the acceptances of signal, $t\bar{t}$, and WW processes. Events with very different kinematic properties (W+jets, WW, and $t\bar{t}$) were put through FMCØ and GEANT to compare their acceptances. We found they agreed well with each other.

7 BACKGROUNDS

7.1 QCD Multijet Background

From our ELE_JET_HIGH(A) data we obtained two sub-samples. Sample 1 simply required that all our offline cuts were satisfied except for the $\not\!\!E_T$ cut. We call it the electron sample. Sample 2 required that the EM object had to pass an "anti-electron" cut while all other cuts were the same as those in sample 1. The "anti-electron" cut preferentially selects those events in which a jet has faked an electron. Since there are virtually no real electrons in this sample we call it the "fake sample". Jet energy fluctuation in the low $\not\!\!E_T$ region ($\not\!\!E_T < 20$ GeV) of the electron sample is the cause of the $\not\!\!E_T$. The events are mostly of QCD multijet origin because the contributions from $W+$ jets, $t\bar{t}$, and signal are all negligible there. Since the fake sample models the QCD multijet events in all $\not\!\!E_T$ regions, we can use the $\not\!\!E_T$ spectra of both samples to estimate the number of QCD multijet background events (N_{QCD}) in the electron sample. We first normalize the $\not\!\!E_T$ spectrum of the fake sample to that of the electron sample in the low $\not\!\!E_T$ region and then estimate N_{QCD} by multiplying the number of events in the signal region ($\not\!\!E_T > 25$ GeV) in the fake sample by the normalization factor [55].

The matched $\not\!\!E_T$ spectra for both samples are shown in Figure 7.1 and 7.2. The "anti-electron" cuts are $\chi^2_{hm} > 100$ and $S_{match} > 10$ for the $\geq 1/2/3$ jet samples and $\chi^2_{hm} > 150$ for the ≥ 4 jet sample. We loosened the cut for the ≥ 4 jet sample because we needed to obtain adequate statistics for the fake sample to do the normalization. The nominal normalization of $\not\!\!E_T$ was performed between $0 \leq \not\!\!E_T \leq 14$ GeV. The results are shown in Table 7.1.

The errors in Table 7.1 are explained below:

- σ_1: the statistical error due to the normalization of the two samples and due to the statistics of the two samples themselves.

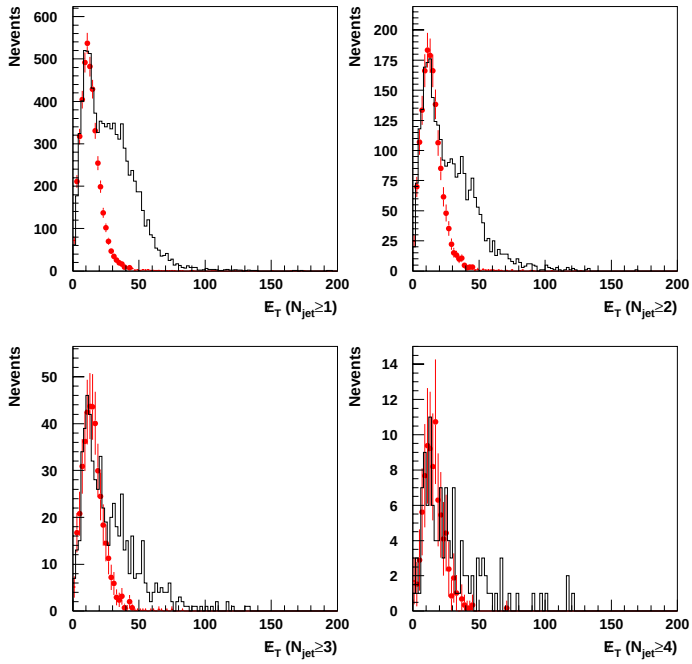

Figure 7.1 Calculating the QCD multijet background in the electron sample by normalizing $\not\!\!E_T$ spectrum of fake sample to that of the electron sample in the low $\not\!\!E_T$ region. The fake sample is plotted in circles and the electron sample is plotted in histogram. The errors are statistical only. The plots are for CC electrons.

- σ_2: the systematic error due to the choice of different normalization regions. The two regions: $0 \leq \not\!\!E_T \leq 12$ GeV and $0 \leq \not\!\!E_T \leq 16$ GeV were also used to calculate the QCD multijet background. Each result was compared with the nominal. The larger difference of the two was assigned as σ_2.

- σ_3: the systematic error due to trigger and ID efficiencies. The fake event is subject to the same trigger and ID cut as the electron event. We estimated this error by putting VECBOS (EJ) + HERWIG $W+$ jet events through FMCØ because they have similar kinematics.

- σ_4: the systematic error due to a different "anti-electron" definition. We recalculated the QCD multijet background by requiring the fake electron to satisfy $\chi^2_{hm} > 200$ and

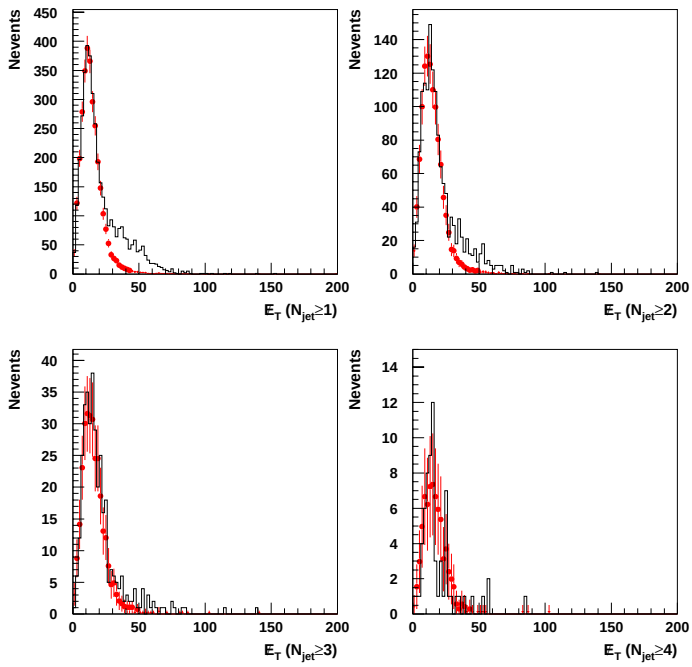

Figure 7.2 Calculating the QCD multijet background in the electron sample by normalizing $\not\!\!E_T$ spectrum of fake sample to that of the electron sample in the low $\not\!\!E_T$ region. The fake sample is plotted in circles and the electron sample is plotted in histogram. The errors are statistical only. The plots are for EC electrons.

$S_{match} > 10$. The difference between this result and the nominal was assigned as σ_4.

7.2 $t\bar{t}$ Background

The number of $t\bar{t}$ background events, $N_{t\bar{t}}$, was calculated by FMCØ. The $t\bar{t}$ events were generated with $m_{top} = 175$ GeV/c^2. The production cross section of $t\bar{t}$ is 5.89 ± 1.66 pb, as measured by DØ [56]. The error, $\sigma_{xsec} = 1.66$ pb, includes uncertainties from the trigger and ID efficiencies, jet energy scale, event generator dependence (HERWIG vs. ISAJET) and data statistics. Because we used new trigger and ID efficiencies and also because we used PYTHIA as our underlying physics generator, to estimate the total error of $N_{t\bar{t}}$, we added in quadrature the errors due to the trigger and ID efficiencies from FMCØ (σ_ε) and the difference in acceptance

Table 7.1 Estimated number of QCD multijet background events, N_{QCD}, as a function of inclusive jet multiplicity, N_{jet} in the ELE_JET_HIGH sample. CC and EC results are combined. σ_1, σ_2, σ_3, and σ_4 are errors from four different sources (see text).

N_{jet}	N_{QCD}	σ_1	σ_2	σ_3	σ_4
≥ 1	568.2 ± 61.1	12.7	4.8	58.3	12.0
≥ 2	263.7 ± 42.4	9.4	5.8	40.0	8.6
≥ 3	82.6 ± 15.3	5.8	2.3	13.5	4.0
≥ 4	19.1 ± 4.7	2.6	1.5	3.1	1.8

between PYTHIA and HERWIG (σ_{MC}) to σ_{xsec}. This is a conservative approach. The error due to parton distribution function (PDF) can be ignored. The result is shown in Table 7.2 for ≥ 3 and ≥ 4 jet events.

Table 7.2 Estimated number of the $t\bar{t}$ background events, $N_{t\bar{t}}$, in ≥ 3 and ≥ 4 jet data samples (ELE_JET_HIGH(A)). The errors (in the form of relative error) come from cross section (σ_{xsec}), trigger/ID efficiency (σ_ε), difference in MC (σ_{MC}) and luminosity (σ_{lum}).

N_{jet}	$N_{t\bar{t}}$	σ_{xsec}	σ_ε	σ_{MC}	σ_{lum}
≥ 3	28.6 ± 8.5	28.2%	6.9%	5.1%	4.4%
≥ 4	17.4 ± 5.5	28.2%	7.3%	11.6%	4.4%

7.3 WW Background

FMCØ was also used to calculate the number of WW background events, N_{WW}. The theoretical WW cross section was calculated in [57]. The calculation used an obsolete parton distribution function. After a correction to the more modern parton distribution function (CTEQ3M) the cross section is 10.4 ± 0.23 pb [43]. The errors of N_{WW} were calculated the same way as those on $N_{t\bar{t}}$. The only extra error term comes from the jet energy scale. We

measured that by calculating from a GEANT WW sample the change of acceptance due to change of E_T^j by one sigma of its resolution:

$$E_T^j(new) = (1 \pm s) \cdot E_T^j(nominal) \pm c, \tag{7.1}$$

where $s = 2.5\%$ and $c = 0.5$ GeV. Due to the uncertainty introduced during DØ data fixing (see Chapter 5), we raised s to 3.5% for jets within $0.8 \leq |\eta_d^j| \leq 1.4$. The result is shown in Table 7.3 for ≥ 3 and ≥ 4 jet events.

Table 7.3 Estimated number of WW background events, N_{WW}, in ≥ 3 and ≥ 4 jet data samples (ELE_JET_HIGH(A)). The errors (in the form of relative error) come from cross section (σ_{xsec}), trigger/ID efficiency (σ_ε), difference in MC (σ_{MC}), jet energy scale (σ_{escale}) and luminosity (σ_{lum}).

N_{jet}	N_{WW}	σ_{xsec}	σ_ε	σ_{MC}	σ_{escale}	σ_{lum}
≥ 3	7.7 ± 1.2	2.2%	8.1%	5.1%	11.0%	4.4%
≥ 4	1.42 ± 0.33	2.2%	8.4%	11.6%	17.6%	4.4%

7.4 $W+$ jets Background

To a good approximation [53] each extra jet in $W+$ jet events is a result of an extra interaction vertex of strength α_s. We expect that the number of $W+$ jets events scales to the power of N_{jet} [53]. The scaling law has been proven valid by the top cross section analysis [44]. In this analysis we first measured the scaling factor α and then estimated the number of $W+ \geq 3$ jet events in our ELE_JET_HIGH(A) data, N_3. The expected number of $W+ \geq 4$ jet events, N_4^W in our ELE_JET_HIGH(A) data is then:

$$N_4^W = N_3^W \cdot \alpha \cdot \frac{\varepsilon_{trig}^{W4}}{\varepsilon_{trig}^{W3}}, \tag{7.2}$$

where ε_{trig}^{W3} and ε_{trig}^{W4} are the trigger efficiencies of $W+ \geq 3$ jet and $W+ \geq 4$ jet events, respectively. They are listed in Table 6.6.

7.4.1 Measuring the Scaling Factor α

To measure α, we first calculated the number of the $W+ \geq n$ jet events, $\overline{N}_n^W$, from a sample with no bias on jet multiplicity. $\overline{N}_n^W$ was used to distinguish it from N_n^W which is the number of $W+ \geq n$ jet events in the ELE_JET_HIGH(A) data. We then fit $\overline{N}_n^W$ to a power law (Equation 7.3) to extract α:

$$\overline{N}_n^W = \overline{N}_1^W \cdot \alpha^{n-1}. \tag{7.3}$$

We used Run 1b EM1_EISTRKCC_MS data to measure α since there is virtually no trigger bias on N_{jet}. The integrated luminosity after main ring veto is 80.4 ± 3.5 pb^{-1}. Since we are interested in the number of $W+ \geq n$ jet events, the $W+ \geq n$ jet events become our signal and QCD multijet, $t\bar{t}$, WW, and possible SUSY events become our backgrounds. We applied the offline cuts as described in Chapter 4. We required different number of good jets for different inclusive jet multiplicities. We also required $E_T^{ele} > 25$ GeV to avoid Level 1 trigger inefficiency [58].

The concept of estimating number of $W+ \geq n$ jet events is the same as that used for the QCD multijet background estimation. We first find a kinematic region in which $W+ \geq n$ jet events dominate and the contribution of SUSY signal can be ignored. We calculate from MC the expected fraction (f) of $W+ \geq n$ jet events in that region. We then normalize in that region the number of $W+ \geq n$ jet MC events (N_{MC}) to the number of data events (N_{data}) with all major SM background subtracted. The total number of $W+ \geq n$ jet events is then: $\overline{N}_n^W = N_{data}/f$. To find such a kinematic region we use Neural Network (NN) [1].

The NN training and testing samples for $t\bar{t}$, WW, and mSUGRA events were generated using PYTHIA. The $W+ \geq n$ jet samples were generated using VECBOS(parton)+HERWIG(fragmentation). These samples were put through FMCØ. For QCD multijet events, the training samples were

[1] In this analysis, we used a Neural Network package called MLPFIT [59].

obtained from the FAKE_ELEC data stream [2]. We required the same fake electron criteria as that we used to calculate the number of QCD multijet background events: $\chi^2_{hm} > 100$ and $S_{match} > 10$ for the $\geq 1/2/3$ jet samples and $\chi^2_{hm} > 150$ for the ≥ 4 jet sample. Because of the limited statistics in FAKE_ELEC data the testing sample was obtained from the J3MON data stream. We required the events to have at least n good jets (for n inclusive jet multiplicity) and one more jet with $E_T > 25$ GeV and satisfying the electron fiducial cut. We also required that the event had $\not\!\!E_T > 25$ GeV. Any jet combination satisfying these requirements was written out as a testing event. The J3MON data were not used for any direct background calculation. Their sole purpose was to guard against over-training in NN.

We calculated the QCD multijet (using the method described in section 7.1), $t\bar{t}$ (see section 7.2), WW (see section 7.3), and mSUGRA backgrounds respectively for each inclusive jet multiplicity (1 to 4). We generated the mSUGRA sample with $M_0 = 170$ GeV/c^2, $M_{1/2} = 58$ GeV/c^2 and $\tan(\beta) = 3.0$. This point was chosen because it predicted the largest number of events in our data for $\tan(\beta) = 3.0$ and it was right on the exclusion contour from the DØ dilepton analysis [48]. The error on the number of expected SUSY events included the error on trigger and ID efficiencies (estimated by FMCØ [3]), cross section (10% [4]), difference in MC (estimated by FMCØ on $t\bar{t}$ events) and jet energy scale (negligible for $N_{jet} \geq 1$ and $N_{jet} \geq 2$ events, 1.8% for $N_{jet} \geq 3$ events and 5.3% for $N_{jet} \geq 4$ events [5]).

In this analysis, all NN have the structure of X-2X-1 where X is the number of input nodes, i.e., number of variables used for training and 2X is the number of nodes in the hidden layer. We always used 1 output node with an output range approximately between (0,1). Signals were expected to have NN output near 1 and background near 0. The variables used to distinguish

[2] A data stream is a set of data which pass a set of similar triggers.

[3] We modified FMCØ to incorporate the simulation of EM1_EISTRKCC_MS Level 2 trigger. The EM part of the Level 2 trigger parameters were obtained from the CMS package [60, 61] used by QCDWZ group. The MS part is 100% efficient. All the jet trigger simulations were discarded.

[4] The error on the cross section of mSUGRA events is dominated by PDF because high x incoming gluons are involved in the mSUGRA processes. Our nominal PDF is CTEQ4M [62]. In order to estimate the magnitude of systematic error due to PDF, mSUGRA events were generated in a broad $M_0 - M_{1/2}$ space. Points of which gg subprocess dominates were identified. We then generated events at these points using a different PDF (CTEQ3M). The difference in acceptance between the CTEQ3M and CTEQ4M samples is assigned as the systematic error on mSUGRA cross section. Our error estimation is conservative.

[5] These numbers are derived from a GEANT $t\bar{t}$ sample following the method described in section 7.3. Since SUSY events are usually harder than $t\bar{t}$ events our estimate is conservative.

$W+ \geq n$ jet events from the backgrounds are:

- $\not\!\!E_T$
- E_T^e
- $H_T = \sum E_T^{jet}$ for all jets with $E_T^{jet} > 15$ GeV
- $\Delta\phi_{e,\not\!\!E_T}$
- $M_T = \sqrt{2E_T^e \not\!\!E_T (1 - cos(\Delta\phi_{e,\not\!\!E_T}))}$
- $\Delta\phi_{j_1,\not\!\!E_T}$ (not used for ≥ 4 jet events)
- $\Delta\phi_{j_2,\not\!\!E_T}$ (used for ≥ 2 jet and ≥ 3 jet events)
- $\mathcal{A}$ - Aplanarity [63] (not used for ≥ 1 jet events). $\mathcal{A}$ is defined in terms of the normalized momentum tensor of the W boson and the jets with $E_T^j > 15$ GeV:

$$M_{ab} = \frac{\sum_i p_{ia} p_{ib}}{\sum_i p_i^2}, \tag{7.4}$$

  where $\vec{p_i}$ is the three momentum of the ith object in the laboratory frame, and a, b run over x, y, and z. Denote Q_1, Q_2, and Q_3 as the 3 eigenvalues of M_{ab} in increasing order. Then $\mathcal{A} = 1.5 \times Q_1$. The p_z of the W boson was calculated by imposing the requirement that the invariant mass of the electron and the neutrino (assumed to be the source of $\not\!\!E_T$) to be equal to the W mass. This requirement results in a quadratic equation. The smaller p_z was chosen [6]. In case there is no real solution, $\not\!\!E_T$ was increased until a real solution was found.

- $r_H = H_{T2}/H_Z$, where $H_{T2} = H_T - E_{T,1}^j$ and $H_Z = \sum_i |p_z|$ where i runs over all leptons, jets and neutrino in the event [64] (only used for ≥ 4 jet events).
- $cos(\theta_e^*)$, where θ_e^* is the polar angle of the electron in the W rest frame. The W four momentum was obtained by fitting the event to $t\bar{t}$ event. The detail of the fit is described in Appendix C. (only used for ≥ 4 jet events)

[6] This is because the probability of a small p_z is higher than that of a large p_z.

- $cos(\theta^*_{eb})$, where θ^*_{eb} is the angle between the electron and the b jet from the same top (or antitop) in the W rest frame [65] Again, fit to $t\bar{t}$ event was performed to identify the right b jet. (only used for ≥ 4 jet events)

Figure 7.3 shows the NN output on $W+ \geq n$ jet and background events. The number of signal and background events are the same in each of plots in the figure. Figure 7.4 shows the normalization of MC to data. The data were plotted as histograms and the normalized signal + expected background (mSUGRA excluded) were plotted as points. The errors on the points include statistical error and the error due to trigger and ID efficiencies. From the bottom up the backgrounds are stacked up in the order of QCD multijet, $t\bar{t}$ and WW, and $mSUGRA$. VECBOS (EJ) samples were used as signal samples for all jet multiplicities expect for $N_{jet} \geq 1$. We found that for $N_{jet} \geq 1$, PYTHIA modeled the data the best [7]. Normalization was performed between [0.5,1.0] in NN output and the results are listed in Table 7.4. The statistical error arises from the number of data events available for normalization. The systematic errors are estimated by using a different normalization region: NN Output between [0.6,1.0] and by using the VECBOS (MW) samples in the training and normalization.

We fit $\overline{N}^W_n$ to Equation 7.3. The fit is shown in Figure 7.5. It shows that the data obey the scaling law. From the fit we obtained $\alpha = 0.172 \pm 0.0066$.

7.4.2 Estimating the Number of $W+ \geq 3$ jet Events, N^W_3

The method of estimating the number of $W+ \geq 3$ jet events in ELE_JET_HIGH(A) is exactly the same as that described in the previous subsection. The results are shown in Figure 7.6 and Table 7.5.

7.4.3 Calculating the Number of $W+ \geq 4$ jet Events, N^W_4

The trigger efficiencies of $W+ \geq 3$ jet and $W+ \geq 4$ jet events are calculated using FMCØ on VECBOS (EJ) events which were fragmented by HERWIG. Take from Table 6.6, they are $\varepsilon^{W3}_{trig} = 0.925 \pm 0.016$ and $\varepsilon^{W4}_{trig} = 0.957 \pm 0.012$.

[7] This is because for VECBOS $W+ \geq 1$ jet event the p^W_T has to be equal to E^{parton}_T, which was set to 10 GeV. This threshold in MC generation biases the kinematics.

Table 7.4 Estimated number of $W+ \geq n$ jet events, $\overline{N}_n^W$ as a function of inclusive jet multiplicity in the EM1_EISTRKCC_MS data. They were obtained by normalizing MC to data in the NN output region where $W+ \geq n$ jet events dominate (see text).

N_{jet}	≥ 1	≥ 2	≥ 3	≥ 4
N_{obs}	8191	1691	353	64
N_{QCD}	825.7 ± 95.3	290.9 ± 47.6	74.9 ± 15.3	16.6 ± 7.0
$N_{t\bar{t}}$	26.7 ± 7.9	27.0 ± 7.9	22.6 ± 6.7	13.9 ± 4.4
N_{WW}	33.7 ± 3.3	23.6 ± 2.3	6.19 ± 0.95	1.12 ± 0.25
N_{SUSY}	28.3 ± 3.7	25.0 ± 3.1	19.7 ± 2.7	12.6 ± 2.1
$\overline{N}_n^W$	7210.3 ± 131.2	1283.1 ± 79.2	230.1 ± 27.1	27.4 ± 7.4

Before calculating the number $W+ \geq 4$ jet events using Equation 7.2 we examine the error of $\varepsilon_{trig}^{W4}/\varepsilon_{trig}^{W3}$. The errors of ε_{trig}^{W3} and ε_{trig}^{W3} are highly correlated due to the fact that both samples passed the same trigger.

We again used the VECBOS (EJ) $W+ \geq 3$ and $W+ \geq 4$ jet events which were fragmented by HERWIG to estimate the error of the ratio. We first calculated for both samples the average jet E_T for the 5 leading jets in different fiducial regions. We then varied the trigger parameters according to their resolutions and plotted the distribution of $\varepsilon_{trig}^{W4}/\varepsilon_{trig}^{W3}$. The RMS of the distribution is assigned as the error. We obtained $\varepsilon_{trig}^{W4}/\varepsilon_{trig}^{W3} = 1.035 \pm 0.001$.

Finally from Equation 7.2, we obtained the number of $W+ \geq 4$ jet events:

$$N_4^W = 241.8 \times 0.172 \times 1.035 = 43.0 \pm 7.6. \tag{7.5}$$

The error on N_4^W includes errors due to different PDF: 1.4%, MC difference: 11.6% , the uncertainty of the scaling method itself: 10.3% [44], and errors on N_3^W, α, and $\varepsilon_{trig}^{W4}/\varepsilon_{trig}^{W3}$. The calculated N_4^W differs from the result obtained by using direct MC/Data normalization on $W+ \geq 4$ jet events. (see Table 7.5) The difference is 1.4σ with $\sigma = \sqrt{7.6^2 + 7.3^2} = 10.5$, and is acceptable.

Table 7.5 Estimated of the number of $W+ \geq 3$ and $W+ \geq 4$ jet events as a function of jet multiplicity in ELE_JET_HIGH(A) data. They were obtained by normalizing MC to data in the NN output region where $W+ \geq n$ jet events dominate (see text).

N_{jet}	≥ 3	≥ 4
N_{obs}	362	72
N_{QCD}	82.6 ± 15.3	19.1 ± 4.7
$N_{t\bar{t}}$	28.6 ± 8.5	17.4 ± 5.5
N_{WW}	7.7 ± 1.2	1.42 ± 0.33
N_{SUSY}	29.0 ± 4.0	18.5 ± 3.2
N_n^W	241.8 ± 18.0	28.2 ± 7.3

7.5 Summary

The number of background events of different sources are summarized below:

$W + 4$ jets:	43.0	$\pm$	7.6
QCD:	19.1	$\pm$	4.7
$t\bar{t}$:	17.4	$\pm$	5.5
WW:	1.42	$\pm$	0.33
Total:	80.8	$\pm$	10.5

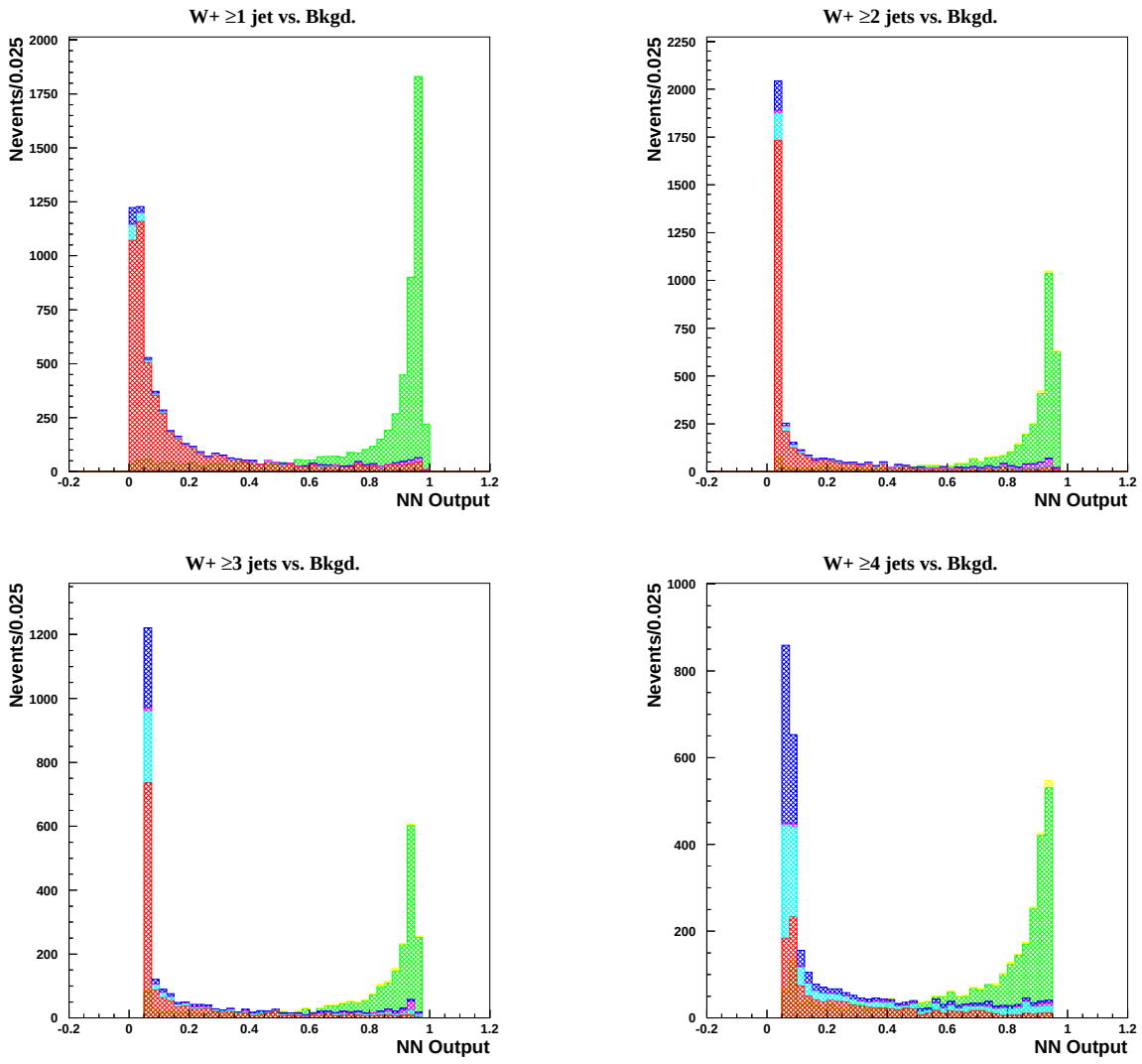

Figure 7.3 Expected NN output for the $W+ \geq 1$ jet (top left), $W+ \geq 2$ jet (top right), $W+ \geq 3$ jet (bottom left), $W+ \geq 4$ jet (bottom right) events, and the corresponding background events.

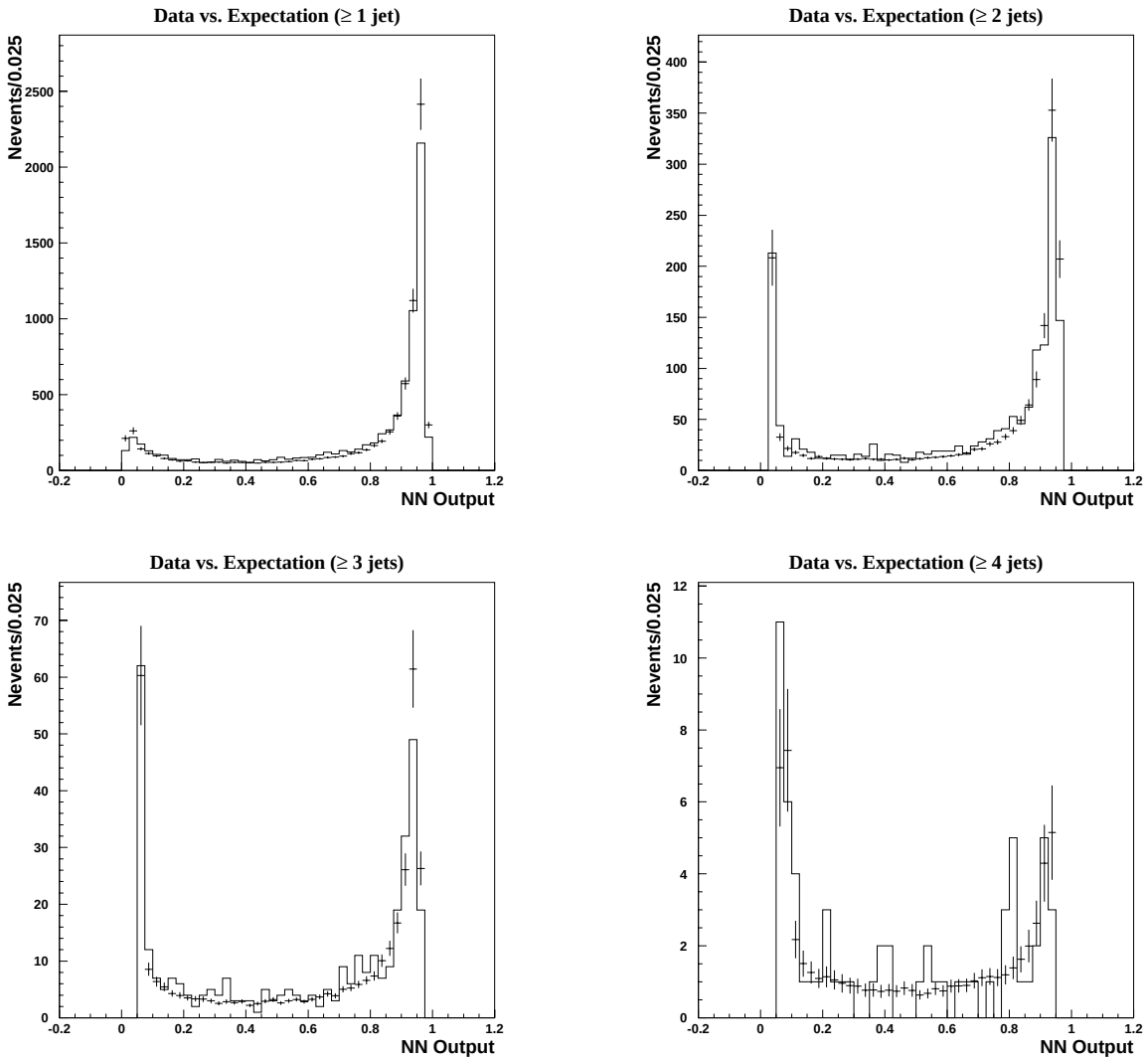

Figure 7.4 NN output for the expected (points) and the real (histogram) data. In the top left plot at least 1 jet was required; in the top right plot at least 2 jets were required; in the bottom left plot at least 3 jes were required and in the bottom right plot at least 4 jets were required. The data events were required to pass the EM1_EISTRKCC_MS trigger.

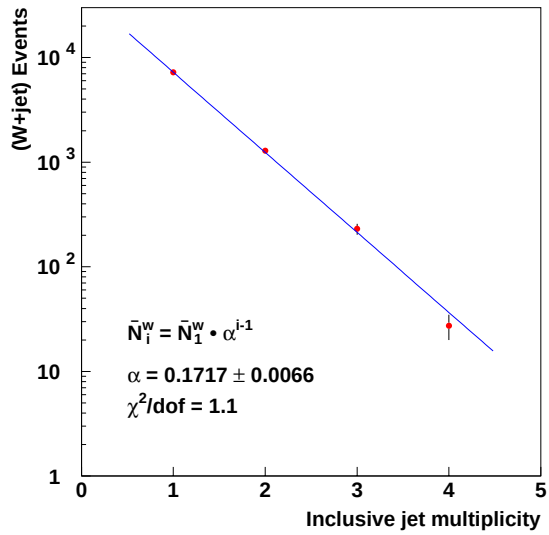

Figure 7.5 Fitting $W+ \geq n$ jet events to a power law as shown in Equation 7.3. The fit shows that the power law is well observed in the data.

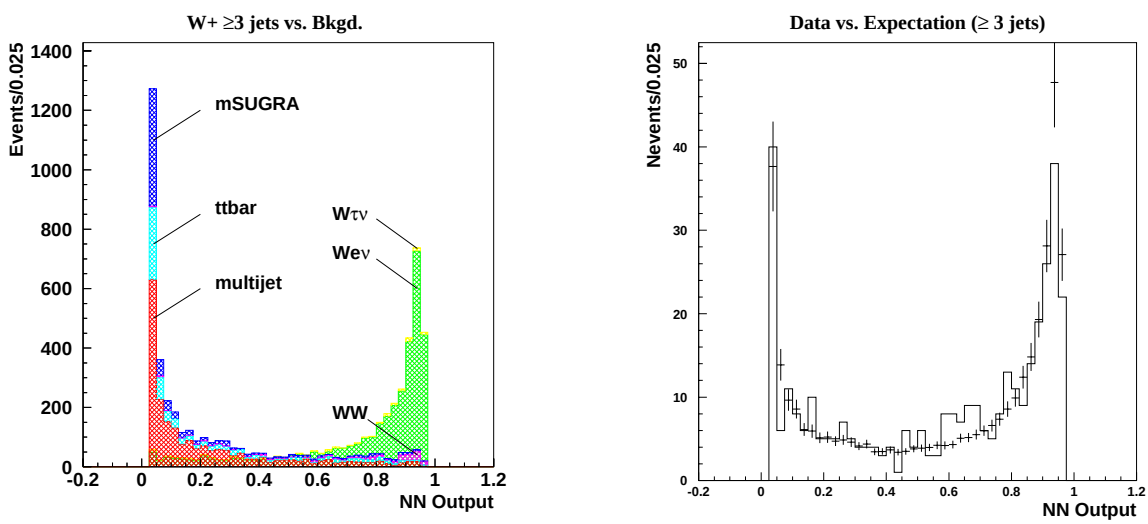

Figure 7.6 Expected NN output for $W+ \geq 3$ jet and its corresponding background events (left plot) and NN output for the expected (points) and the real (histogram) data (right plot). The MC (data) events were simulated (required) to pass the ELE_JET_HIGH(A) trigger.

8 SIGNAL ANALYSIS

8.1 Neural Network Analysis

Because of the tiny acceptance for a typical mSUGRA signal, we used Neural Network to optimally find a kinematic region in which signal to background sensitivity is the highest. We then look in that region for a possible signal. We used the following variables [1] in the Neural Network:

- $\not\!\!E_T$ – Missing transverse energy of the event. For the signal, it comes from two LSP's and at least one neutrino. For the $t\bar{t}$, $W+$ jet, and WW backgrounds, it comes from the neutrino. For the QCD multijet background, it comes from fluctuation in jet energy measurement. Generally, the signal has larger $\not\!\!E_T$ than backgrounds.

- E_T^{ele} – Electron in the signal comes from a virtual W decay. Its spectrum is softer than that of $t\bar{t}$ and $W+$ jet backgrounds.

- H_T – A pair of heavy mSUGRA particles are produced at hard scattering and most of the transverse energy is carried by jets. The signal H_T is thus harder than that of backgrounds.

- E_T^{j3} – Jet 3 from $W+$ jet, WW and QCD multijet events most likely originates from bremsstrahlung. For $t\bar{t}$ and mSUGRA events it comes more likely from W decay. Thus, $t\bar{t}$ and mSUGRA signals have harder E_T^{j3} spectrum.

- M_T – For $t\bar{t}$, $W+$ jet, and WW events, M_T peaks near $M_W = 80$ GeV. This is not the case for signal events.

[1] The meaning of some variables have been explained in section 7.4.1.

- $\Delta\phi_{e,\not{E}_T}$ – Because the electron and neutrino have to form a W boson in $t\bar{t}$, $W+$ jet, and WW events, their $\Delta\phi_{e,\not{E}_T}$ spectra deplete near $\Delta\phi_{e,\not{E}_T} = 0$. For QCD multijet events, the $\Delta\phi_{e,\not{E}_T}$ spectrum peaks around 0 and π because $\not{E}_T$ could be caused by measurement fluctuation of the fake electron energy or its recoils.

- $\mathcal{A}$ – $W+$ jet, WW, and QCD multijet events are more likely to be collinear due to QCD bremsstrahlung while the signal and $t\bar{t}$ events are more likely to be spherical.

- $cos(\theta_j^*)$ – θ_j^* is the polar angle of the higher energy jet which comes from W decay in the rest frame of parent W. We calculated it by fitting the events to $t\bar{t}$ events. For $t\bar{t}$, the spectrum is flat but for signal and other SM backgrounds, it is not.

- $cos(\theta_e^*)$ – θ_e^* has been defined in section 7.4.1 The signal has moderately different $cos(\theta_e^*)$ distribution from SM background, especially $t\bar{t}$.

The spectra of these variables are shown in Figure 8.1.

Based on the plots we claim that we observed no excess in our data due to mSUGRA events. We also plotted in Figure 8.2 the difference in $cos(\theta_j^*)$ and $cos(\theta_e^*)$ between signal and $t\bar{t}$ events. These two variables are particularly useful in reducing $t\bar{t}$ background. The result of Neural Network training is shown in Figure 8.3. The backgrounds and signal are normalized to their expected number of event in data respectively. $t\bar{t}$ has a large contribution in the signal-rich region because it has similar kinematics to the mSUGRA signal. We also plot the Neural Network output of data in Figure 8.4. Again the expected background describes the data very well.

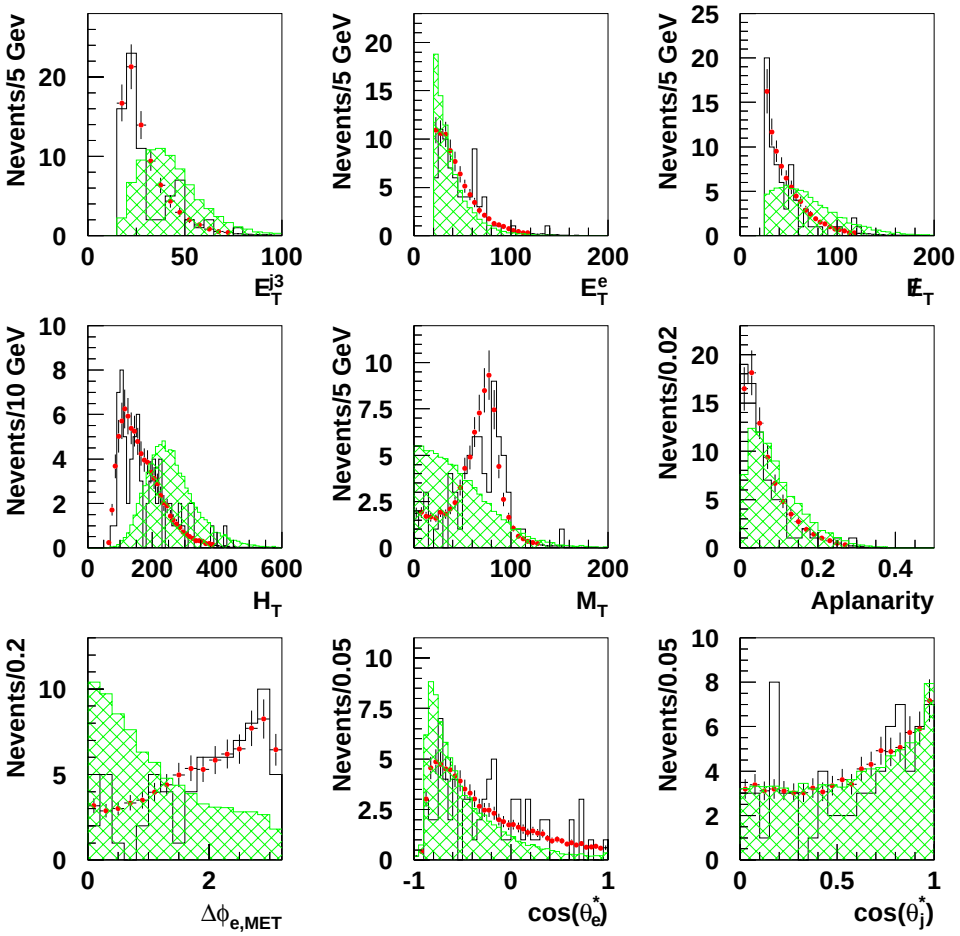

Figure 8.1 Distribution of Neural Network variables for data (histogram), background (circles) and signal (hatched histogram). The number of signal events is normalized to the number of background events. The signal was generated with $M_0 = 170$ GeV, $M_{1/2} = 58$ GeV and $\tan(\beta) = 3.0$.

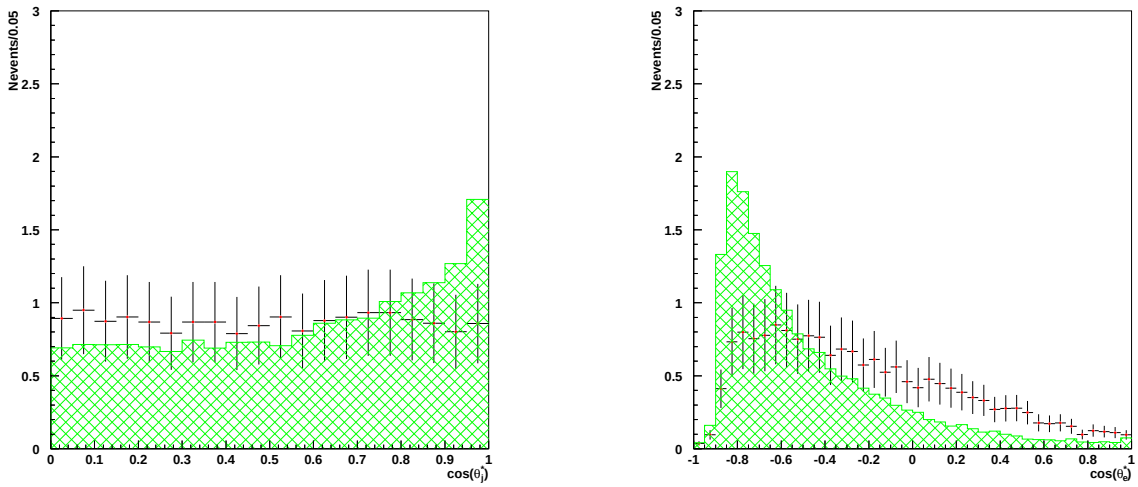

Figure 8.2 Distribution of $cos(\theta_j^*)$ (left) and $cos(\theta_e^*)$ (right) for the signal (hatched histogram) and $t\bar{t}$ (histogram) events. The number of events was normalized to the number of $t\bar{t}$ events expected in our final sample.

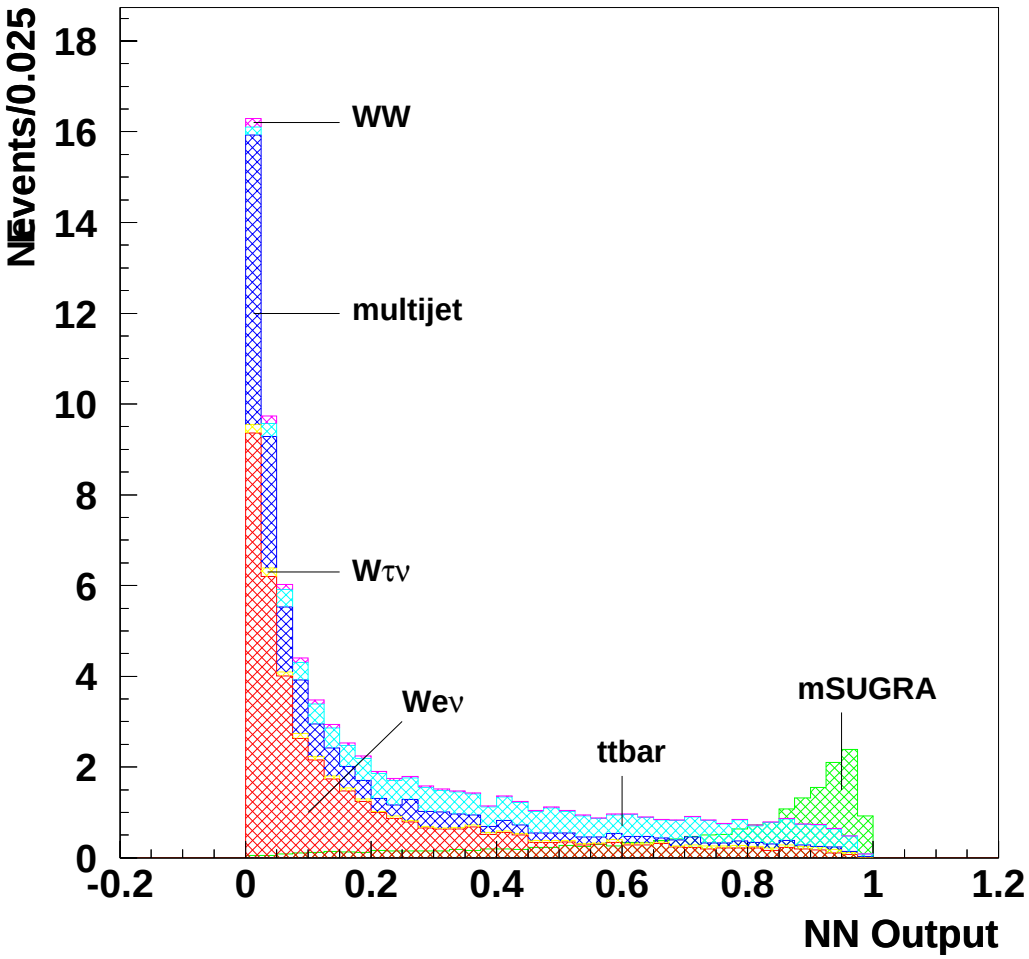

Figure 8.3 Result of Neural Network training. The small bump on the right end of the distribution is the expected signal. The signal was generated with $M_0 = 170$ GeV, $M_{1/2} = 58$ GeV and $\tan(\beta) = 3.0$. The backgrounds are stacked up in the order of $W(e\nu)+$ jet, $W(\tau\nu)+$ jet, QCD multijet, $t\bar{t}$, and WW. All events are normalized to their expected number of events in data.

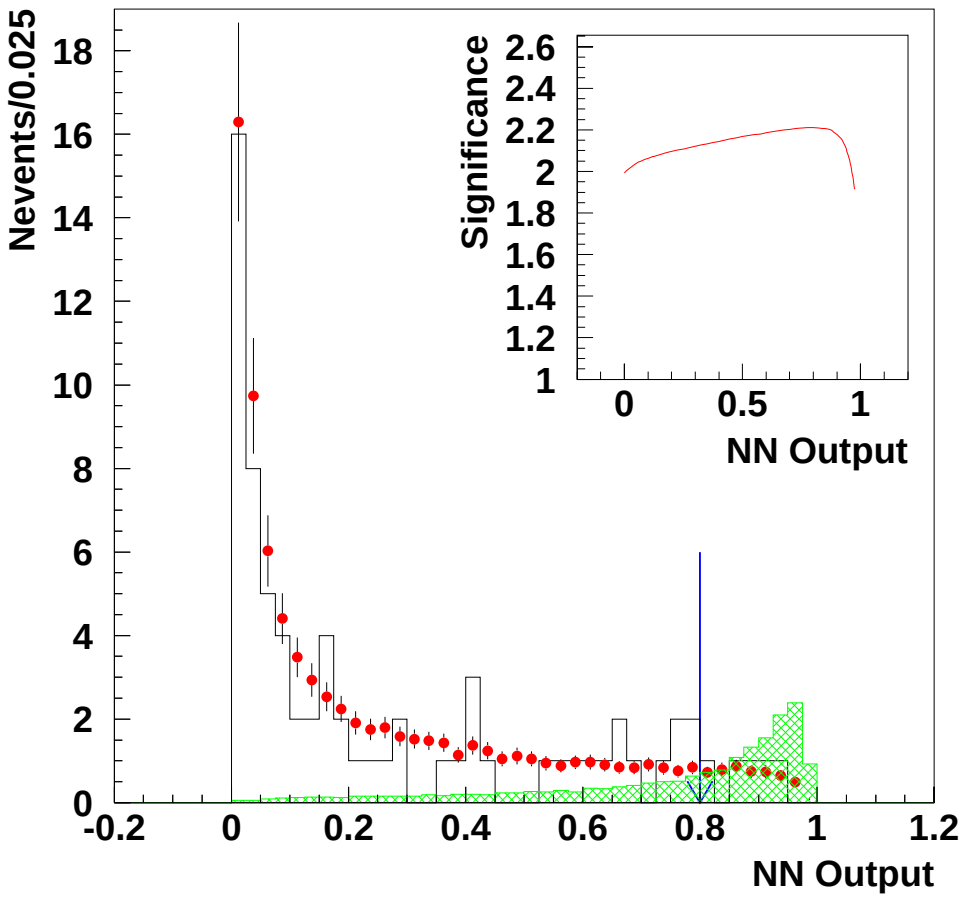

Figure 8.4 Neural Network output for the data (histogram), signal (hatched histogram) and background (points). The signal was generated with $M_0 = 170$ GeV, $M_{1/2} = 58$ GeV and $\tan(\beta) = 3.0$. The background expectation describes the data very well. The line indicates the cut on NN output which corresponds to the maximum signal significance. The significance (described in section 8.2) as a function of NN output is also plotted.

8.2 Signal Significance

In order to apply the optimal cut on the NN output, we calculated the signal significance based on the expected number of signal and background events which would survive a NN cut [66]. The probability that the number of background events, b, fluctuates to n or more events is:

$$F(n|b) = \sum_{k=n}^{\infty} \frac{b^k e^{-b}}{k!} = \frac{1}{\sqrt{2\pi}} \int_{s(n|b)}^{\infty} e^{-t^2}\, dt, \tag{8.1}$$

where $\frac{b^k e^{-b}}{k!}$ is the Poisson probability for observing k events with b events expected. $s(n|b)$ can be regarded as the number of standard deviations, an alternative way of quoting the fluctuation probability. It can be solved numerically. The actual observed number of data events can be any number between $[0, \infty)$ with $s + b$ events expected. The significance is thus defined as:

$$\overline{s} = \sum_{n=0}^{\infty} p(n|s+b) \cdot s(n|b) \tag{8.2}$$

where $p(n|s+b)$ is the Poisson probability for observing n events with $s + b$ events expected.

The NN output corresponding to the maximum significance is where we set our cut to calculate the 95% confidence level (C.L.) signal cross section limit. The algorithm is described in detail in Ref. [67] and is outlined below.

The 95% C.L. signal cross section upper limit, σ_{ul} is defined as:

$$0.95 = \int_0^{\sigma_{ul}} P(\sigma|k, I) d\sigma,$$

where $P(\sigma|k, I)$ is the probability of signal production cross section given k observed events and prior information I. Depending on the situation, the prior information can be derived or guessed *a priori* (see below).

What we really obtain after each experiment is the number of expected background events b, the signal (if it exists) acceptance ε, and the luminosity $\mathcal{L}$, from which the likelihood of observing k events given σ, ε, b, $\mathcal{L}$, and I can be calculated:

$$P(k|\sigma,\varepsilon,b,\mathcal{L},I) = \frac{e^{-(b+\mathcal{L}\sigma\varepsilon)}(b+\mathcal{L}\sigma\varepsilon)^k}{k!}.$$

To obtain $P(\sigma|k,I)$ from $P(k|\sigma,\varepsilon,b,\mathcal{L},I)$ we use the Bayes theorem, which states that:

$$P(A|BC) = \frac{P(B|AC)P(A|C)}{P(B|C)}.$$

It is then straightforward to write down $P(\sigma,\varepsilon,b,\mathcal{L}|k,I)$ in terms of $P(k|\sigma,\varepsilon,b,\mathcal{L},I)$:

$$\begin{aligned} P(\sigma,\varepsilon,b,\mathcal{L}|k,I) &\propto c\cdot P(k|\sigma,\varepsilon,b,\mathcal{L},I)P(\sigma,\varepsilon,b,\mathcal{L}|I) \\ &= c\cdot P(k|\sigma,\varepsilon,b,\mathcal{L},I)P(\varepsilon,b,\mathcal{L}|I)P(\sigma|I), \end{aligned} \tag{8.3}$$

where c is a normalization constant which satisfies:

$$\int_0^\infty d\sigma \int_0^1 d\epsilon \int_0^\infty db \int_0^\infty d\mathcal{L}\; P(\sigma,\varepsilon,b,\mathcal{L}|k,I) = 1.$$

We have divided the prior probability into two parts: $P(\varepsilon,b,\mathcal{L}|I)$ and $P(\sigma|I)$. ε, b, and $\mathcal{L}$ are all experimentally measured quantity. We assume that they have a normal distribution and are positive. (None of these variables cannot be negative physically.) The distribution of σ is not known. We used a flat prior, that is:

$$P(\sigma|I) = \begin{cases} 1/\sigma_{max} & \text{if } 0 \le \sigma \le \sigma_{\max} \\ 0 & \text{otherwise,} \end{cases}$$

where σ_{max} is chosen large enough that the likelihood function $P(k|\sigma,\varepsilon,b,\mathcal{L},I)$ is negligible for $\sigma > \sigma_{max}$.

To obtain $P(\sigma|k,I)$, we integrate $P(\sigma,\varepsilon,b,\mathcal{L}|k,I)$ calculated in Equation 8.3 over the nuisance variables: ε, b and $\mathcal{L}$.

Table 8.1 lists the signal, background, and data events as a function of NN output cut. The signal was generated with $M_0 = 170$ GeV, $M_{1/2} = 58$ GeV and $\tan(\beta) = 3.0$. Table 8.2 lists the 95%C.L. cross section limit for various signal model points.

Table 8.1 Number of observed data events—N_{obs}, expected total background events N_{bkgd}^{total} and its breakdown in various sources, expected signal events N_{SUSY}, signal acceptance a_{SUSY} and significance $\overline{s}$ as a function of NN output cut. The signal was generated with $M_0 = 170$ GeV, $M_{1/2} = 58$ GeV and $\tan(\beta) = 3.0$.

NN cut	N_{obs}	N_{bkgd}^{total}	N_{QCD}	$N_{t\overline{t}}$	$N_{We\nu}$	$N_{W\tau\nu}$	N_{WW}	N_{SUSY}	$a_{SUSY}(\%)$	$\overline{s}$
0.000	72	80.84 ± 10.48	19.08 ± 4.72	17.39 ± 5.45	40.77 ± 7.59	2.18 ± 0.41	1.42 ± 0.32	18.48 ± 3.27	0.537 ± 0.095	1.99
0.050	48	54.81 ± 7.50	9.81 ± 2.44	16.92 ± 5.30	25.21 ± 4.70	1.80 ± 0.34	1.06 ± 0.24	18.38 ± 3.25	0.534 ± 0.094	2.04
0.100	39	44.37 ± 6.40	7.21 ± 1.80	16.14 ± 5.06	18.57 ± 3.46	1.61 ± 0.30	0.85 ± 0.19	18.17 ± 3.22	0.528 ± 0.093	2.06
0.150	35	37.96 ± 5.71	5.88 ± 1.47	15.25 ± 4.78	14.68 ± 2.74	1.46 ± 0.27	0.70 ± 0.16	17.92 ± 3.17	0.521 ± 0.092	2.08
0.200	29	33.19 ± 5.17	4.99 ± 1.25	14.30 ± 4.48	11.97 ± 2.24	1.33 ± 0.25	0.59 ± 0.13	17.67 ± 3.13	0.513 ± 0.091	2.10
0.250	27	29.53 ± 4.69	4.46 ± 1.12	13.21 ± 4.14	10.11 ± 1.89	1.26 ± 0.24	0.50 ± 0.11	17.36 ± 3.07	0.504 ± 0.089	2.11
0.300	24	26.15 ± 4.26	3.67 ± 0.93	12.21 ± 3.83	8.66 ± 1.62	1.19 ± 0.23	0.43 ± 0.10	17.06 ± 3.02	0.495 ± 0.088	2.12
0.350	24	23.16 ± 3.87	3.01 ± 0.76	11.26 ± 3.53	7.39 ± 1.38	1.13 ± 0.21	0.37 ± 0.08	16.72 ± 2.96	0.486 ± 0.086	2.13
0.400	22	20.58 ± 3.52	2.65 ± 0.68	10.37 ± 3.25	6.19 ± 1.16	1.05 ± 0.20	0.32 ± 0.07	16.37 ± 2.90	0.475 ± 0.084	2.14
0.450	18	17.97 ± 3.14	2.24 ± 0.57	9.35 ± 2.93	5.12 ± 0.96	0.99 ± 0.19	0.28 ± 0.06	15.98 ± 2.83	0.464 ± 0.082	2.16
0.500	18	15.81 ± 2.79	1.90 ± 0.49	8.32 ± 2.61	4.44 ± 0.84	0.90 ± 0.17	0.24 ± 0.05	15.52 ± 2.75	0.451 ± 0.080	2.17
0.550	17	13.82 ± 2.46	1.59 ± 0.41	7.38 ± 2.31	3.81 ± 0.72	0.83 ± 0.16	0.20 ± 0.05	15.00 ± 2.66	0.436 ± 0.077	2.18
0.600	15	11.98 ± 2.18	1.33 ± 0.35	6.56 ± 2.06	3.17 ± 0.60	0.74 ± 0.14	0.18 ± 0.04	14.45 ± 2.56	0.420 ± 0.074	2.19
0.650	13	10.10 ± 1.87	1.03 ± 0.28	5.66 ± 1.77	2.60 ± 0.49	0.67 ± 0.13	0.15 ± 0.03	13.77 ± 2.44	0.400 ± 0.071	2.20
0.700	10	8.42 ± 1.59	0.81 ± 0.22	4.84 ± 1.52	2.05 ± 0.39	0.61 ± 0.12	0.13 ± 0.03	12.98 ± 2.30	0.377 ± 0.067	2.20
0.750	9	6.68 ± 1.28	0.56 ± 0.16	3.91 ± 1.23	1.61 ± 0.31	0.49 ± 0.10	0.10 ± 0.02	12.01 ± 2.13	0.349 ± 0.062	2.21
0.800	5	5.08 ± 0.99	0.40 ± 0.12	3.03 ± 0.95	1.18 ± 0.23	0.39 ± 0.08	0.08 ± 0.02	10.86 ± 1.92	0.315 ± 0.056	2.21
0.850	4	3.56 ± 0.71	0.24 ± 0.08	2.19 ± 0.69	0.79 ± 0.16	0.29 ± 0.06	0.05 ± 0.01	9.35 ± 1.66	0.272 ± 0.048	2.21
0.900	2	1.96 ± 0.41	0.10 ± 0.04	1.27 ± 0.40	0.37 ± 0.08	0.19 ± 0.04	0.03 ± 0.01	6.95 ± 1.23	0.202 ± 0.036	2.18
0.950	0	0.57 ± 0.13	0.03 ± 0.02	0.39 ± 0.13	0.09 ± 0.02	0.06 ± 0.02	0.01 ± 0.00	3.30 ± 0.59	0.096 ± 0.017	2.07

Table 8.2 Number of observed data events N_{obs}, expected total background events N_{bkgd}^{total} and expected signal events N_{SUSY} corresponding to the optimal NN cut for different model points. The signal acceptance before NN cut a_{SUSY}^{preNN} and after NN cut a_{SUSY}^{postNN}, *mSUGRA* production cross section at each model point and the calculated 95% C.L. cross section upper limit are also listed. All models have $\tan(\beta) = 3$. This table lists results for 150 GeV $\leq M_0 \leq$ 200 GeV.

M_0 (GeV)	$M_{1/2}$ (GeV)	NN cut	N_{obs}	N_{bkgd}^{total}	N_{SUSY}	a_{SUSY}^{preNN} (%)	a_{SUSY}^{postNN} (%)	σ_{th} (pb)	σ_{ul} (pb)
160	60	0.800	4	5.01 ± 0.98	9.90 ± 1.76	0.565 ± 0.039	0.321 ± 0.057	33.34	21.24
160	63	0.800	5	5.15 ± 1.00	8.48 ± 1.50	0.575 ± 0.040	0.341 ± 0.060	26.84	22.92
160	65	0.825	6	5.00 ± 0.99	7.11 ± 1.26	0.576 ± 0.040	0.327 ± 0.058	23.48	28.25
160	70	0.775	5	5.99 ± 1.16	5.22 ± 0.93	0.527 ± 0.037	0.327 ± 0.058	17.24	22.64
170	58	0.800	5	5.08 ± 0.99	10.86 ± 1.92	0.537 ± 0.037	0.315 ± 0.056	37.16	24.87
170	63	0.825	5	4.57 ± 0.90	7.89 ± 1.40	0.585 ± 0.040	0.335 ± 0.059	25.38	24.44
170	65	0.850	3	3.71 ± 0.77	6.36 ± 1.13	0.573 ± 0.040	0.309 ± 0.055	22.23	20.38
170	70	0.850	5	3.71 ± 0.76	4.61 ± 0.82	0.566 ± 0.039	0.303 ± 0.054	16.38	29.32
170	75	0.825	4	4.43 ± 0.88	3.34 ± 0.59	0.493 ± 0.034	0.292 ± 0.052	12.34	24.35
180	63	0.850	3	3.85 ± 0.79	6.98 ± 1.24	0.559 ± 0.038	0.312 ± 0.055	24.16	19.98
180	65	0.850	3	3.66 ± 0.78	6.18 ± 1.09	0.556 ± 0.038	0.315 ± 0.056	21.17	20.05
180	67	0.825	4	4.31 ± 0.90	5.77 ± 1.02	0.555 ± 0.038	0.333 ± 0.059	18.69	21.55
180	70	0.875	3	2.76 ± 0.59	4.00 ± 0.71	0.540 ± 0.037	0.276 ± 0.049	15.63	24.56
190	60	0.850	2	3.53 ± 0.75	7.56 ± 1.34	0.500 ± 0.034	0.284 ± 0.050	28.76	18.64
190	63	0.875	2	3.06 ± 0.66	5.89 ± 1.04	0.519 ± 0.035	0.275 ± 0.049	23.17	19.81
190	65	0.900	3	2.20 ± 0.49	4.60 ± 0.81	0.522 ± 0.036	0.245 ± 0.043	20.30	29.38
190	66	0.875	2	3.13 ± 0.68	5.04 ± 0.89	0.528 ± 0.036	0.285 ± 0.050	19.07	19.01
190	67	0.875	3	3.21 ± 0.70	4.76 ± 0.84	0.533 ± 0.036	0.286 ± 0.051	17.95	22.89
190	70	0.875	3	2.85 ± 0.61	3.94 ± 0.70	0.530 ± 0.036	0.283 ± 0.050	15.04	23.77
200	60	0.875	1	2.91 ± 0.61	6.11 ± 1.08	0.462 ± 0.032	0.237 ± 0.042	27.77	18.59
200	62	0.850	5	3.55 ± 0.77	6.09 ± 1.08	0.479 ± 0.033	0.275 ± 0.049	23.96	32.90
200	65	0.900	0	1.98 ± 0.45	4.14 ± 0.73	0.489 ± 0.033	0.228 ± 0.040	19.62	15.49
200	67	0.900	2	2.17 ± 0.48	3.92 ± 0.69	0.494 ± 0.034	0.244 ± 0.043	17.32	23.77

Table 8.2 (continued) Number of observed data events N_{obs}, expected total background events N_{bkgd}^{total} and expected signal events N_{SUSY} corresponding to the optimal NN cut for different model points. The signal acceptance before NN cut a_{SUSY}^{preNN} and after NN cut a_{SUSY}^{postNN}, *mSUGRA* production cross section at each model point and the calculated 95% C.L. cross section upper limit are also listed. All models have $\tan(\beta) = 3$. This table lists results for 210 GeV $\leq M_0 \leq$ 260 GeV.

M_0 (GeV)	$M_{1/2}$ (GeV)	NN cut	N_{obs}	N_{bkgd}^{total}	N_{SUSY}	a_{SUSY}^{preNN}(%)	a_{SUSY}^{postNN}(%)	σ_{th} (pb)	σ_{ul} (pb)
210	57	0.825	3	4.31 ± 0.91	7.36 ± 1.30	0.378 ± 0.026	0.226 ± 0.040	35.17	26.88
210	60	0.825	3	4.41 ± 0.95	6.23 ± 1.10	0.411 ± 0.028	0.250 ± 0.044	26.96	24.25
210	62	0.850	4	3.73 ± 0.81	5.41 ± 0.96	0.432 ± 0.029	0.251 ± 0.044	23.30	29.78
210	65	0.875	4	3.00 ± 0.69	4.41 ± 0.78	0.452 ± 0.031	0.250 ± 0.044	19.04	31.85
220	57	0.875	1	2.88 ± 0.65	5.50 ± 0.97	0.329 ± 0.022	0.172 ± 0.030	34.42	25.71
220	60	0.875	1	2.89 ± 0.65	4.89 ± 0.86	0.374 ± 0.025	0.201 ± 0.035	26.32	22.10
220	61	0.875	2	2.85 ± 0.64	4.74 ± 0.84	0.383 ± 0.026	0.210 ± 0.037	24.39	26.35
220	65	0.875	3	2.58 ± 0.60	3.81 ± 0.67	0.404 ± 0.027	0.221 ± 0.039	18.60	31.27
230	47	0.825	3	4.47 ± 0.92	6.87 ± 1.22	0.067 ± 0.005	0.040 ± 0.007	187.53	151.94
230	50	0.825	3	4.52 ± 0.94	6.39 ± 1.13	0.084 ± 0.006	0.050 ± 0.009	138.52	120.64
230	53	0.850	3	3.35 ± 0.71	5.77 ± 1.02	0.145 ± 0.010	0.082 ± 0.014	76.19	79.05
230	57	0.850	3	3.32 ± 0.74	5.40 ± 0.95	0.299 ± 0.020	0.172 ± 0.030	33.88	37.72
240	41	0.900	1	2.05 ± 0.47	4.85 ± 0.86	0.042 ± 0.003	0.018 ± 0.003	283.25	248.49
240	45	0.875	1	2.79 ± 0.62	5.01 ± 0.89	0.053 ± 0.004	0.026 ± 0.005	211.99	174.32
240	50	0.850	1	3.66 ± 0.78	5.25 ± 0.93	0.075 ± 0.005	0.042 ± 0.007	135.95	103.48
240	52	0.900	1	2.09 ± 0.47	4.16 ± 0.74	0.099 ± 0.007	0.045 ± 0.008	100.14	102.35
240	55	0.850	4	3.68 ± 0.80	5.00 ± 0.88	0.221 ± 0.015	0.122 ± 0.022	44.21	61.47
250	41	0.825	3	4.33 ± 0.87	5.80 ± 1.03	0.037 ± 0.003	0.022 ± 0.004	281.53	272.08
250	42	0.825	3	4.20 ± 0.85	5.42 ± 0.96	0.039 ± 0.003	0.023 ± 0.004	259.36	270.30
250	43	0.900	2	2.17 ± 0.48	4.23 ± 0.75	0.042 ± 0.003	0.019 ± 0.003	238.96	303.58
260	41	0.850	2	3.55 ± 0.73	4.67 ± 0.83	0.034 ± 0.002	0.018 ± 0.003	280.15	293.53
260	42	0.850	5	3.92 ± 0.79	4.68 ± 0.83	0.036 ± 0.002	0.020 ± 0.003	257.67	443.57

9 RESULTS

The 95% confidence level exclusion contour is plotted in Figure 9.1. Plotted in the same figure is the DØ dilepton and LEP I 95% C.L. exclusion contour. The single electron analysis is sensitive in the large M_0 region. Extended exclusion region from the dilepton result is obtained between $m_0 = (165, 250)$ GeV. The amount of extension is limited because our analysis suffers a large and hard-to-reduce $t\bar{t}$ background.

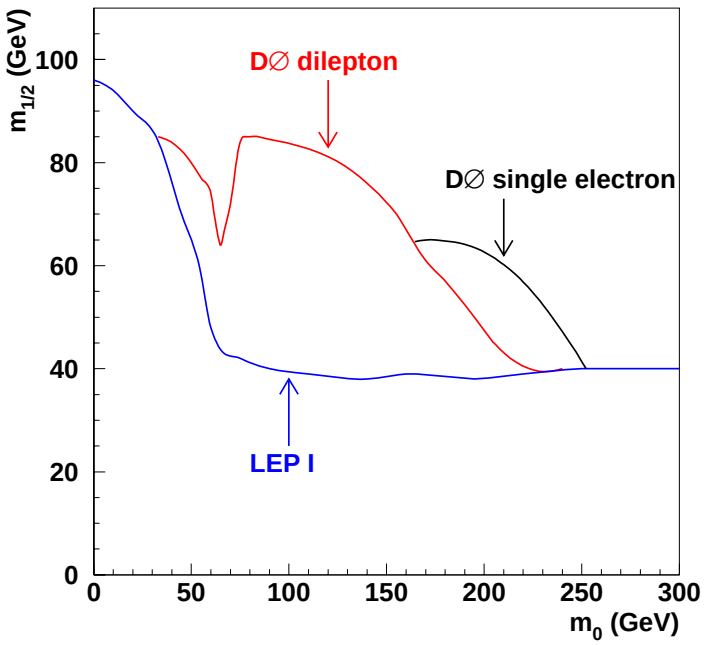

Figure 9.1 95% C.L. exclusion contour for mSUGRA with $\tan(\beta) = 3.0$. Also plotted is the result of DØ dilepton [41] and LEP I [31] analyses.

10 PRODUCTION CROSS SECTION OF $t\bar{t}$

Since we did not find evidence of a mSUGRA signature in our data and since $t\bar{t}$ is the largest background to our signal after Neural Network cut, we can turn the problem around to measure the $t\bar{t}$ production cross section: $\sigma_{t\bar{t}}$. The cross section has been measured by both DØ: $\sigma_{t\bar{t}} = 5.9 \pm 1.7$ pb [56] and CDF: $\sigma_{t\bar{t}} = 6.5^{+1.7}_{-1.4}$ pb [68]. Both results are combined results of all $t\bar{t}$ decay channels. For DØ, the analysis of the single electron channel [1], based on 115.0 pb^{-1} of data, yields $\sigma_{t\bar{t}} = 2.94 \pm 2.13$ pb. That analysis used a grid cut on two variables: $H_T > 180$ GeV and $\mathcal{A} > 0.065$ to enhance the signal to background ratio. We describe in this section a Neural Network approach to enhance the signal to background ratio and a new $\sigma_{t\bar{t}}$ measurement.

10.1 $W+$ jets Background

We again use the scaling method to estimate the number of $W+ \geq 4$ jet events. Caveat must be taken because we cannot assume a known $\sigma_{t\bar{t}}$ in measuring the scaling factor, α as we did in search for mSUGRA in section 7.4.1.

10.1.1 Measuring the Scaling Factor: α

From the observed number of events (N_{obs}), we subtract the number of QCD multijet (N_{QCD}) and WW (N_{WW}) events at each inclusive jet multiplicity. The remaining number of events (N_i) are from $W+$ jet and $t\bar{t}$. We fit these numbers of events at each inclusive jet multiplicity to Equation 10.1 with α and $\sigma_{t\bar{t}}$ as parameters:

[1] The analysis did not use muon tag to reduce the background and focused on optimizing kinematic variables only. This is exactly what we do here.

$$N_{obs} - N_{QCD} - N_{WW} = N_i = \overline{N}_1^W \cdot \alpha^{i-1} + \sigma_{t\bar{t}} \cdot \mathcal{L} \cdot a_i^{t\bar{t}}. \tag{10.1}$$

where $a_i^{t\bar{t}}$ is the acceptance of $t\bar{t}$ events which are required to have at least i good jets and to have passed the EM1_EISTRKCC_CC trigger. The N_{obs}, N_{QCD}, N_{WW}, $t\bar{t}$, and $a_i^{t\bar{t}}$ are listed in Table 10.1. The integrated luminosity $\mathcal{L} = 92.7$ pb^{-1}. The fit is shown in Figure 10.1 and the fitted $\alpha = 0.190 \pm 0.011$.

Table 10.1 Estimating the scaling factor α by fitting N_i to Equation 10.1 (see text). The numbers are pertinent to the EM1_EISTRKCC_MS trigger.

N_{jet}	≥ 1	≥ 2	≥ 3	≥ 4
N_{obs}	8191	1691	353	64
N_{QCD}	825.7 ± 95.3	290.9 ± 47.6	74.9 ± 15.3	16.6 ± 7.0
N_{WW}	38.8 ± 3.8	27.1 ± 2.8	7.1 ± 1.1	1.29 ± 0.30
N_i	7326.5 ± 131.5	1372.9 ± 63.0	271.0 ± 24.3	46.1 ± 10.6
$a_i^{t\bar{t}}$	0.0563	0.0570	0.0477	0.0292

10.1.2 Estimating the Number of $W+ \geq 4$ jet Events

From Equation 10.1 we can write the following equations:

$$\begin{cases} \alpha \cdot N_3 & = N_4^W \cdot \frac{\varepsilon_{trig}^{W3}}{\varepsilon_{trig}^{W4}} + \alpha \cdot \sigma_{t\bar{t}} \cdot \mathcal{L} \cdot a_3^{t\bar{t}} \\ N_4 & = N_4^W + \sigma_{t\bar{t}} \cdot \mathcal{L} \cdot a_4^{t\bar{t}}. \end{cases} \tag{10.2}$$

Note that these two equations are for the ELE_JET_HIGH(A) triggered data. ε_{trig}^{W3} and ε_{trig}^{W4} are trigger efficiencies of $W+ \geq 3$ jet and $W+ \geq 4$ jet events, respectively. They are shown in Table 6.6; $a_3^{t\bar{t}}$ and $a_4^{t\bar{t}}$ are acceptances of $t\bar{t}$ events with ≥ 3 and ≥ 4 jets, respectively. They are shown in Table 10.2. Solving the equations simultaneously, we obtained the number of $W+ \geq 4$ jet events (N_4^W) in Equation 10.3:

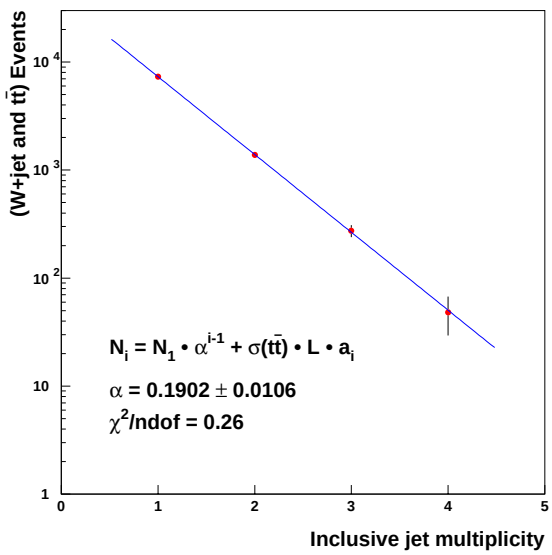

Figure 10.1 Fitting N_i to Equation 10.1 (see text). We assume that the number of $W+$ jet events follows scaling law as a function of inclusive jet multiplicity.

$$
\begin{aligned}
N_4^W &= \frac{\alpha \cdot (N_3 \cdot a_4^{t\bar{t}} - N_4 \cdot a_3^{t\bar{t}})}{\frac{\varepsilon_{trig}^{W3}}{\varepsilon_{trig}^{W4}} \cdot a_4^{t\bar{t}} - \alpha \cdot a_3^{t\bar{t}}} \\
&= \frac{0.1902 \times (271.7 \cdot 0.0319 - 51.5 \cdot 0.0524)}{\frac{0.925}{0.957} \cdot 0.0319 - 0.1902 \cdot 0.0524} \\
&= 54.4 \pm 11.1. \qquad (10.3)
\end{aligned}
$$

The error on N_4^W is dominated by the error on the number of ≥ 4 jet events (19%), the error on the scaling method itself (10%), and the error on the number of ≥ 3 jet events (9.0%). The error on $\varepsilon_{trig}^{W3}/\varepsilon_{trig}^{W4}$ is obtained using the method described in section 7.4.3.

The sum of N_4^W, N_QCD, and N_{WW} is 74.9. It already exceeds the number of observed events and leaves little room for $t\bar{t}$ events. However, it is very likely that this is a upward fluctuation of N_4^W in our data. This fluctuation becomes less important when signal optimization is applied to enhance the signal to background ratio (see section 10.2).

Table 10.2 Numbers used in Equation 10.3. They are pertinent to the ELE_JET_HIGH(A) trigger.

N_{jet}	≥ 3	≥ 4
N_{obs}	362	72
N_{QCD}	82.6	19.1
N_{WW}	7.69	1.42
N_i	271.7	51.5
$a_i^{t\bar{t}}$	0.0524	0.0319

10.2 Measuring the $\sigma_{t\bar{t}}$

A Neural Network is again used to measure $\sigma_{t\bar{t}}$. The input variables are plotted in Figure 10.2. One new variable χ^2 comes from the 3C fit of the events to $t\bar{t}$ events (see Appendix C). The result of the Neural Network training is shown in Figure 10.3.

We calculated the $t\bar{t}$ signal significance as a function of NN cut. We then applied to data the NN cut which corresponds to the highest significance as described in section 8.2. From the number of data events which survived the cut and the number of background events which were expected to pass the cut we calculated $\sigma_{t\bar{t}}$. Since the significance calculation needs $\sigma_{t\bar{t}}$ as an input, we iterated the significance and $\sigma_{t\bar{t}}$ calculation until the input and output $\sigma_{t\bar{t}}$ were the same. The resulting NN distributions of data, $t\bar{t}$ signal and background are plotted in Figure 10.4. The maximum signal significance is achieved at NNOutput = 0.8. We observed 17 events and expect 5.47 ± 0.93 background events. The breakdown of the number of expected background events is shown in Table 10.3.

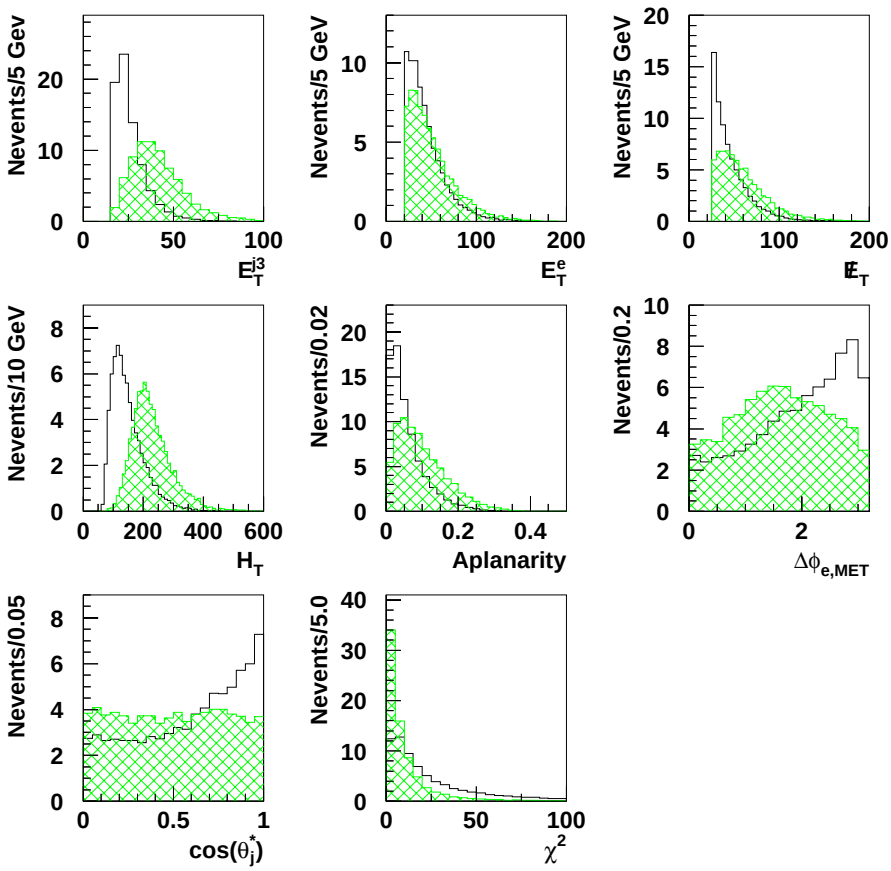

Figure 10.2 Distribution of Neural Network variables for $t\bar{t}$ signal (hatched histogram) and background (histogram). The number of $t\bar{t}$ events is normalized to the same number of background events.

From Equation 10.4, we obtain $\sigma_{t\bar{t}} = 6.13 \pm 2.44$ pb.

$$\begin{aligned}
\sigma_{t\bar{t}} &= \frac{N_{obs} - N_{bkgd}}{a_4^{t\bar{t}} \cdot \mathcal{L} \cdot \varepsilon_{NN}} \\
&= \frac{17 - 5.47}{0.0319 \cdot 92.7(\mathrm{pb}^{-1}) \cdot 0.637} \\
&= 6.13 \pm 2.19 \text{ (stat.)} \pm 1.07 \text{ (sys.) pb} \qquad (10.4)
\end{aligned}$$

Here are a few comparisons between the previous DØ analysis and this analysis:

- The previous DØ analysis in the single electron channel expected 8.3 $t\bar{t}$ and 4.51 ± 0.91

Table 10.3 Number of events for each background source after NN optimization (NNOutput ≥ 0.8).

N_4^W	N_{QCD}	N_{WW}
4.53 ± 0.91	0.74 ± 0.20	0.20 ± 0.05

background events in 115.0 pb^{-1} of data [56]. This yields a $t\bar{t}$ signal to background ratio: 1.84. The number of $t\bar{t}$ events was calculated using a theoretical cross section: $\sigma_{t\bar{t}}^{th} = 5.44$ pb. Using the same $\sigma_{t\bar{t}}^{th}$ in our analysis, which used 92.7 pb^{-1} of data (only 80.6% the amount of those in the previous analysis), we expect 10.2 $t\bar{t}$ and 5.47 ± 0.93 background events. The corresponding signal to background ratio is 1.86, comparable to that of the previous DØ analysis.

- Using two kinematic variables (H_T and $\mathcal{A}$), the previous DØ analysis observed 9 candidate events. Our analysis used more kinematic information in optimization and we observed 17 candidate events. Although our observed number of candidate events is more consistent with the expected sum of the signal and background events than in the previous analysis, the potentially large statistical fluctuation makes this consistency less significant.

- The $\sigma_{t\bar{t}}$'s measured in the two analyses differ by 1σ with $\sigma = \sqrt{2.44^2 + 2.13^2} = 3.24$. The two measurements also have comparable total errors.

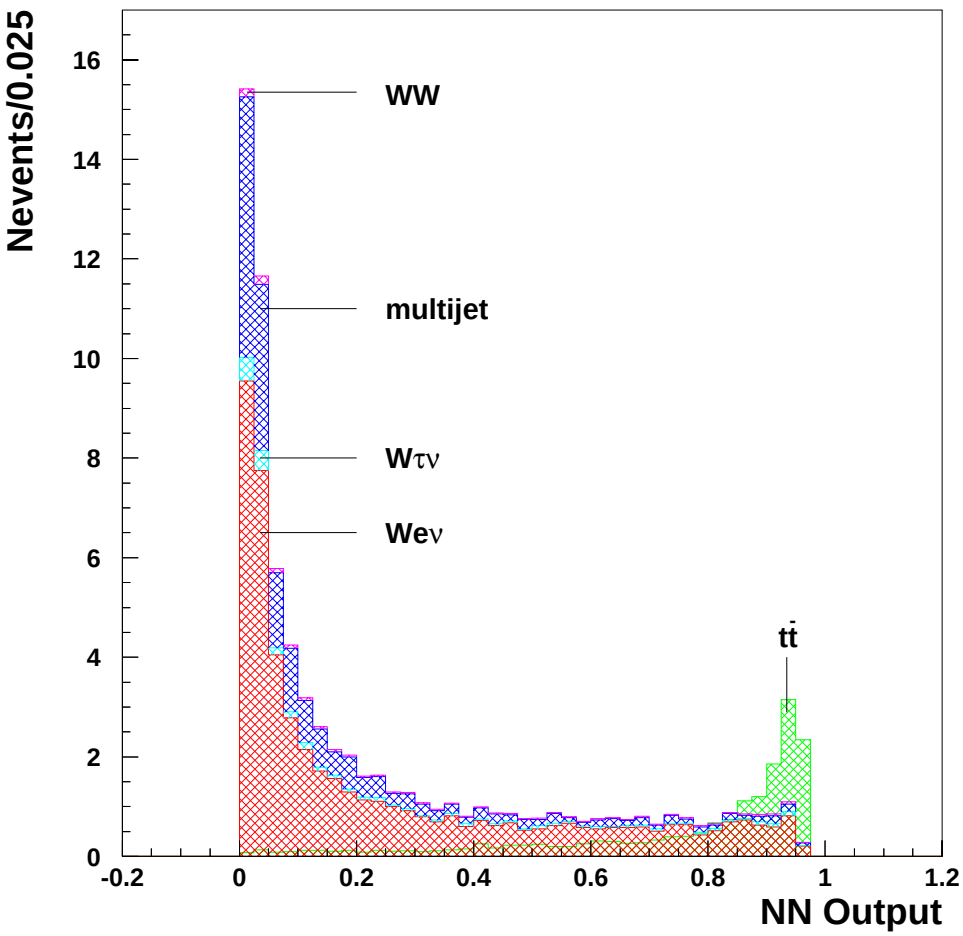

Figure 10.3 Result of Neural Network training. The background distribution peaks on the left and the $t\bar{t}$ signal peaks on the right. The right end of the distribution is the expected signal ($\sigma_{t\bar{t}} = 5.9$ pb was used). The backgrounds are stacked up in the order of $W(e\nu)+$ jet, $W(\tau\nu)+$ jet, QCD multijet, and WW. All events are normalized to their expected number of events in data respectively.

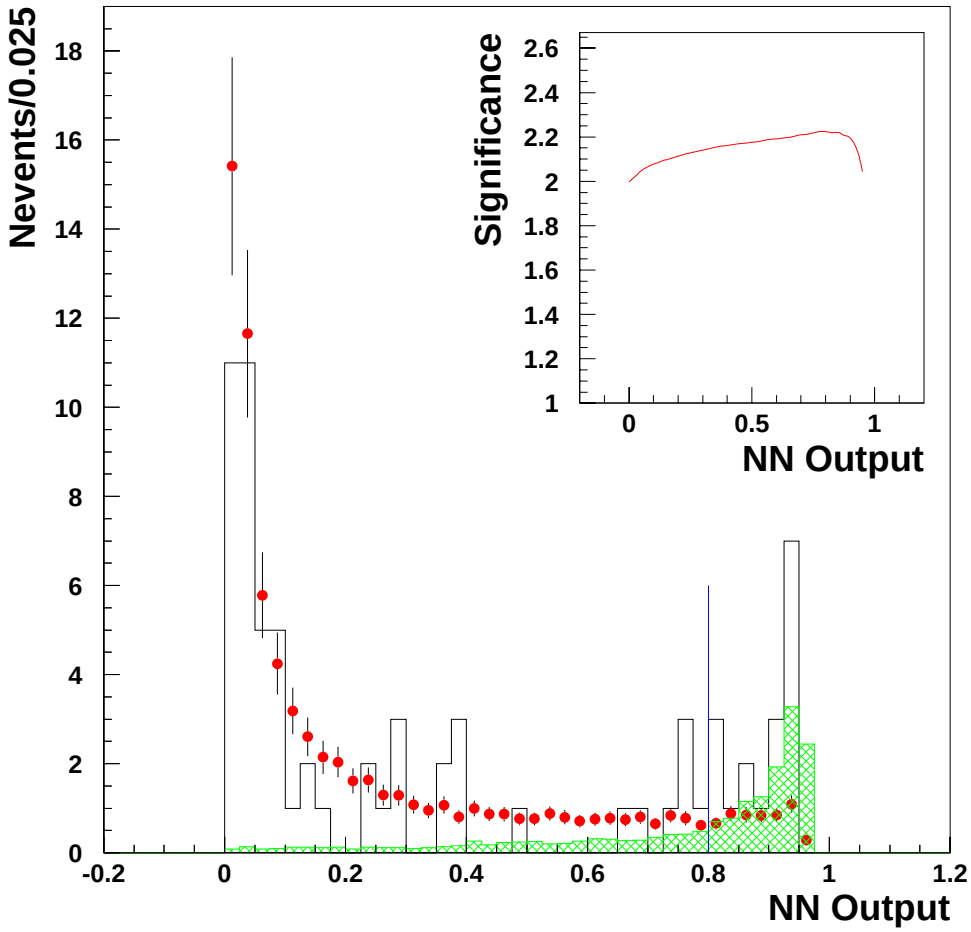

Figure 10.4 Neural Network output for the data (histogram), $t\bar{t}$ signal (hatched histogram), and background (points). The number of signal events is normalized to our measured $t\bar{t}$ cross section: $\sigma_{t\bar{t}} = 6.13$ pb. The line indicates the cut on NN output which corresponds to the highest signal significance.

APPENDIX A ICR AND EC JET ID EFFICIENCIES

We used the same method which was described in section 5.2 to derive the cuts and to calculate the ID efficiencies for ICR and EC jets. The related plots are shown in this appendix.

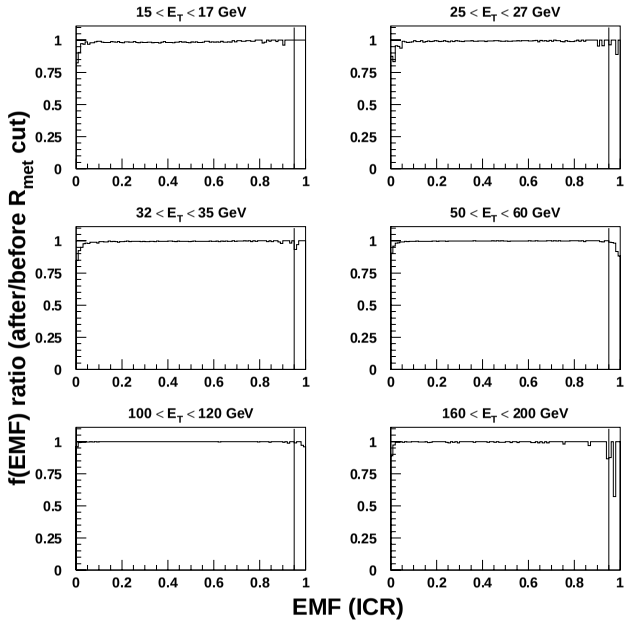

Figure A.1 Ratio of *emf* after and before the R_{MET} cut for the ICR jets. Depletion in the high end of the distribution indicates that the contribution of noise and fakes is not negligible.

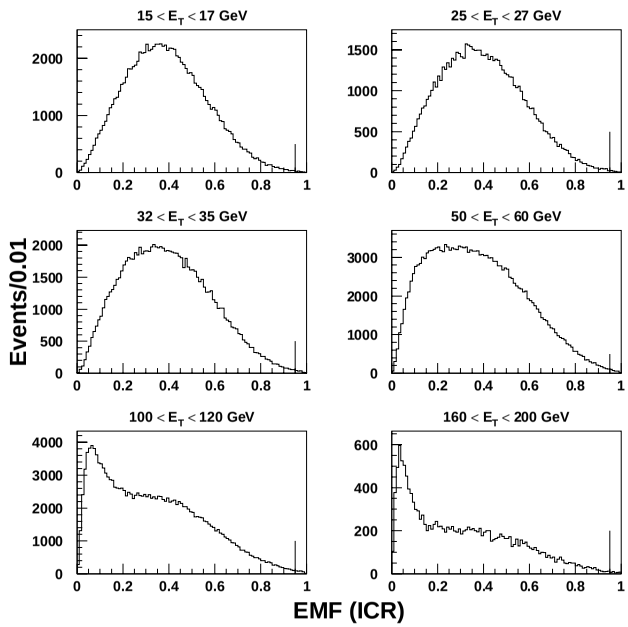

Figure A.2 ICR jet *emf* distribution after the R_{MET} cut. The lines indicate the *emf* cut. Jets with $emf < 0.95$ are accepted.

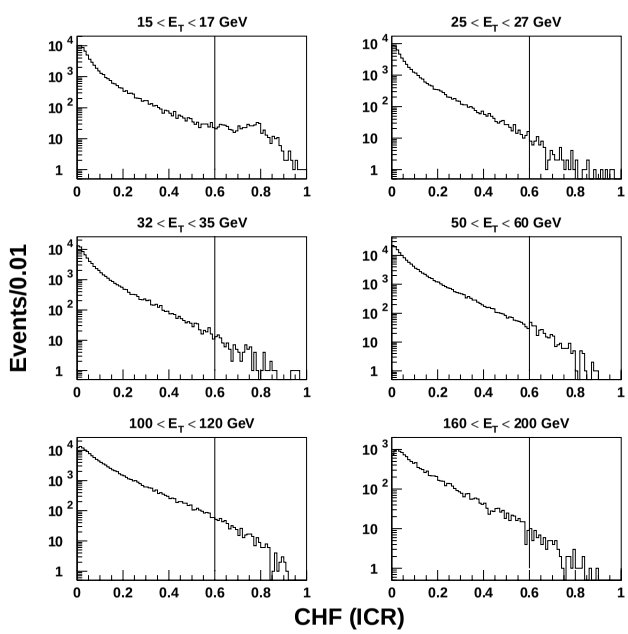

Figure A.3 ICR jet *chf* distribution after the R_{MET} and *emf* cuts. The lines indicate the *chf* cut. Jets with $chf < 0.6$ are accepted.

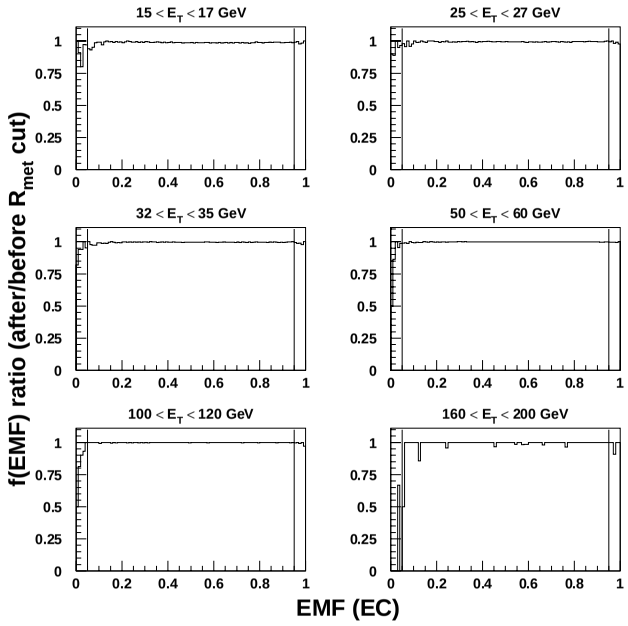

Figure A.4 Ratio of *emf* after and before the R_{MET} cut for the EC jets. Depletion in the low and high ends of the distribution indicate that the contribution of noise and fakes are not negligible.

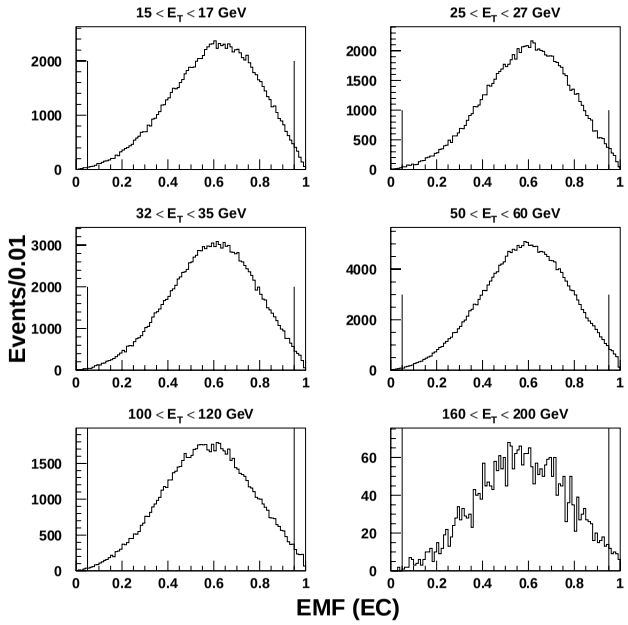

Figure A.5 EC jet *emf* distribution after the R_{MET} cut. The lines indicates the *emf* cut. Jets with $0.05 < emf < 0.95$ are accepted.

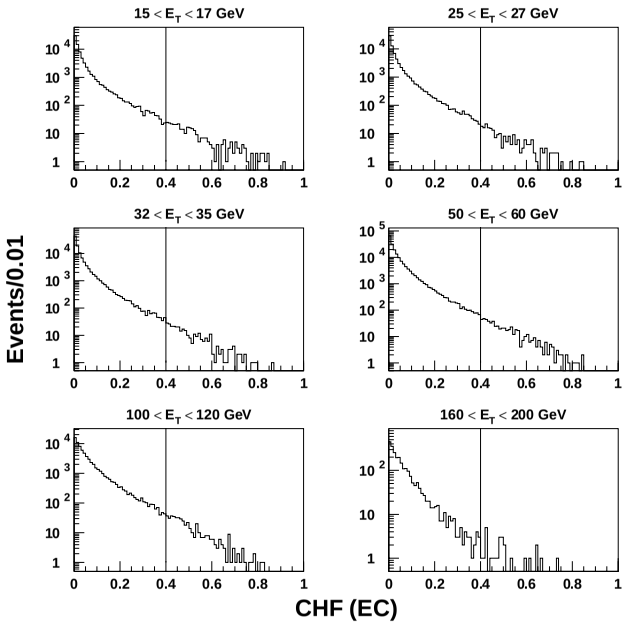

Figure A.6 EC jet *chf* distribution after the R_{MET} and *emf* cuts. The lines indicates the *chf* cut. Jets with $chf < 0.4$ are accepted.

APPENDIX B VECBOS AND QCD DYNAMIC SCALE Q^2

In this analysis, two QCD dynamic scales were used to generate VECBOS $W+$ jet events: $Q^2 = (\frac{1}{n}\sum_i E_T^{parton})^2$ (the "EJ" sample) and $Q^2 = M_W^2$ (the "MW" sample). Both samples were processed by HERWIG for fragmentation. In order to find out which sample models data better, we compared event kinematic variables of both MC samples with data. We added to the VECBOS $W+$ jet samples QCD multijet, $t\bar{t}$, and WW events in their respective proportion in the data [1]. The variables we investigated were those used in our Neural Networks (see Chapter 7 and 10). We found that though the variables related to the electron and the $\not\!\!E_T$ were indistinguishable between the "EJ" and "MW" samples, there was a difference in E_T^{jet}. The effect is amplified in the H_T distribution as shown in Figure B.1. We required at least three jets in those plots in order to have enough statistics. We concluded from the plots that the "EJ" sample modeled data better than the "MW" sample.

[1] Since there was no evidence of mSUGRA signature in our data we did not add any mSUGRA events.

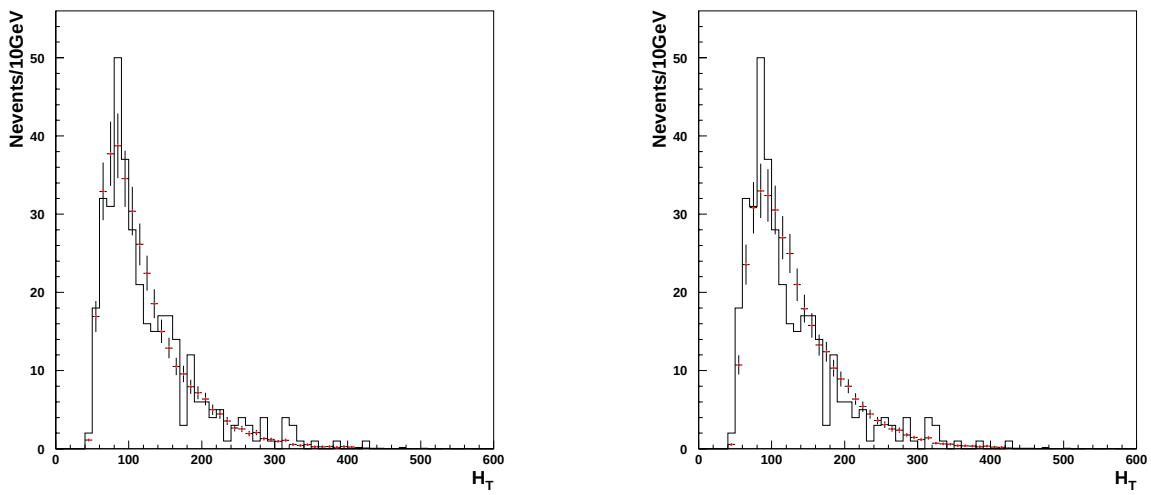

Figure B.1 Expected H_T distribution (points) vs data H_T distribution (histogram). VECBOS was generated with $Q^2 = (\frac{1}{n}\sum_i E_T^{parton})^2$ (left plot) and $Q^2 = M_W^2$ (right plot). At least 3 jets were required.

APPENDIX C $t\bar{t}$ 3C FIT

In this section we describe the 3C fit to $t\bar{t}$ events which decay to the electron + $\not\!\!E_T$ + ≥ 4 jets. For such decays. There are altogether 4 constraints:

$$f1 = M_{j1-e-\nu} - M_t = 0 \tag{C.1}$$

$$f2 = M_{j2-j3-j4} - M_t = 0 \tag{C.2}$$

$$f3 = M_{e-\nu} - M_W = 0 \tag{C.3}$$

$$f4 = M_{j3-j4} - M_W = 0. \tag{C.4}$$

We have denoted j1 and j2 as the b-jets from top or antitop decay. We set $M_t = 175$ GeV/c^2 and $M_W = 80.43$ GeV/c^2 in our fitter. In general, if the number of constraints is the same as the number of unknowns, there is a unique solution [1] to the problem. If the number of constraints is greater than the number of unknowns, the system is over-constrained. In latter case, the measured quantities can be adjusted (fitted) to satisfy all the constraints. The adjustment is such that the χ^2 defined in Equation C.5 is minimal:

$$\chi^2 = (\mathbf{x}^f - \mathbf{x}^m)^T \, \mathbf{G} \, (\mathbf{x}^f - \mathbf{x}^m) + 2\vec{f} \cdot \vec{\lambda}, \tag{C.5}$$

where $\mathbf{x}^f$, $\mathbf{x}^m$ are vectors of fitted and measured variables, respectively, $\mathbf{G}$ is the inverse error matrix which is determined by the resolution of the variables, $\vec{f}$ are the constraint equations and $\vec{\lambda}$ are the Lagrange multipliers.

Since the only unmeasured variable in our $t\bar{t}$ events is p_z^ν, we have a system with 3-constraints (4 constraints - 1 unknown). We used an algorithm very similar to that of the SQUAW kinematic

[1] Depending on the problem, sometimes we need to solve non-linear equations, e.g., the quadratic equation in solving for the neutrino p_z in $W \to e\nu$ events. In cases like these, we end up with more than one solution.

fitting program [69]. The input variables to the fit are the energy, pseudorapidity, and azimuthal angle of the electron and the four leading jets, and k_{Tx}, k_{Ty} [2]. One more variable is needed to uniquely define the $t\bar{t}$ system. We chose p_z^ν. Since it cannot be measured we calculated it by requiring that the invariant mass of $j1 - e - \nu$ is equal to the top mass. This led to a quadratic equation. If there were two real solutions then both solutions were used. If there was no real solution then only the real part of the solution was used.

The resolution of the variables were taken from [64] and are copied in Table C.1. We looped over all 12 jet permutations and all choices of p_z^ν in the fit. The jet permutation (see Equation C.1 to C.4) that corresponded to the lowest χ^2 was regarded as the jet order into which the "$t\bar{t}$" event decayed. The χ^2 distributions of $t\bar{t}$ events are shown in Figure C.1. We can see that for the fits that give correct permutation [3] the χ^2 is very close to the expected χ^2 function with 3 degrees of freedom.

Table C.1 Object resolutions. The operator $\bigoplus$ denotes a sum in quadrature.

Objects	Energy resolution	$\sigma(\eta)$	$\sigma(\phi)$
Electrons	$\frac{\sigma(E_T)}{E_T} = 0.0157 \bigoplus \frac{0.072\ \mathrm{GeV}^{1/2}}{\sqrt{E_T}} \bigoplus \frac{0.66\ \mathrm{GeV}}{E_T}$	0	0
Jets			
$0 < \lvert\eta_d\rvert < 0.8$	$\frac{\sigma(E)}{E} = 0.036 \bigoplus \frac{1.145\ \mathrm{GeV}^{1/2}}{\sqrt{E}}$	0.04	0.04 rad
$0.8 < \lvert\eta_d\rvert < 1.4$	$\frac{\sigma(E)}{E} = 0.082 \bigoplus \frac{1.264\ \mathrm{GeV}^{1/2}}{\sqrt{E}}$	0.05	0.05 rad
$1.4 < \lvert\eta_d\rvert < 2.5$	$\frac{\sigma(E)}{E} = 0.046 \bigoplus \frac{1.305\ \mathrm{GeV}^{1/2}}{\sqrt{E}}$	0.05	0.05 rad
k_T	$\sigma(k_{Tx}) = \sigma(k_{Ty}) = 12$ GeV		

The pull quantities of the fit are defined in Equation C.7. For correctly assigned resolutions

[2] $\vec{k}_T$ is defined in Equation C.6. It can be seen as the transverse momentum of the $t\bar{t}$ system.

$$\vec{k}_T = \vec{\not{E}}_T + \vec{E}_T^e + \sum_{4jets} \vec{E}_T^j \tag{C.6}$$

[3] Correct permutation means that the fitted jet order is the same as the jet order that matches the partons in Monte-Carlo.

they are expected to have a Gaussian distribution centered at 0 and with a width of 1. Figure C.3 shows the distribution of pull quantities of all variables which have finite resolution. A Gaussian fit to each distribution is also shown.

$$\xi_i = \frac{x_i^f - x_i^m}{\sigma_i} \tag{C.7}$$

From the distributions of χ^2 and the pull quantities we can conclude that our implementation of the fitter was correct. Finally we plotted the χ^2 distributions for W+jets, QCD multijet, WW and mSUGRA events in Figure C.2. As expected they have larger means than $t\bar{t}$ events.

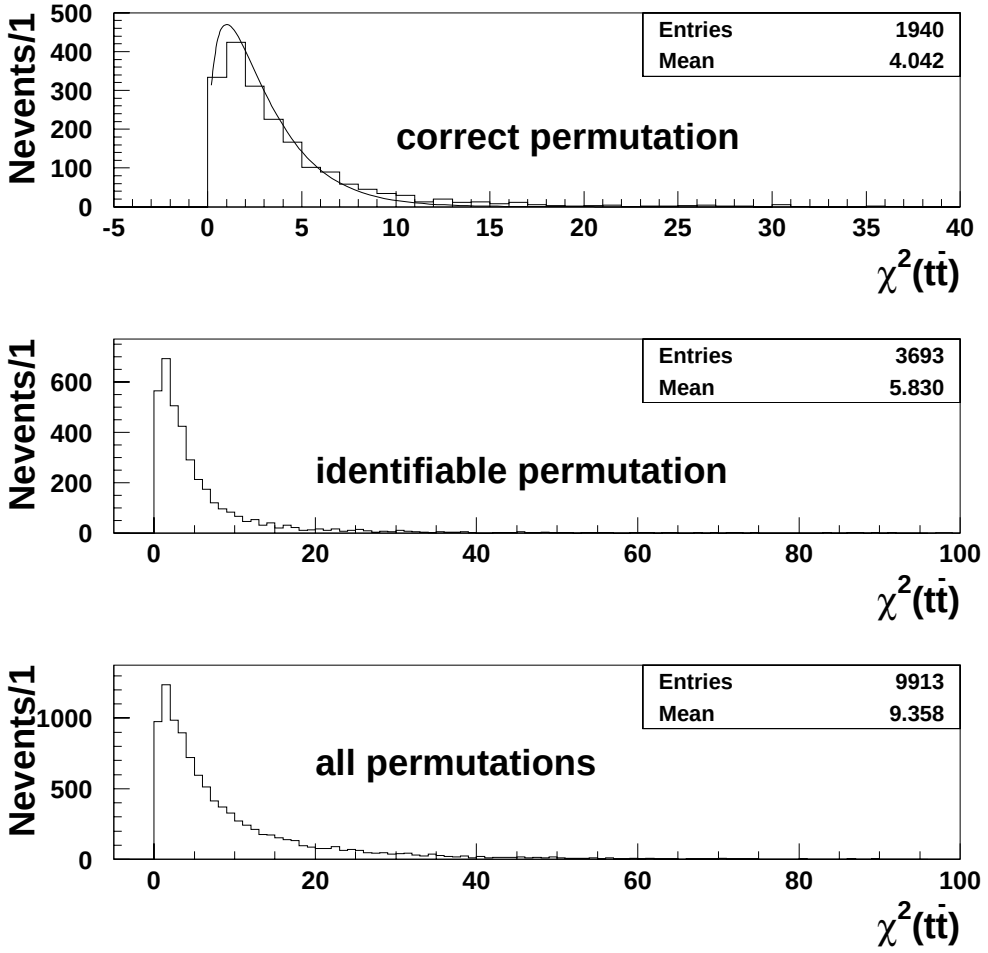

Figure C.1 χ^2 distribution of 3C fit to $t\bar{t}$ events. The top plot shows the χ^2 distribution for fits which result in the correct permutation. A χ^2 function with 3 degrees of freedom is also drawn. The middle plot shows the χ^2 distribution for events which a matching between the fitted jets to partons is identifiable (although may not be correct). The ratio of the number of events in the top plot to the middle plot gives how often our fitter results in a correct permutation. The rate is 52%. The bottom plot shows the χ^2 distribution we would expect for our data $t\bar{t}$ events. For representation purpose, the middle and the bottom plots show the χ^2 distributions only up to $\chi^2 = 100$.

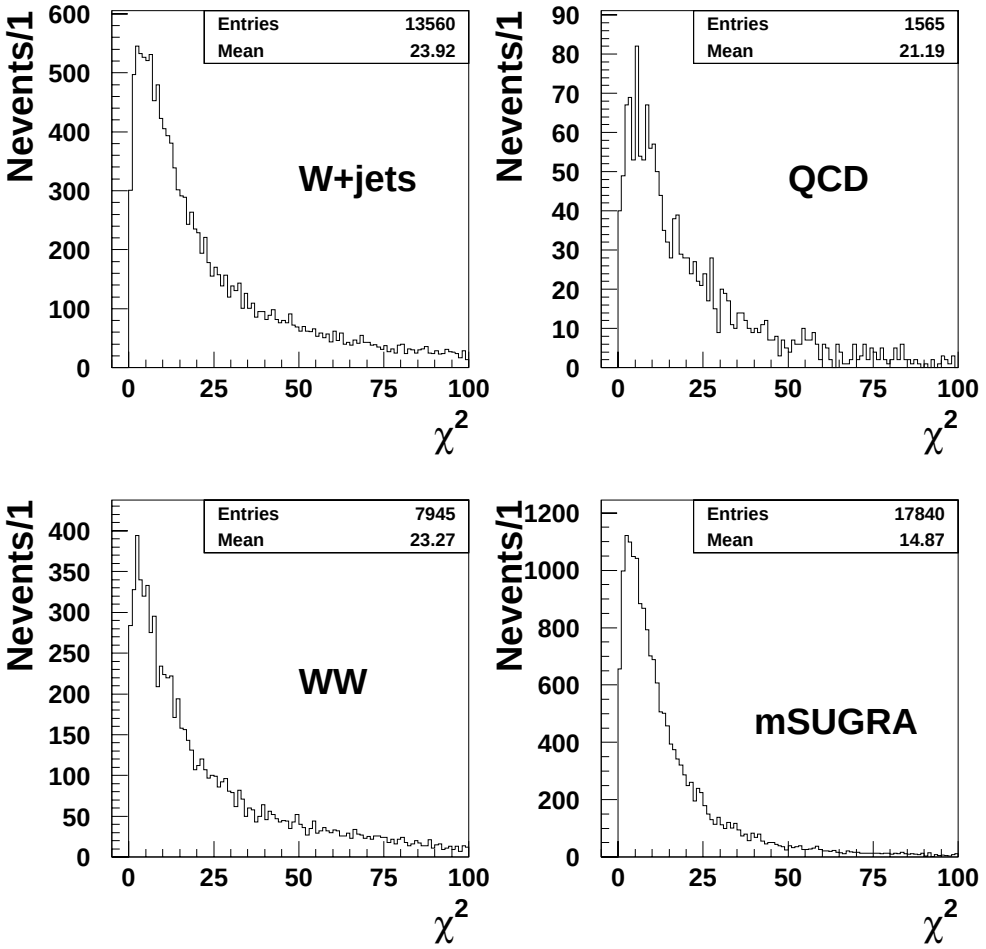

Figure C.2 χ^2 distributions of 3C fits performed on W+jet, QCD multijet, WW, and mSUGRA events. All events are required to have passed our initial selection cuts (see Chapter 4). In each plot we have a χ^2 cutoff at 100.

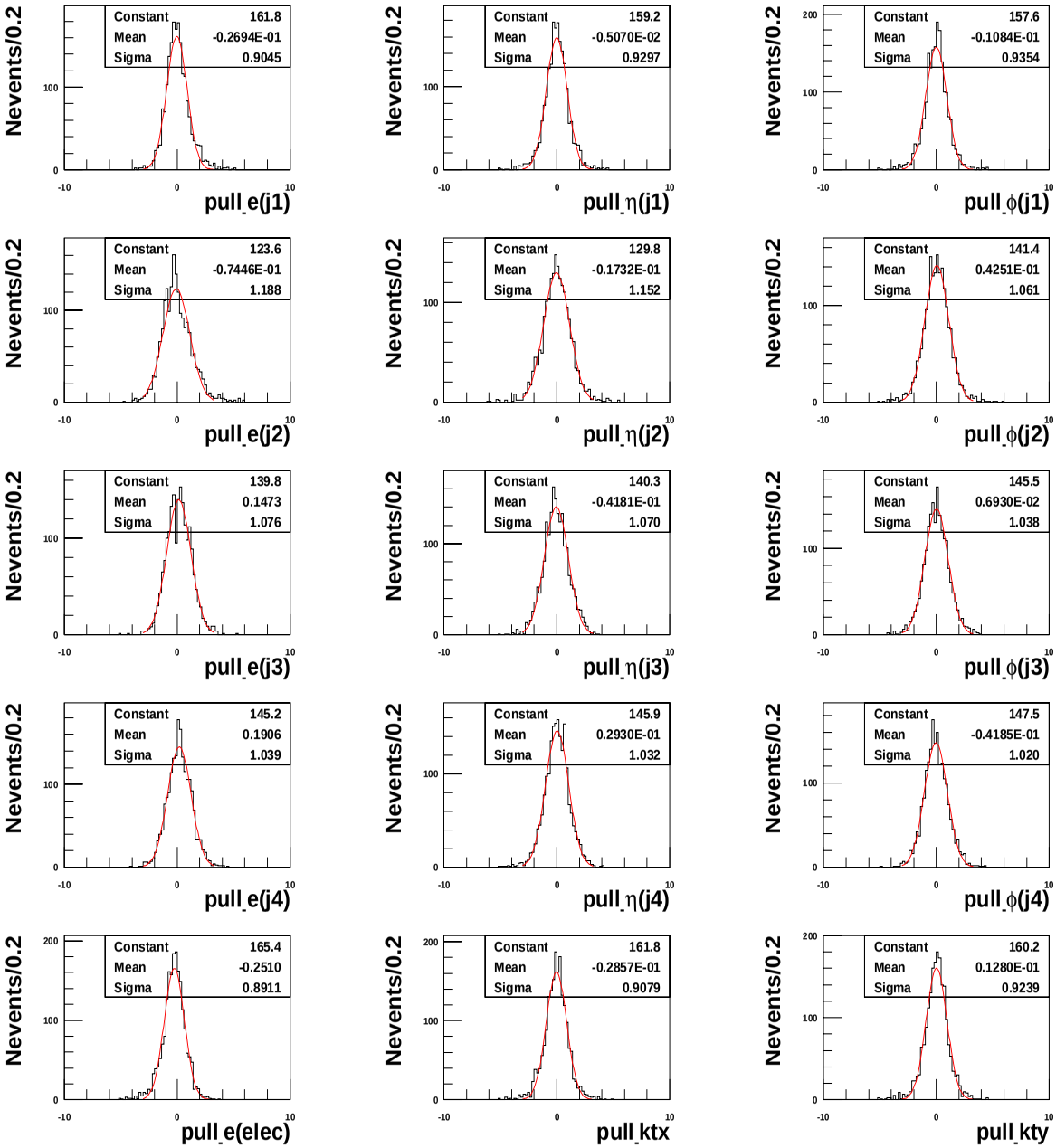

Figure C.3 Distribution of pull quantities of all variables which have finite resolution. A Gaussian fit between (-3,3) is also plotted on top of each distribution. The fits indicate that the resolution assignment was correct.

APPENDIX D NEURAL NETWORKS

In this analysis, we extensively used neural networks (NN) [1] to obtain optimal selection cut on signal against background. This appendix attempts to give a brief introduction to neural networks.

D.1 Perceptron

Neural networks are mathematical simulations of human brain to do pattern recognition. They are usually composed of networks of many simple units which are called perceptrons [2]. A typical perceptron has many inputs and one output as shown in Figure D.1. It performs the following functions:

- all the inputs are combined linearly, e.g., for the perceptron in Figure D.1,

$$y_i = \sum_k w_{ik} x_k + \theta_i, \tag{D.1}$$

  where index i denotes the ith perceptron and θ denotes the perceptron threshold. Index k sums over the number of the inputs;

- send an output signal to other perceptrons. The output signal is a linear or a non-linear transformation of y. For a non-linear transformation, the most popular function is the sigmoid function. One of such is given in Equation D.2 and plotted in Figure D.2.

$$g(y) = \frac{1}{1 + e^{-y}}. \tag{D.2}$$

[1] In fact they should be called artificial neural networks (ANN) to be distinguished from the biological neural networks. We use NN throughout in this analysis to refer to artificial NN.

[2] The biological analogy of a perceptron is a neuron.

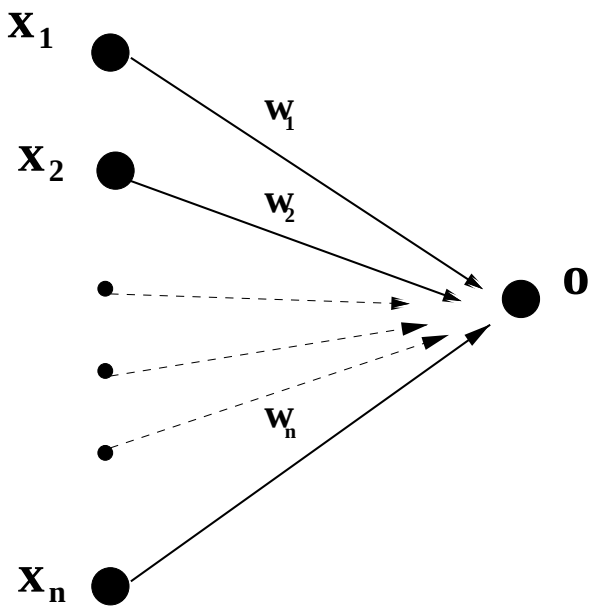

Figure D.1 A perceptron.

The sigmoid function in Figure D.2 shows a "turn-on" feature. For a large positive argument it is activated (output ≈ 1), while for a large negative argument it is dormant (output ≈ 0).

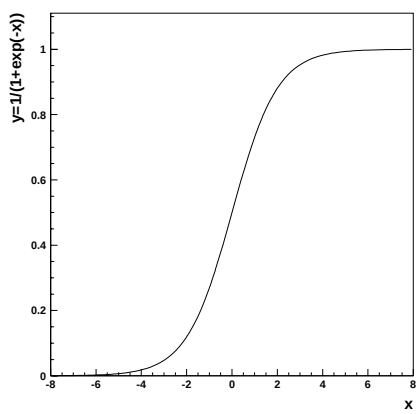

Figure D.2 The sigmoid function: $g(x) = \frac{1}{1+e^{-x}}$.

D.2 Mathematical Interpretation

There are many kinds of neural networks. The one which is used most extensively and is used in this analysis is called the feed-forward network. "Feed-forward" refers to the direction in which values are propagated through the network. A network is usually composed of many layers of perceptron. Figure D.3 shows a simple feed-forward network with three layers: one input layer, one hidden layer, and one output layer. Each point in the figure is called a node. A network of this structure is also called a multilayer perceptron (MLP). MLPfit [59] software package, which is used in this analysis, is named after this. The output of such a network can be written as

$$O(x_1, x_2, \ldots, x_n) = g\left(\sum_j^m w_j \cdot g\left(\sum_k^n w_{jk} x_k + \theta_j\right) + \theta\right), \tag{D.3}$$

where k and j sum over the nodes in the input layer and the hidden layer respectively. There are n (m) nodes in the input (hidden) layer. The θ's are thresholds.

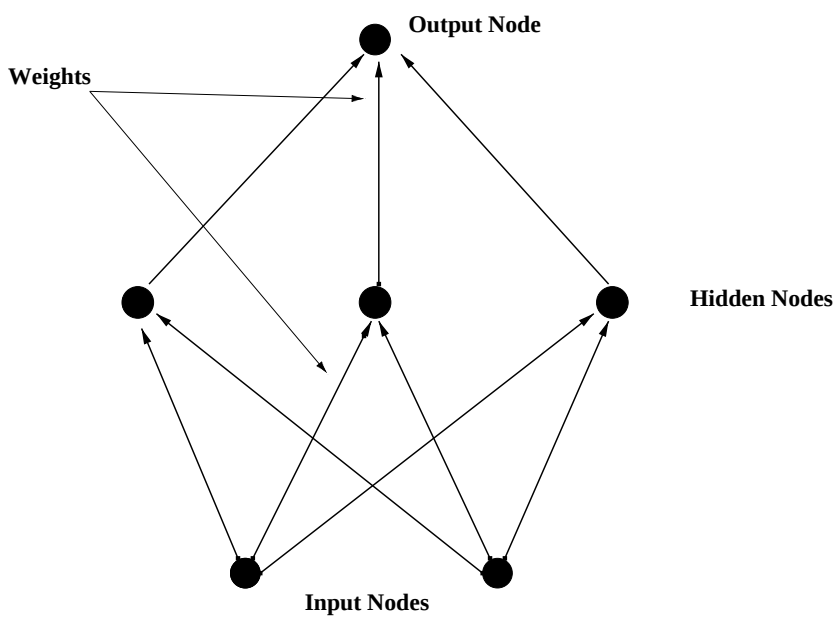

Figure D.3 A multilayer perceptron feed-forward neural network. There are 2 input nodes, 3 hidden nodes, and 1 output node.

It has been shown that feed-forward networks with a single hidden layer are capable of

approximating virtually any function in practical application to an arbitrary precision, provided that they have sufficient number of nodes in the hidden layer [70]. It has also been shown that if such networks use thresholds or sigmoid activation function they are universally consistent estimators of binary classifications, i.e., signal and background classification [71]. In high energy physics, the most common task is to distinguish signal from background. Usually a set of variables are constructed, each of which has a different distribution for signal and background. We want to find a function which maps these variables to a single output to optimally classify whether a particular set of inputs belongs to signal or background. This function is called the mapping function and is usually non-linear. It can be so complicated that its construction from first principle, e.g., from matrix element calculation, is practically impossible. Neural networks try to find an approximation to the mapping function by finding the weights and thresholds in Equation D.3. Furthermore, the output of an MLP actually represents the Bayesian posterior probability for either signal or background [72].

A frequently asked question is why we need thresholds in the network. This can be answered by looking at Equation D.3. $\sum_k w_{jk} x_k + \theta_j$ represents a hyperplane in the multi-variable space. Without a threshold we would be requiring the hyperplane to pass the hyperspace origin, restricting the generality. Another question is why we need the non-linear transformation. This is because a composition of linear function is again a linear function while most problems are nonlinear. To approximate a non-linear mapping function, non-linear transformation has to be used.

D.3 Using Neural Networks

The weights and thresholds in the neural networks are obtained by a process called "training", much similar to the human learning process. The training is performed on the signal and background simultaneously. A mean square error function E is constructed

$$E = \frac{1}{2N_p} \sum_{1}^{N_p} \sum_{1}^{N} (O_i^{(p)} - t_i^{(p)})^2, \tag{D.4}$$

where $O_i^{(p)}$ is the NN output for pattern p (signal or background); $t_i^{(p)}$ is the training target (or the expected training result; in our case it is 0 for background and 1 for signal); N_p is the number of patterns (events) in the training samples; and N is the number of network outputs (set to 1 in this analysis).

The goal of training is to minimize function E. After sufficient training a set of weights and thresholds, and an approximation to the mapping function as defined in Equation D.3 are obtained. We apply this function to data events to classify whether they are signal or background.

The number of free parameters in an NN is equal to the total number of weights and thresholds in the network. For an MLP with I input nodes, H hidden nodes, and 1 output node, the number of free parameters is $I \times H + 2H + 1$. In order to sufficiently train the network so that it can approximate the mapping function well, the number of training events is usually required to be at least an order of magnitude larger than the number of free parameters. This requirement is always satisfied in this analysis.

Care must be taken to avoid over-training the network. Statistical fluctuation of the variables in both signal and background provides a "noise" to the network. Over-training happens when the network is learning the noise, as well as the signal or background. The usual method to avoid over-training is to examine the mean square error of a statistically independent test sample. The noise is not the same in the training sample as in the test sample. If the noise in the training sample is being learned, it will lead to an increase in the mean square error in the test sample. In this analysis, every training was monitored with a statistically independent sample.

BIBLIOGRAPHY

[1] I. Mendeleev, Annalen der Chemie und Pharmacie 8, Supplementary Volume for 1872, p.511.

[2] J. J. Thompson, Philos. Mag. **44**, 293 (1897).

[3] E. Rutherford, Proceedings of the Manchester Literary and Philosophical Society, IV, **55**, 18 (1911).

[4] N. Bohr, Philos. Mag. **26**, 1(1913), 476(1913), 857 (1913).

[5] E. Rutherford, Phil. Mag. **31**, 581 (1919).

[6] J. Chadwick, Roy. Soc. Proc, **136**, 692 (1932).

[7] C. M. .G. Lattes *et al.*, Nature **159**, 694 (1947); **160**, 453, 486 (1947).

[8] P. A. M. Dirac, "The Principles of Quantum Mechanics", 4th *ed.*, Oxford Clarendon Press (1958); J. Schwinger, "Selected Papers on Quantum Electrodynamics", Dover Publications, New York (1958); R. P. Feynman, "QED: The Strange Theory of Light and Matter", Princeton University Press, Princeton, NJ (1985).

[9] C. N. Yang and R. .L. Mills, Phys. Rev. **96**, 191 (1954).

[10] M. Gell-Mann, Phys. Lett. **8**, 214 (1964); G. Zweig, CERN Report 8182/TH.401 (1964, unpublished); CERN Report 8419/TH.412(1964, unpublished), reprinted in "Developments in the Quark Theory of Hadrons", Vol. 1: 1964-1978, edited by D. B. Lichtenberg and S. P. Rosen, Hadronic Press, Nonantum, MA (1980), p.22; M. Gell-Mann and Y. Ne'eman, "The Eightfold Way", Benjamin Publishers, New York (1964)

[11] S. Weinberg, Phys. Rev. Lett. **19**, 1264(1967); A. Salam, "Elementary Particle Theory: Relativistic Groups and Analyticity (Nobel Symposium No. 8)", edited by N. Svartholm, Almqvist, and Wiksell, Stockholm (1968), p.367.

[12] E. D. Bloom *et al.*, Phys. Rev. Lett. **23**, 930 (1969); M. Breidenbach *et al.*, Phys. Rev. Lett., **23**, 935 (1969).

[13] J. D. Bjorken, Phys. Rev. **179**, 1547 (1969); R. P. Feynman, "Photon-Hadron Interactions", Benjamin, Reading, MA (1972).

[14] J. J. Aubert *et al.*, Phys. Rev. Lett. **33**, 1404 (1974); J. E. Augustin *et al.*, Phys. Rev. Lett. **33**, 1406 (1974).

[15] S.W.Herb *et al.*, Phys. Rev. Lett. **39**, 252 (1977).

[16] CDF collaboration, F. Abe *et al.*, Phys. Rev. Lett. **74**, 2626 (1995); DØ collaboration, S. Abachi *et al.*, Phys. Rev. Lett. **74**, 2632 (1995).

[17] UA-1 Collaboration, G.Arnison *et al.*, Phys. Lett. **122B**, 103, 398 (1983).

[18] For a review, see C. Quigg, "Gauge Theories of the Strong, Weak, and Electromagnetic Interactions", Addison-Wesley (1983), Chapter 5.

[19] P. W. Higgs, Phys. Lett. **12**, 132 (1964).

[20] C. Quigg, "Gauge Theories of the Strong, Weak, and Electromagnetic Interactions", Addison-Wesley (1983), p.188-189.

[21] R. Cahn, Rev. Mod. Phys., **68**, 951 (1996).

[22] N. Cabibbo, Phys. Rev. Lett. **10**, 531 (1963); M. Kobayashi and T. Maskawa, Prog. Theor. Phys. **49**, 652 (1973).

[23] SK Collaboration, S. Fukuda *et al.*, Phys. Rev. Lett. **86**, 5651 (2001); SNO Collaboration, Q.R.Ahmad *et al.*, nucl-ex/0106015

[24] M. E. Peskin and D. V. Schroeder, "An Introduction to Quantum Field Theory", Addison Wesley (1995), p.720-721, p.726-727.

[25] The strong CP problem, its proposed solutions, and their unexpected implications are reviewed by R. .D. Peccei in "CP Violation", edited by C. Jarlskog, World Scientific (1989).

[26] S. Dawson, "SUSY and Such", hep-ph/9612229, v2.

[27] J. L. Hewett, "The Standard Model and Why We Believe It", hep-ph/9810316.

[28] S. Martin, "A Supersymmetric Primer", hep-ph/9709356.

[29] Particle Data Group, D. E. Groom *et al.*, The European Physical Journal C, vol.15, 2000.

[30] G. R. Farrar and P. Payet, Phys. Lett. **B76**, 575 (1978).

[31] LEP2 SUSY Working Group, http://www.cern.ch/LEPSUSY.

[32] C. Fabjan, "Calorimetry in High Energy Physics", Experimental Techniques in High-Energy Nuclear and Particle Physics, World Scientific Publishing Co. Pte. Ltd. (1991), p.257-324; R. Wigmans, Nucl. Instrum. Methods, **A265**, 273 (1988).

[33] DØ collaboration, S. Abachi *et al.*, Nucl. Instrum. Methods, **A338**, 185 (1994).

[34] G. Manning, "DØ Software Documentation".

[35] "Experimental Techniques in High-Energy, Nuclear, and Particle Physics", edited by T. Ferbel, World Scientific (1991), p.6.

[36] CERN, "GEANT Detector Description and Simulation Tool", CERN Program Library Long Writeup W5013, 1994.

[37] U. Heintz and M. Narain, "Electron ID with Transition Radiation Detector and Central Drift Chamber", DØ note 2355, 1994

[38] M. Narain and U. Heintz, "A Likelihood Test for Electron ID", DØ note 2386, 1994.

[39] DØ collaboration, B. Abbott *et al.*, Nucl. Instrum. Methods Phys. Res. A**424**, 352 (1999).

[40] E. Gallas, "The MTC Package (Muon Tracking in the DØ calorimeter)", DØ note 2066, 1995.

[41] DØ collaboration, B. Abbott *et al.*, Phys. Rev. D Rapid Comm. **63**, 091102 (2001).

[42] DØ collaboration, B. Abbott *et al.*, Phys. Rev. Lett. **83**, 4937 (1999).

[43] A. S. Belyaev *et al.*, "Electroweak Production of Single Top Quarks at DØ", DØ note 3772, 2000.

[44] J. Butler *et al.*, "Measurement of the Top Quark Production Cross Section Using lepton + jets events, DØ note 2978, 1995.

[45] Private communication with Daniel Elvira.

[46] L. Babukhadia *et al.*, "Standard Jet Cuts and their Efficiencies for Run 1B", DØ note 3407, 1998.

[47] R. Genik, "The Search for Di-lepton Signatures from Squarks and Gluinos in $p\overline{p}$ Collisions at $\sqrt{s} = 1.8$ TeV", Ph.D. thesis (Volume II), 1998.

[48] R. Genik, "The Search for Di-lepton Signatures from Squarks and Gluinos in $p\overline{p}$ Collisions at $\sqrt{s} = 1.8$ TeV", Ph.D. thesis (Volume I), 1998.

[49] S. Eno, R. Genik, J. Hobbs, and L. Lueking, "The Fast MC QSIM", DØ note 3587, 1999.

[50] M. Bengtsson and T. Sjöstrand, Comp. Phys. Commun. **43** 367 (1987).

[51] G. Marchesini *et al.*, Comp. Phys., Comm., **67**, 465 (1992) (release v5.9).

[52] S. Mrenna, "Simulating Supersymmetry with PYTHIA 5.7 and JETSET 7.4", hep-ph/9609360.

[53] F. A. Berends *et al.*, Nucl. Phys., **B357**, 32 (1991).

[54] DØ collaboration, B. Abbott *et al.*, Phys. Rev. D **62**, 052005 (2000).

[55] J. Yu, "Determination of the Strong Coupling Constant (α_s) and a Test of Perturbative QCD Using W + Jets Processes in the DØ Detector", Ph.D. thesis, 1993.

[56] DØ collaboration, B. Abbott *et al.*, "$t\overline{t}$ Production Cross Section in $p\overline{p}$ Collisions at $\sqrt{s} = 1.8$ TeV", in preparation for Phys. Rev. D.

[57] J. Ohnemus, Phys. Rev. D **44**, 1402 (1991).

[58] P. Grudberg, "Measurement of the W and Z Boson Production Cross Sections in $p\overline{p}$ Collisions at $\sqrt{s} = 1.8$ TeV with the DØ Detector", Ph.D. thesis, 1997.

[59] J. Schwindling and B. Mansoulié, "MLPFIT", http://schwind.home.cern.ch/schwind/MLPfit.html.

[60] E. Flattum, "A Measurement of the W Boson Mass in $p\overline{p}$ Collisions at $\sqrt{s} = 1.8$ TeV", Ph.D. thesis, 1996.

[61] I. Adam, "Measurement of the W Boson Mass with the D0 Detector Using the Electron Et Spectrum", Ph.D. thesis, 1997.

[62] The Coordinated Theoretical-Experimental Project on QCD, http://www.phys.psu.edu/ cteq/.

[63] V. D. Bagger and R. J. N. Phillips, "Collider Physics", Addison-Wesley, Reading, MA (1987), p.281.

[64] DØ collaboration, B. Abbott *et al.*, Phys. Rev. D **58**, 052001 (1998).

[65] G. Mahlon and S. Parke, "Maximizing Spin Correlations in Top Quark Pair Production at the Tevatron", hep-ph/9706304, 1997.

[66] R. Partridge, "Optimizing Statistical Significance for Small Signals", DØ note 3383, 1998.

[67] I. Bertram *et al.*, "A Recipe for the Construction of Confidence Limits", DØ note 2775, 1995.

[68] F. Bedeschi, FERMILAB-CONF-01/006-E, or Proceedings 20th Physics in Collision Conference, Lisbon, Portugal, June 29-July 1, 2000.

[69] O. I. Dahl, T. B. Day, F. T. Solmitz, and N. L. Gould, Technical Report No. P-126, Lawrence Radiation Laboratory, 1968, Berkeley, California (unpublished); J. P. Berge, F. T. Solmitz, and H. D. Taft, Rev. Sci. Instrum. **32**, 538 (1961).

[70] K. Hornik, M. Stinchcombe, and H. White, Neural Networks, **2**, 359 (1989).

[71] A. Faragó and G. Lugosi, IEEE Transactions on Information Theory, **39**, 1146 (1993); G. Lugosi and K. Zeger, IEEE Transactions on Information Theory, **41**, 677 (1995); L. Devroye, L. Györfi, and G. Lugosi, "A Probabilistic Theory of Pattern Recognition", Springer (1996).

[72] D. .W. Ruck *et al.*, IEEE Trans., Neural Networks **1 (4)**, 296 (1990); E. A. Wan, IEEE Trans., Neural Networks **1 (4)**, 303 (1990).